

1-1-2008

## Study of the interaction between hydrogen and carbon-based nanomaterials

Roberto Felix  
*University of Nevada, Las Vegas*

Follow this and additional works at: <https://digitalscholarship.unlv.edu/rtds>

---

### Repository Citation

Felix, Roberto, "Study of the interaction between hydrogen and carbon-based nanomaterials" (2008).  
*UNLV Retrospective Theses & Dissertations*. 2370.  
<http://dx.doi.org/10.25669/fq5s-wudp>

This Thesis is protected by copyright and/or related rights. It has been brought to you by Digital Scholarship@UNLV with permission from the rights-holder(s). You are free to use this Thesis in any way that is permitted by the copyright and related rights legislation that applies to your use. For other uses you need to obtain permission from the rights-holder(s) directly, unless additional rights are indicated by a Creative Commons license in the record and/or on the work itself.

This Thesis has been accepted for inclusion in UNLV Retrospective Theses & Dissertations by an authorized administrator of Digital Scholarship@UNLV. For more information, please contact [digitalscholarship@unlv.edu](mailto:digitalscholarship@unlv.edu).

STUDY OF THE INTERACTION BETWEEN HYDROGEN AND CARBON-BASED  
NANOMATERIALS

by

Roberto Félix

Bachelor of Science  
University of Nevada, Las Vegas  
2005

A thesis submitted in partial fulfillment  
of the requirements for the

**Master of Science Degree in Chemistry**  
**Department of Chemistry**  
**College of Science**

**Graduate College**  
**University of Nevada, Las Vegas**  
**August 2008**

UMI Number: 1460527

Copyright 2009 by  
Felix, Roberto

All rights reserved.

## INFORMATION TO USERS

The quality of this reproduction is dependent upon the quality of the copy submitted. Broken or indistinct print, colored or poor quality illustrations and photographs, print bleed-through, substandard margins, and improper alignment can adversely affect reproduction.

In the unlikely event that the author did not send a complete manuscript and there are missing pages, these will be noted. Also, if unauthorized copyright material had to be removed, a note will indicate the deletion.

**UMI**<sup>®</sup>

---

UMI Microform 1460527

Copyright 2009 by ProQuest LLC.

All rights reserved. This microform edition is protected against unauthorized copying under Title 17, United States Code.

ProQuest LLC  
789 E. Eisenhower Parkway  
PO Box 1346  
Ann Arbor, MI 48106-1346



**Thesis Approval**  
The Graduate College  
University of Nevada, Las Vegas

June 23, 2008

The Thesis prepared by

Roberto Felix

Entitled

Study of the Interaction between Hydrogen and Carbon-based  
Nanomaterials

is approved in partial fulfillment of the requirements for the degree of

Master of Science in Chemistry

Examination Committee Chair

Dean of the Graduate College

Examination Committee Member

Examination Committee Member

Graduate College Faculty Representative

## ABSTRACT

### **Study of the Interaction between Hydrogen and Carbon-based Nanomaterials**

by

Roberto Félix

Dr. Clemens Heske, Examination Committee Chair  
Associate Professor of Chemistry  
University of Nevada, Las Vegas

Hydrogen is a promising energy carrier. Coupling hydrogen production to renewable energy sources would help alleviate the world's dependence on fossil fuels. A hurdle that must be overcome for that scenario is the development of satisfactory hydrogen storage media. Theoretical work suggests that carbon-based nanomaterials are plausible candidates.

The research objective of this work is to study the influence of hydrogen adsorption on the chemical and electronic properties of carbon-based nanomaterials (i.e., single-walled carbon nanotubes and  $C_{60}$ ). An atomic hydrogen source was constructed. Nanomaterials were exposed to atomic and/or molecular hydrogen, and the local chemical and electronic interaction was studied using Photoelectron Spectroscopy. Annealing of hydrogenated samples shows the reversibility of the adsorption of atomic hydrogen. The results obtained give detailed information about hydrogenation-induced chemical and electronic interactions, showing that Photoelectron Spectroscopy, with the atomic hydrogen source, is a powerful tool to investigate the hydrogen storage potential of carbon-based nanomaterials.

## TABLE OF CONTENTS

ABSTRACT.....	iii
LIST OF FIGURES.....	v
ACKNOWLEDGEMENTS.....	vi
CHAPTER 1 INTRODUCTION.....	1
1.1 Hydrogen Adsorption on Carbon-based Nanomaterials.....	3
CHAPTER 2 EXPERIMENTAL METHODOLOGY.....	8
2.1 Photoelectron Spectroscopy Principles.....	8
2.2 Instrumentation.....	15
CHAPTER 3 ATOMIC HYDROGEN SOURCE.....	20
3.1 Introduction.....	20
3.2 Hydrogen Dissociation by Tungsten.....	21
3.3 AHS Atomic Hydrogen Production.....	24
CHAPTER 4 RESULTS AND DISCUSSION.....	34
4.1 Introduction.....	34
4.2 $T_w$ -dependence Hydrogenation Study.....	34
4.3 Hydrogen Adsorption/Desorption Cycle Study.....	58
4.4 $C_{60}$ Hydrogenation Study.....	75
CHAPTER 5 SUMMARY AND FUTURE WORK.....	85
5.1 Summary.....	85
5.2 Future work.....	86
APPENDIX I DETAILED XPS AND UPS DATA OF THE $T_w$ -DEPENDENT HYDROGENATION SERIES (SECTION 4.2) .....	88
APPENDIX II DETAILED XPS AND UPS DATA OF THE HYDROGEN ADSORPTION/DESORPTION CYCLING SERIES (SECTION 4.3) .....	90
BIBLIOGRAPHY.....	92
VITA.....	98

## LIST OF FIGURES

Figure 1.1	C <sub>60</sub> Fullerene and SWNTs in three different Chiralities. ....	3
Figure 2.1	Schematic Diagram of the XPS , UPS and the XAES Processes.....	9
Figure 2.2	Schematic Diagram of the PES Experimental Setup.....	10
Figure 2.3	Universal Curve of the Inelastic Mean Free Path of Electrons in Solid.....	11
Figure 2.4	XPS survey of C <sub>60</sub> on Gold Substrate probed by Mg K <sub>α</sub> excitation.....	13
Figure 2.5	Diagrams of the two employed Surface Analysis Systems .....	16
Figure 3.1	Potential Energy Profile of H <sub>2</sub> Molecule approaching W Surface .....	22
Figure 3.2	Schematic Diagram of the Atomic Hydrogen Source .....	25
Figure 3.3	Picture of the constructed Atomic Hydrogen Source. ....	26
Figure 3.4	Measured P <sub>AH</sub> /P <sub>H2</sub> Ratios as a Function of T <sub>w</sub> for five different ΔP <sub>H2</sub> .....	28
Figure 3.5	Mass Spectrometer P <sub>AH</sub> background as a Function of ΔP <sub>H2</sub> .....	30
Figure 4.1	XPS of SWNT sample and after Hydrogenation Treatments.....	38
Figure 4.2	Detailed C 1s XPS of SWNT Sample and Hydrogenation-treated. ....	39
Figure 4.3	SWNT C 1s Chemical Shifts induced by Hydrogenation Treatments. ....	41
Figure 4.4	SWNT C 1s FWHM during Hydrogenation Treatment. ....	42
Figure 4.5	Deconvolution of the C 1s Photoemission Line.....	43
Figure 4.6	C 1s Line Deconvolution of five Experimental Series Stages. ....	44
Figure 4.7	sp <sup>3</sup> /sp <sup>2</sup> Carbon in SWNT Sample as Function of T <sub>w</sub> Hydrogenation.....	46
Figure 4.8	O and Cl Surface Levels along the Course of the Experimental Series. ....	48
Figure 4.9	Deposition of Fluorine on SWNT Sample. ....	50
Figure 4.10	He II UPS VBM of SWNT Sample and Hydrogenation-treated.....	52
Figure 4.11	SWNT π–Electron Conjugation System Reduction by Hydrogenation.....	54
Figure 4.12	Hydrogenation-induced SWNT Work Function Reduction.....	57
Figure 4.13	XPS of SWNT sample of five Experimental Series Stages. ....	61
Figure 4.14	Oxygen Speciation along the Course of the Experimental Series.....	62
Figure 4.15	F 1s XPS of SWNT Sample and Hydrogenation-treated .....	63
Figure 4.16	C 1s XPS of SWNT Sample in Hydrogenation-cycling.....	64
Figure 4.17	SWNT C 1s Line Position throughout Experimental Series Stages.....	65
Figure 4.18	SWNT C 1s FWHM throughout the Experimental Series Stages.....	66
Figure 4.19	Deconvolution of C 1s Line along the Experimental Series Phases .....	68
Figure 4.20	sp <sup>3</sup> /sp <sup>2</sup> Carbon of SWNT Sample of the Experimental Series Phases.. ....	69
Figure 4.21	He II UPS VBM of SWNT Sample of 2 <sup>nd</sup> Experimental Series Phases .....	71
Figure 4.22	SWNT π–Electron Conjugation System Modulations. ....	72
Figure 4.23	Cycling of SWNT Sample’s Work Function.....	74
Figure 4.24	XPS Survey of C <sub>60</sub> Sample and Hydrogenation-treated.....	79
Figure 4.25	Deconvolution of C <sub>60</sub> C 1s Line and Hydrogenation-treated. ....	80
Figure 4.26	He II UPS VBM of C <sub>60</sub> Sample and Hydrogenation-treated.....	82
Figure 4.27	Hydrogenation-induced C <sub>60</sub> Work Function Reduction. ....	83

## ACKNOWLEDGEMENTS

I would like to take a moment to acknowledge the people without whom the writing of this thesis would not have been possible.

I wish to thank Prof. Clemens Heske for the kindness and guidance he has generously given to me throughout this work. I will always appreciate that he allowed me to join his research group. Not only has it been great fun to work in his laboratory, but the experience I have garnered as a result has been invaluable. The dedication, enthusiasm and energy he bestows upon his work have left a deep, inspiring impression in me.

I am also very grateful to my committee members Prof. Pamela Burnley, Prof. Chulsung Bae, and Prof. Balakrishnan Naduvalath for the time they have invested in helping to complete this thesis and their encouraging comments. There is no doubt in my mind that they have made my task much smoother.

I could not forget Dr. Lothar Weinhardt's help in becoming familiar with the PES instrumentation and his advice during the construction of the hydrogen source. Dr. Marcus Bär has constantly been open to discuss questions I have encountered pertinent to research and other issues. Dr. Yufeng Zhang has been a great source of aid in the writing of this thesis. They have all earned my respect and high esteem.

Many thanks go to my fellow lab graduate students. Timo Hofmann, as the most PES-experienced graduate member of the group, has been a great support -- like standing on strong shoulders. Sujitra Pookpanratana's insights and optimism always factored in the



research work's delight. Thanks! Sharath Sudarshanam has been a cheerful office neighbor and a Fityk master. Ich Tran has been a commendable team partner.

Special thanks go to Amo Sanchez, for his continued assistance in part manufacturing, and Carlos Ezeta and Pat Zozaya, for their help during my years as a UNLV student.

I am very grateful to my family. To my brother Alexander, I am obliged for his support and joyful spirit, always reminding me there is light at the end of the tunnel. To my brother David, I particularly acknowledge his altruistic disposition and hard work in helping me type this thesis. My thank-yous do not do him justice. (I could not have done it without you David!) To my parents, Ana and Roberto, I will always be indebted for their love and care. How could that possibly be repaid? Whatever it may be I have accomplished, I owe it to them.

## CHAPTER 1

### INTRODUCTION

During the 16<sup>th</sup> century, the first recorded acquaintance that mankind made with molecular hydrogen took place [1]. By mixing metals with strong acids, Phillip von Hohenheim inadvertently produced hydrogen gas. Ever since, investigation of the properties of the simplest of elements has ultimately revealed the indispensable role it has played not only in the subsistence of all life form in our planet, but in the existence of the universe. Not surprisingly, understanding the behavior of the minutest element has resulted in the launching of scientific revolutions in our knowledge of the natural sciences.

During the 21<sup>st</sup> century, hydrogen once again appears to have a prominent position in the solving of a monumental challenge currently being faced by human society. The non-renewable fossil fuel energy resources upon which human society so heavily depends continue to be strained by the world's growing energetic demands [2]. As the human population continues to grow and developing countries attain greater industrialization, the fossil fuel reserves are greater stretched, and their rate of consumption takes a higher toll on the global environment and threatens Earth's climate stability [3].

Consequently, enormous efforts are being directed toward the development of renewable energy sources that may someday serve as an alternative to fossil fuels. For this purpose, hydrogen is seen as a promising energy carrier. By reacting with oxygen,

hydrogen releases energy with water being the reaction's product. Since hydrogen is predominantly found on earth as part of chemical compounds and not as  $H_2$  fuel, coupling molecular hydrogen production to renewable energy or nuclear power sources could ideally be an effective way of alleviating the world's overwhelming dependence on fossil fuels. For example, solar energy could be used to electrolyze water via photocells, or be employed as a heat source to facilitate high-temperature hydrogen-producing thermochemical cycles. Moreover, cellular organisms known to generate hydrogen could be employed in this task, and by investigating their biological functions, new hydrogen yielding mechanisms could be developed [4].

In addition to cost-effective hydrogen production obstacles, for a hydrogen economy scenario to take place, the development of storage media with special criteria for the energy transportation sector is required. Among the factors desirable hydrogen storage media must possess are: safety, cost-efficiency, reversibility, and high gravimetric and volumetric storage properties. This is certainly the case for transportation applications, which require a quantity of fuel in one tank load that is sufficient to travel distances comparable to fossil-fuel powered vehicles. For this purpose, the US Department of Energy (DOE) has envisioned a 6.5 %-wt. hydrogen storage capacity requirement for hydrogen-powered transportation [5]. Furthermore, release and adsorption of hydrogen need to occur under ambient temperatures and moderate pressures (i.e. 1-10 atm.), conditions permissible in automobiles. Thus, a balance must be found between materials that can achieve high hydrogen storage capacities, due to strong chemical bonding between hydrogen and low-mass atom materials, and storage media with low-temperature capture and release of hydrogen, requiring "weak chemical bonds, fast kinetics, and short

diffusion length, as might be found in surface adsorption” [4]. Because carbon-based nanomaterials, such as single-walled carbon nanotubes (SWNT) and  $C_{60}$  fullerenes, combine both desired aspects, carbon-based nanomaterials have been considered promising candidates for storage of hydrogen.

### 1.1 Hydrogen Adsorption on Carbon-based Nanomaterials

$C_{60}$  fullerenes were discovered in 1985, the third carbon allotrope to be identified [Kro85], and set the stage for the discovery of other fullerene carbon structures. SWNTs were first discovered by S. Iijima in 1993 [6]. These carbon allotropes can conceptually be described as seamless rolled-up graphene sheets.  $C_{60}$  possesses a 7 Å diameter, whereas the diameter range of SWNT is of a few nanometers. The electronic structure of the nanotube’s  $sp^2$ - hybridized carbon network depends on the nanotube diameter and chiral vector. Consequently, by varying these parameters a SWNT may act as an insulator, a semiconductor, or a metal [7].

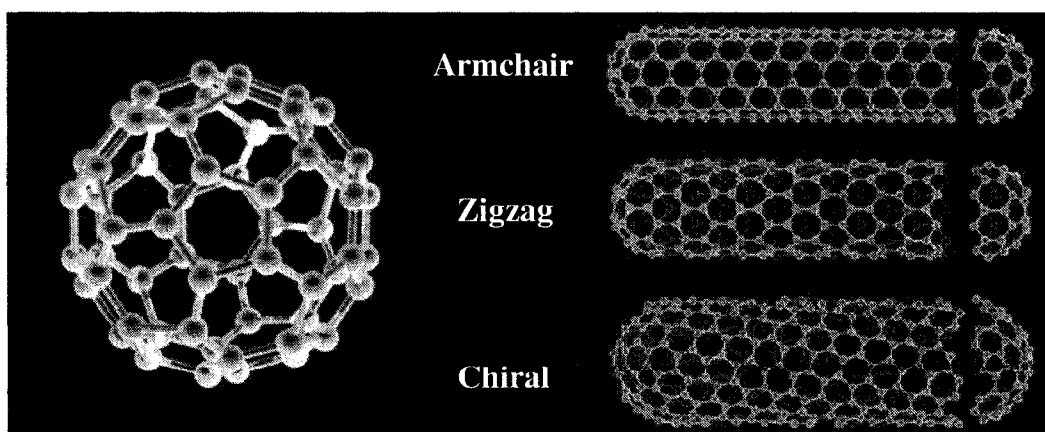


Figure 1.1 Representation of a  $C_{60}$  fullerene and SWNTs in three different chiralities [8].

After Dillon et al. in 1997 reported the condensation of molecular hydrogen on SWNT soot at cryogenic temperatures [9], an enormous research activity on the hydrogen storage capacity was propelled. At first, promising results reporting high hydrogen storage capacities under various experimental settings were published, in some cases surpassing the DOE Hydrogen goal. For example, Ye et al. [10] reported attaining a nearly 1:1 H/C ratio by submitting a SWNT sample at a temperature of 80 K to molecular hydrogen pressures greater than 40 bar. Dillon et al. [11] reported a 7% wt-hydrogen storage capacity for a purified SWNT sample at room temperature after exposure to molecular hydrogen at 0.666 bar.

Nonetheless, these promising capacity yields of hydrogen storage on SWNTs were not independently replicated by other research teams [12]. In fact, many of the later experimental capacities were minute in comparison. This variation in experimental results has been attributed to several factors. The purification stage is the most difficult part of the SWNT synthesis process [13-15]. Consequently, the relative purity level of the SWNT used in the various experiments is uncontrolled. Because impurities in the SWNT samples will play a role in the adsorption of hydrogen, impurity level deviations are bound to provoke inaccuracies when comparing obtained results. Furthermore, the diameter distribution of the nanotubes is known to affect the strength of interaction with adsorbates [16, 17]. At present, SWNT samples with particularly defined nanotube diameters cannot be synthesized or separated in large quantities. Consequently, the random nanotube diameter variation of the employed SWNT samples also factors into the above-described incongruence of the experimental results.

Experimental results of hydrogen physisorption on  $C_{60}$  have not been any more encouraging. At room temperatures, hydrogen adsorption has been determined to be of one hydrogen molecule per  $C_{60}$ , even after exposures at 2000 bar hydrogen pressures [18].

Physisorption has been the overwhelming focus of hydrogen adsorption studies on carbon nanomaterials. Physisorption potentials are characterized by a low binding energy, on the order of 10 to 100 meV [19]. Furthermore, determination of hydrogen storage capacities of carbon nanomaterials have been carried out by utilizing techniques that are not sensitive to carbon-hydrogen interactions, e.g., thermal desorption spectroscopy, thermal gravimetric analysis, and Brunauer-Emmett-Teller analysis [9-11, 18]. Consequently, desorbed hydrogen cannot be assuredly backtracked to its original adsorption state on the substrate. Moreover, due to reliance of physisorbed particles on dipole moments as one of the driving adsorption mechanisms [19, 20], the substrate temperature must often be kept low compared to room temperature in order to prevent perturbation of the adhered state by thermal motion of the substrate lattice. Such constraint undoubtedly complicates vehicular on-board hydrogen storage accessibility, as mentioned previously.

Existing hydrogen chemisorption studies of carbon nanomaterials [21-24], on the other hand, are confined to a few examples. Thus, these storage media still need to be further scrutinized in this respect to develop a better understanding of their hydrogen uptake capabilities. Compared to physisorption, chemisorption is characterized by the presence of an activation barrier and, in many cases, a high binding energy of the adsorbate to the substrate (up to several eV). It also involves the rearrangement of the

electronic orbitals of the participating atoms since a chemical bond is formed. As mentioned, hydrogen chemisorption on carbon nanomaterials requires an energy barrier to be overcome [23, 25, 26]; however, this adsorption is exothermic [16, 27]. Moreover, theoretical work signals that SWNT with tube radii smaller than 6.25 Å remain stable even after complete chemisorptive hydrogenation, indicating a prospective 7.5 %-wt. hydrogen storage capacity for this medium [16]. Nonetheless, the dissociation energy of molecular hydrogen is higher than the energy liberated by the chemisorption reaction [28]. Therefore, molecular hydrogen must first be dissociated into atomic hydrogen for its adsorption to take place.

In previous hydrogen chemisorption studies, methods used to crack molecular hydrogen have been (i) exposure of hydrogen to a hot tungsten filament, (ii) flowing hydrogen gas through a heated tungsten capillary tube, or (iii) generation of a hydrogen plasma. In the present thesis, an atomic hydrogen source based on thermal cracking of molecular hydrogen in a heated tungsten capillary tube was constructed, and the hydrogenation of C<sub>60</sub> and SWNT was studied. Note that the hydrogen dissociation step could potentially also be performed by transition-metal atoms decorating the surface of carbon-based nanomaterials [29]. Not only would metal adatoms serve as a dissociative catalyst but could also play an active role in the storage process; thus, increasing the storage capacity of the substrate. Yildirim and Ciraci [30], based on total energy calculations, predict that SWNT with high Ti coverage are capable of storing 8 %-wt. hydrogen. Additionally, Sun et al. [31] present first-principle studies that lithium-decorated C<sub>60</sub> may bond sufficient hydrogen to attain 9 %-wt. storage properties.

Although the present thesis does not report on hydrogen adsorption of *metal-decorated* nanomaterials, it does build a foundation upon which such future work can be carried out.

The structure of the present thesis is hereby explained. Chapter 2 describes the experimental techniques pertinent to the performed experimental series. Chapter 3 details the construction of the atomic hydrogen source, the principles behind its atomic hydrogen generation, and a characterization of its activity as a function of capillary tube temperature. Chapter 4 presents and discusses the results of the chemisorption studies on SWNT and C<sub>60</sub> storage matrices. Chapter 5 provides a summary of the entire work.



## CHAPTER 2

### EXPERIMENTAL METHODOLOGY

#### 2.1 Photoelectron Spectroscopy Principles

##### 2.1.1 Background

Photoelectron spectroscopy (PES) is an analytical tool for the study and characterization of the occupied electronic states of a sample surface. This spectroscopic technique is particularly useful in the analysis of surface elemental compositions, chemical bonds, and valence structures.

The basis for this extensively used experimental technique is the photoelectric effect, which was initially developed by Hertz [32], and later explained by Einstein.

In the photoemission event, an incident photon with energy  $h\nu$  excites an N-electron system from an initial state  $|\psi_i\rangle$  to a final state  $|\psi_f\rangle$ . In this process, one electron is excited from its ground state to a state above the vacuum level. The probability for this transition,  $w_{i \rightarrow f}$ , to occur (in the first order) can be calculated by Fermi's Golden Rule:

$$w_{i \rightarrow f} \propto \frac{2\pi}{\hbar} \left| \langle \psi_f | r | \psi_i \rangle \right|^2 \delta(E_f - E_i - h\nu), \quad (1)$$

where  $\delta$  describes the energy conservation law;  $r$  is the dipole operator; and  $E_f$  and  $E_i$  are the energies of the final and initial states, respectively [33].

Using an x-ray source, PES measures the current of the emitted photoelectrons versus their kinetic energy,  $E_k$ . In this context,  $E_k$  is defined by the difference of the photon energy,  $h\nu$ , the electron's binding energy (BE),  $E_B$ , and the work function,  $\Phi$ :

$$E_k = h\nu - E_B - \Phi \quad (2)$$

Depending on the source of excitation photons, PES is also called x-ray photoelectron spectroscopy (XPS) or ultraviolet photoelectron spectroscopy (UPS). In Figure 2.1, the photoemission processes involved in XPS and UPS are illustrated. For XPS analysis, Mg  $K_\alpha$  ( $h\nu=1253.6$  eV) or Al  $K_\alpha$  ( $h\nu=1486.6$  eV) x-ray photons are employed. UPS analysis is carried out with a gas discharge lamp emitting He I ( $h\nu=21.2$  eV) or He II ( $h\nu=40.8$  eV) ultraviolet light. An electron analyzer is required to detect the photoelectrons in an energy-dispersive manner, as illustrated in Figure 2.2.

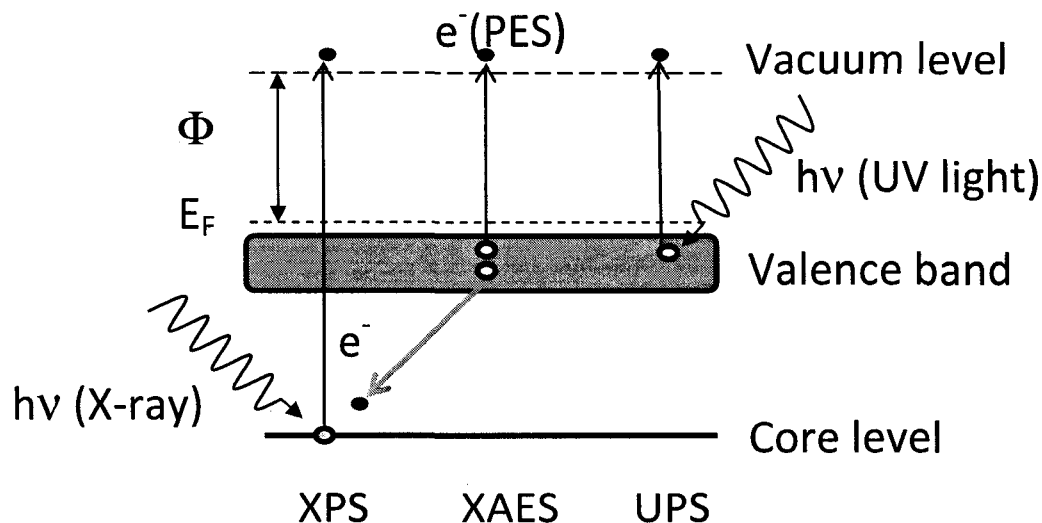


Figure 2.1 Schematic diagram of the XPS and UPS photoemission processes and the X-ray excited Auger electron spectroscopy (XAES) process in a semiconductor. For clarity, the conduction band has been omitted.

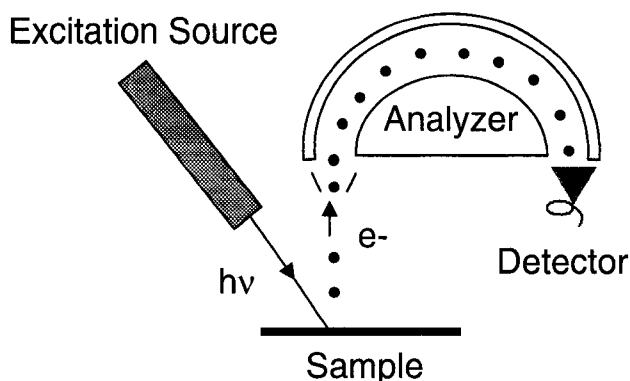


Figure 2.2 Schematic diagram of the PES experimental setup.

In order to prevent the photoelectrons from losing any kinetic energy on their way to the analyzer as a result of collisions with residual molecules in the sample environment, PES must be performed under ultra high vacuum (UHV) conditions (pressures in the order of  $10^{-10}$  mbar). UHV also allows for adequate experimental time periods without significant problems due to surface contamination. Since the accumulation of surface adsorbates can alter the chemical and electronic structure of the sample, and PES is a very surface sensitive method (see below), it is absolutely necessary to conduct PES in a UHV environment.

### 2.1.2 Electron Inelastic Mean Free Path

Although photons from the excitation sources used for the present experimental series are capable of penetrating several hundred nm (or more) inside the probed sample, the excited photoelectrons are collected from a surface-near region, defined by the small inelastic mean free path (IMFP),  $\lambda$ , in the Ångstrom range, which is dependent on the  $E_k$  of the photoelectron. It is this important phenomenon (inelastic scattering and the

associated mean free path) that makes the different modes of PES surface-sensitive techniques.

The fraction of unscattered electrons (i.e., those that contribute to a specific line in an XPS or UPS spectrum), can be described by  $e^{-\frac{d}{\lambda}}$  after a certain path length  $d$ . Thus, after a distance of  $\lambda$ , the number of electrons that still carry the original energy information is reduced to  $1/e$ . Because the relation of mean free path and kinetic electron energy shows a similar qualitative behavior in a large number of solids, it can be approximated by the so-called universal curve, shown in Figure 2.3.

For electrons with  $E_k \sim 30$  eV, the IMFP is approximately 3 monolayers. For electrons with  $E_k < 30$  eV,  $\lambda(E_k)$  increases and is proportional to  $\frac{1}{\sqrt{E_k}}$ , whereas for electrons with  $E_k > 30$  eV,  $\lambda \propto \sqrt{E_k}$ .

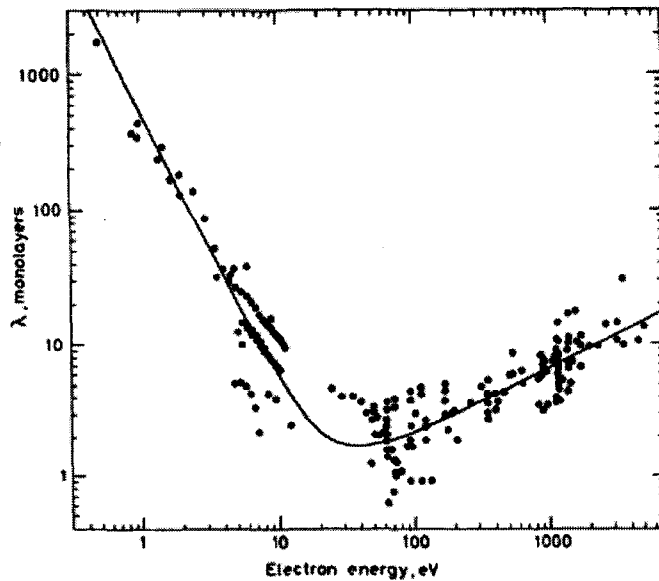


Figure 2.3 Universal curve of the inelastic mean free path of electrons in a solid [34].

### 2.1.3 XPS Analysis

Figure 2.4 presents an XPS spectrum of a C<sub>60</sub> layer on Au foil, in which the kinetic energies of the detected electrons were converted into binding energies using equation (2). Two different types of spectral lines can be observed in the spectrum relating to the two emission processes observable after x-ray excitation: (i) photoelectron lines and (ii) Auger lines. After a photoemission process, a core hole is left behind, which is rapidly filled by an electron from outer level. This relaxation process can emit a fluorescent photon, which conserves the energy difference between the involved states. However, the major relaxation route for relatively shallow core levels (i.e., in the soft x-ray regime below 1500 eV) concerns the emission of a second electron, known as an Auger electron (and its detection is denoted XAES for “x-ray excited Auger electron spectroscopy”). The kinetic energy of this Auger electron is independent of the excitation source, i.e., in particular independent of the incoming photon energy.

The nomenclature for the XPS lines, in spectroscopic notation, is: element, principal quantum number, and orbital angular momentum quantum number (in letter form), e.g., C 1s. If the probed line exhibits a spin-orbit splitting, the total angular momentum quantum number ( $j = l + s$ ) is given as a subscript, e.g., W 4f<sub>5/2</sub>. The nomenclature for the XAES lines, in x-ray notation, is: element, the three principal quantum numbers of the electrons participating in the process and a subscript representing the angular momentum, spin quantum number, and their coupling, e.g., O KL<sub>2</sub>L<sub>3</sub>.

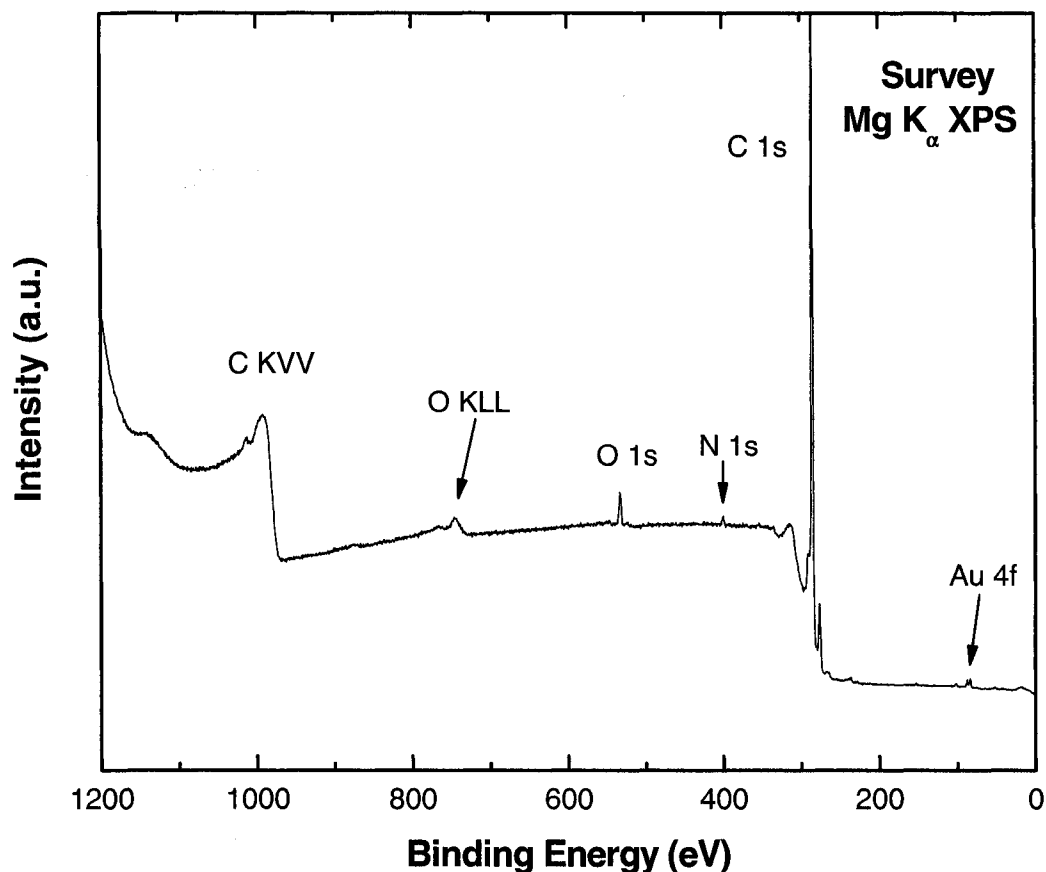


Figure 2.4 XPS survey spectrum of  $C_{60}$  on a gold substrate probed by  $Mg K_{\alpha}$  excitation

Because each element has its own set of electrons with unique binding energies, XPS (and XAES) is an advantageous technique that allows for the identification of elements and determination of their surface coverage on a sample (e.g., the weak N 1s line in Figure 2.4, which stems from residual solvent used in the sample preparation). The chemical composition of the sample can thus be ascertained by comparing the peaks of the XPS spectrum to standard reference spectra. Furthermore, the chemical environment also varies the position of the core level and Auger lines, also known as chemical shift, which makes the differentiation of various chemical states for a given element possible. This phenomenon can be foreseen from equation (1). On the initial state side, the

electron configuration of the atom is changed by the chemical binding. On the final state side, the interaction between the emitted electron and the remaining core hole, which can be partially shielded by the other electrons in the solid, is important [33]. The time needed to compensate the positive charge created by the core hole (the “core hole lifetime”) depends on the chemical bonding of the atom in the solid, also leading to a chemical shift. Via the Heisenberg uncertainty principle, the core hole lifetime also defines the natural line width of the XPS core level lines.

Other featured lines of interest are found on the high-binding energy side next to the core level lines. These are called satellite lines and originate from energy losses due to additional excitations during the photoemission process, such as shake-up/shake-off processes and plasmons [35, 36].

#### 2.1.4 UPS Analysis

When using a helium gas discharge lamp as an excitation source, the probing photon energy is in the ultraviolet regime. Only the valence levels can be characterized with this energy scale. Nevertheless, this technique is of great interest because it can probe the valence structure much better than XPS. Additionally, UV light has a much larger cross section for valence electrons than x-rays, and the line width of the UV source is much narrower, leading to much higher overall energy resolution.

With UPS, the valence band maximum (VBM) as well as the work function,  $\Phi$ , of the sample can be characterized. For the latter, the kinetic energy  $E_{k,min}$  of the slowest electrons emitted from the sample is measured relative to the kinetic energy of the Fermi edge,  $E_{k,F}$ . The work function can be calculated as follows:

$$\Phi = h\nu - (E_{k,F} - E_{k,min}) \quad (3)$$

## 2.2 Instrumentation

### 2.2.1 Introduction

The experiments presented in this thesis were performed in two conjoined surface analysis systems, the diagrams of which are shown in Figure 2.5. The analysis chamber of the Andere ESCA chamber is equipped with a XR50 SPECS twin anode x-ray source (Mg  $K_{\alpha}$  and Al  $K_{\alpha}$ ) and a gas discharge UV source (HeI/II). Most of the XPS measurements and the entirety of the UPS measurements were performed in this chamber. The measurement detection was performed with a SPECS PHOIBOS 150MCD electron analyzer. With the installation and optimization of the SCIENTA system (Figure 2.5 b) during the course of this thesis, XPS scans with monochromatized Al  $K_{\alpha}$  excitation (and hence better energy resolution) became possible. This took place in the analysis chamber of the SCIENTA system, which is equipped with a SCIENTA R4000 electron analyzer. The base pressure for both analysis chambers is generally better than  $2.0 \times 10^{-10}$  mbar.

Hydrogenation treatments and sample storage during the course of the experimental series took place in the preparation chamber of the system to which the atomic hydrogen source (AHS) was mounted at the time (see Figure 2.5; further details are provided in the experimental procedure sections of the various experimental series). For experiments in the SCIENTA system, an SRS RGA300 quadrupole mass spectrometer was also used in the preparation chamber. The base pressures for the two preparation chambers were not as low as those found in the analysis chambers, but were routinely in the  $10^{-10}$  mbar range.



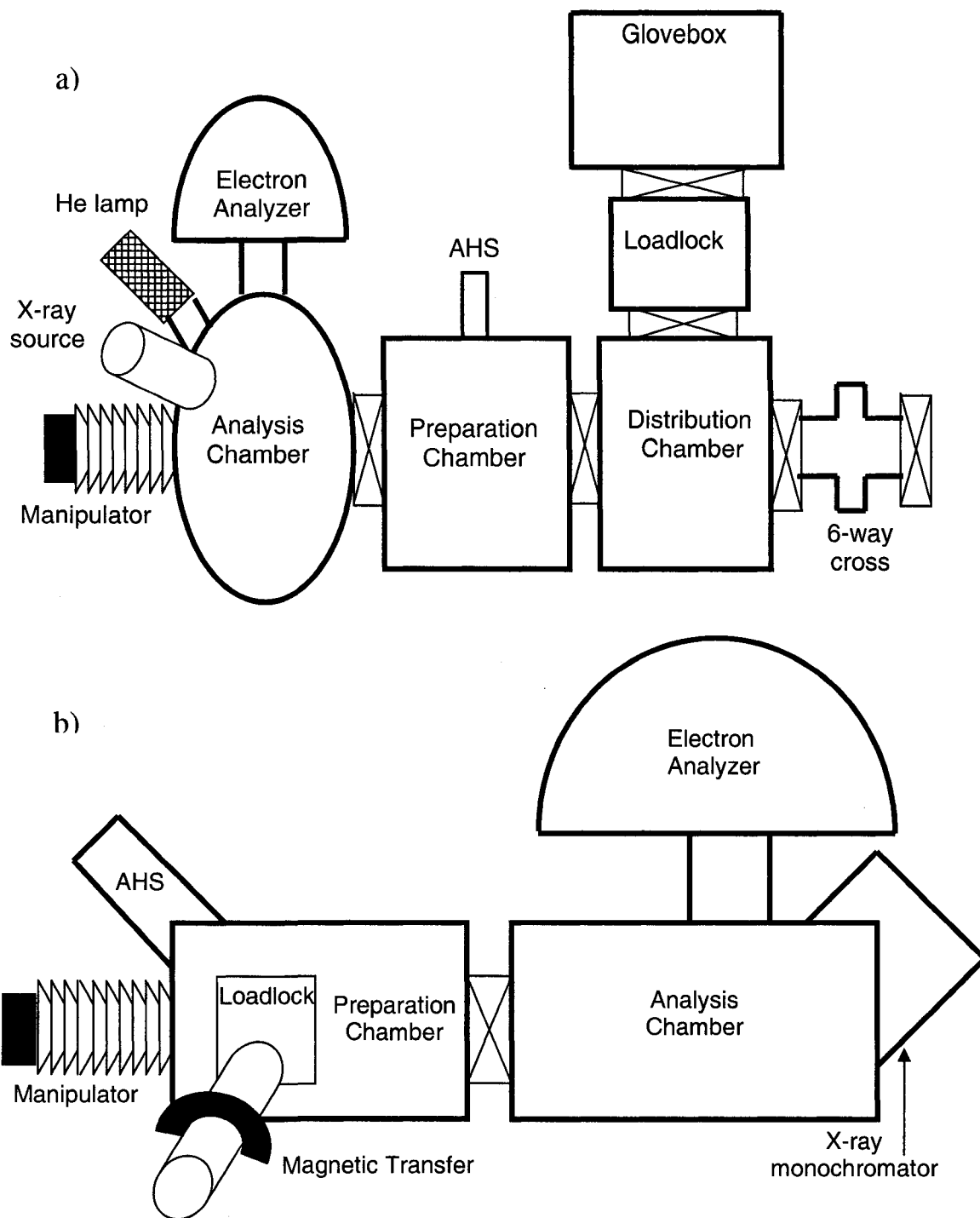


Figure 2.5 Diagrams of the two surface analysis systems (electron analyzer in parenthesis): (a) Andre ESCA (SPECS PHOIBOS 150MCD); (b) SCIENTA (SCIENTA R4000); the 6-way cross in (a) and the preparation chamber in (b) are connected. In each diagram, the position of the atomic hydrogen source (AHS) is indicated.

### 2.2.2 Concentric Hemispherical Analyzer

Both the SPECS PHOIBOS 150MCD electron analyzer and the SCIENTA R4000 are concentric hemispherical electron analyzers (CHA). As sketched in Figure 2.2, the CHA consists of two metal hemispheres. One hemisphere is shaped concave, and the other convex. They are arranged in such a way that their centers of curvature are coincident. While the inner hemisphere is charged positively, the outer hemisphere is charged negatively. Electrons are injected into the gap between the hemispheres through an entrance slit, the width of which has an influence on the overall spectral resolution and the count rate. If the electrons are traveling very fast, they will impinge on the outer hemisphere. If they are traveling very slowly, they will be attracted to the inner hemisphere. Hence only electrons in a narrow energy region (called the pass energy) succeed in passing through the hemispheres and into the detector. As with the entrance slit width, the pass energy is a suitable parameter to control the overall spectral resolution and the count rate.

The energy resolution ( $\Delta E/E_0$ ) of the CHA can be expressed as follows:

$$\frac{\Delta E}{E_0} = \frac{s \cdot E_{\text{pass}}}{2r} \quad (4)$$

where  $s$  stands for the entrance slit width (in mm.),  $E_{\text{pass}}$  stands for the selected pass energy, and  $r$  stands for the CHA hemisphere radius. For the SPECS PHOIBOS 150MCD electron analyzer,  $r = 150\text{mm}$  and  $s = 7\text{mm}$ ; whereas for the SCIENTA R4000,  $r = 200\text{mm}$  and  $s = 0.8\text{mm}$ .

The electron analyzers are calibrated with the Ag  $3d_{5/2}$ , Au  $4f_{7/2}$ , and the Cu  $2p_{3/2}$  photoelectron lines of the corresponding metals. By linearly fitting the measured kinetic

energies ( $E_{k,meas}$ ) of the core level photoelectrons to reference values ( $E_{k,ref}$ ) [34], an energy scale correction is obtained. For the PHOIBOS analyzer and Mg  $K_{\alpha}$  excitation, the energy correction, in eV, was  $E_{k,ref} = 0.85145 + 1.00006 \cdot (E_{k,meas})$  for 50 eV pass energy and  $E_{k,ref} = 0.81017 + 0.99993 \cdot (E_{B,meas})$  for 10 eV pass energy. For the SCIENTA R4000 analyzer monochromatized Al  $K_{\alpha}$  excitation, the energy correction, in eV, was  $E_{k,ref} = 1486.6 - [0.1 + (1.00007)(1486.6 - E_{k,meas})]$  for 50 eV pass energy.

### 2.2.3 Sample Handling

Sample introduction into the analysis chamber is done by a series of successive sample transfers.

First, samples are introduced from air into the glove box that is filled with dry nitrogen from a liquid nitrogen dewar. In the glove box, the sample is mounted on suitable sample holders.

For experiments in the Andere ESCA, the sample sits on a metal stub (VG ESCA stub) which is placed from the glove box onto a trolley holder in the loadlock chamber. Following evacuation, the sample is transferred, first from the loadlock to the distribution chamber, to the preparation chamber, and then into the analysis chamber with the help of a moving cart. This is achieved by a sequence of openings and closings of intervening gate valves, and of mechanical transfers from one trolley to another and then onto the sample manipulator using ‘wobblesticks’. A spring clip on the fork grips the sample stub firmly.

Once the sample is transferred into the analysis chamber, it needs to be positioned accurately for analysis by means of a manipulator. It provides X and Y lateral motions of  $\pm 12.5$  mm and a Z translation motion of 50 mm. The sample position is optimized

using a video camera that “looks” along the entrance axis of the electron spectrometer, as well as by monitoring the XPS count rate of a prominent core level line as a function of sample position.

In SCIENTA, the successive sample transfer is vastly similar. In the SCIENTA system, two different pathways are available to introduce samples from air, namely through the glove box and the distribution chamber (using a “home-made” adaptor), as described above, or through a separate load lock at the SCIENTA system itself. Samples are secured to sample plates (instead of metal stubs), and sample transfer from the SCIENTA loadlock to the preparation chamber is done via a magnetic transfer rod, from which the sample is transferred to an automated manipulator by use of pincer-grip wobblesticks. The automated manipulator carries the sample into the analysis chamber, reducing the probability of dropping a sample in the SCIENTA system.

#### 2.2.4 Atomic Hydrogen Source

As mentioned in Chapter 1, an atomic hydrogen source was constructed in the framework of this thesis with the purpose of producing atomic hydrogen in an UHV environment. This is carried out by flowing molecular hydrogen gas through a resistively-heated tungsten capillary tube.

Temperature modulation of the capillary tube is achieved by submitting it to electron bombardment, followed by a supply of high voltage. Varying the applied voltage changes the capillary tube temperature accordingly.

Chapter 3 discusses the principles of the operation of the atomic hydrogen source in greater detail.

## CHAPTER 3

### ATOMIC HYDROGEN SOURCE

#### 3.1 Introduction

The constructed atomic hydrogen source (AHS) was designed by following a “do-it-yourself” instructive paper [37] as a guide. The AHS produces a beam of atomic/molecular hydrogen, essentially by letting molecular hydrogen gas flow through a heated small-diameter tungsten (W) capillary tube. As will be explained in Section 3.2, the high temperature itself is not responsible for the hydrogen dissociation, but allows tungsten to act as a catalyst in the generation of atomic hydrogen. Molecular hydrogen is prone to experience dissociative chemisorption on metal surfaces [20]. Thus, it is the desorption process of the chemisorbed hydrogen that determines whether the escaping particle is in atomic or molecular form. The surface temperature plays a primary role in the kinetics of this process. Consequently, beams with different atomic/molecular hydrogen ratios can be attained by modulating the W capillary tube temperature,  $T_w$ .

In order to increase  $T_w$  within the range required for atomic hydrogen generation, the capillary tube is submitted to a positive high voltage bias, while simultaneously being bombarded by electrons from a strategically located tungsten filament. This mediated power surge induces vibrations in the atomic lattice of the capillary tube, which raises the tube temperature.

## 3.2 Hydrogen dissociation by tungsten

### 3.2.1 Introduction

Tungsten's ability to dissociate molecular hydrogen into atomic hydrogen was first recorded almost a century ago, by Langmuir [38]. This event was realized by observing the effects of heating a W wire between a temperature range of 1300-2500 K in a H<sub>2</sub> atmosphere of  $10^{-2} - 10^{-3}$  mTorr. The atomic hydrogen formed by the H<sub>2</sub> molecules striking the W filament would stick to the glass walls of the experimental apparatus; thus, eliciting a "disappearance" of hydrogen pressure. Ever since, numerous studies concerning the interaction of hydrogen with the surface of tungsten have been conducted [39].

### 3.2.2 Hydrogen Dissociation Mechanism

As a hydrogen molecule approaches a tungsten surface, it becomes attracted by van der Waals forces exerted by the surface atoms. This results in the molecule accelerating towards the metal surface and ultimately colliding with it [20, 40]. There are several possible outcomes for the impinging molecule: (i) elastic scattering, whereby the molecule is directly reflected from the surface; (ii) inelastic scattering, whereby the molecule is also reflected upon the collision, but not prior to an energy exchange between the molecule and the surface; (iii) direct dissociation, whereby the molecule's kinetic energy is sufficient to surmount the dissociation activation energy resulting in the chemisorption of the atoms on the metal surface ("chemisorbed state"); and (iv) indirect dissociation, whereby the molecule remains as an entity trapped in a molecular interaction potential, prior to becoming dissociated or free from this physisorption (or "precursor") state [40]. Although a weakly-bound precursor state for hydrogen

adsorption may be present for W at low temperature [41], at room temperature and above, the direct dissociation pathway seems to be the most prominent hydrogen interaction with the W surface. Figure 3.1 shows a one-dimensional view of the potential energy profile, which confirms that the dissociative chemisorption of a hydrogen molecule is the dominant process as it approaches a tungsten surface.

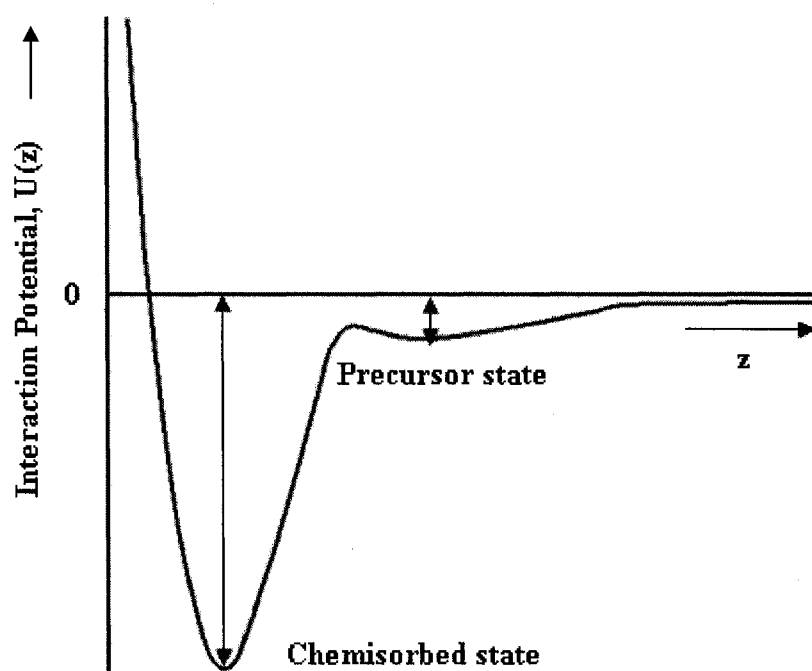


Figure 3.1 One-dimensional view of the potential energy profile (adapted from [20]) showing that the dissociative chemisorption of a hydrogen molecule is the dominant process as it approaches a tungsten surface.  $z$  is the distance of the  $H_2$  molecule from the tungsten surface.

At room temperature, the initial sticking coefficient,  $s_0$ , of  $H_2$  on W indicates a non-activated chemisorption process. This is also illustrated in Figure 3.1 by the fact that the

low energy barrier a precursor state hydrogen molecule must overcome to transform into a chemisorbed state has a negative interaction potential,  $U(z)$ . Under this environment,  $s_0$  has a value of 0.5-0.65 [40], which indicates that a hydrogen molecule must undergo approximately two collisions against a perfectly clean W surface to dissociatively chemisorb to it. In doing so, two adsorption sites become occupied. As the surface fractional coverage (i.e, the ratio between the number of adsorption sites occupied and the total number of adsorption sites available),  $\theta$ , increases due to further hydrogen chemisorption onto the W surface, the probability of lateral chemisorbed hydrogen interactions increases, leading to recombination of hydrogen adatoms and its desorption as molecular hydrogen [42].

With increasing  $T_w$ , the vibrational amplitude of the surface atoms increases, allowing for movement of the hydrogen adatoms over the W surface (i.e., two-dimensional gas properties). Thus, for  $T_w < 1200$  K, the main hydrogen desorption mode results in chemisorbed atomic hydrogen recombining to molecular hydrogen. At  $T_w \sim 1200$  K, desorption of atomic hydrogen commences [43]. At this temperature range,  $\theta$  is low enough to significantly hinder hydrogen adatom recombination and allow surface atoms to eject as atoms. At this temperature and at hydrogen pressures greater than  $10^{-6}$  Torr, the formation of atomic hydrogen is proportional to the square root of the molecular hydrogen pressure,  $\sqrt{P_{H_2}}$ , and follows a rate,  $V_{AH}$  (atoms  $\text{cm}^{-2} \text{s}^{-1}$ ), that can be expressed by the following formula [42, 44, 45]:

$$V_{AH} = A \cdot \sqrt{P_{H_2}} \cdot e^{-E_a / kT} \quad (5)$$

where A stands for a pre-exponential factor,  $E_a$  stands for an activation energy, k is the Boltzmann constant, and T is the temperature of the tungsten surface in Kelvin.



However, this  $\sqrt{P_{H_2}}$ -rate law has been observed to cease with  $T_w$  greater than 1600 K and  $P_{H_2}$  lower than  $10^{-6}$  Torr [43, 44]. Under these parameters, the rate of atomic hydrogen formation instead becomes linearly dependent on  $P_{H_2}$ .

Since under the latter parameters, the impinging rate of molecular hydrogen on the W surface becomes a limiting factor for atomic hydrogen formation, increasing the surface reaction area will augment atomic hydrogen production. Employing a W capillary tube through which molecular hydrogen is flowed is an appropriate way to attain a greater reaction surface area.

### 3.3 AHS Atomic Hydrogen Production

#### 3.3.1 AHS Setup

Figure 3.2 displays the main instrument components used to generate atomic hydrogen, and a photo of the source is shown in Figure 3.3. The flow of molecular hydrogen gas into the UHV system is regulated by a leak valve. Molecular hydrogen gas flows through the gas line, which is connected to the W capillary tube by using a stainless steel adaptor. The gas line has a ceramic insulator component welded to it in order to restrict the applied high voltage (HV) solely to the W capillary tube. The source of the electrons employed in the AHS is a tungsten filament taken from a commercial automotive light bulb (OSRAM 7528). As can be seen, it is situated close to the capillary tube in order to heat the W tube and thus facilitate the generation of atomic hydrogen.

The capillary temperature was measured via a type C thermocouple. The thermocouple wires were tightly pressed against the capillary tube by means of a tantalum fastening ring. The temperature reading of the thermocouple system was

compared against temperature measurements taken with a Raytek MM1ML High-Performance Infrared Thermometer [46]. The emissivity value of 0.35 given in the pyrometer's manual for tungsten was used for calibration. For all settings, the pyrometer measurements were approximately 200 K below the thermocouple temperature outputs. This reading variation can be attributed to the nature of the pyrometer temperature measurement. For the actual measurement distance (pyrometer  $\leftrightarrow$  capillary) a measuring spot size of approximately 3-mm in diameter could be estimated. Due to the capillary tube's dimensions (1.6 mm outer diameter), it is expected that the cooler capillary tube background is also factored into the pyrometer's temperature reading. Throughout this thesis, we will therefore report the temperature readings taken from the thermocouple,

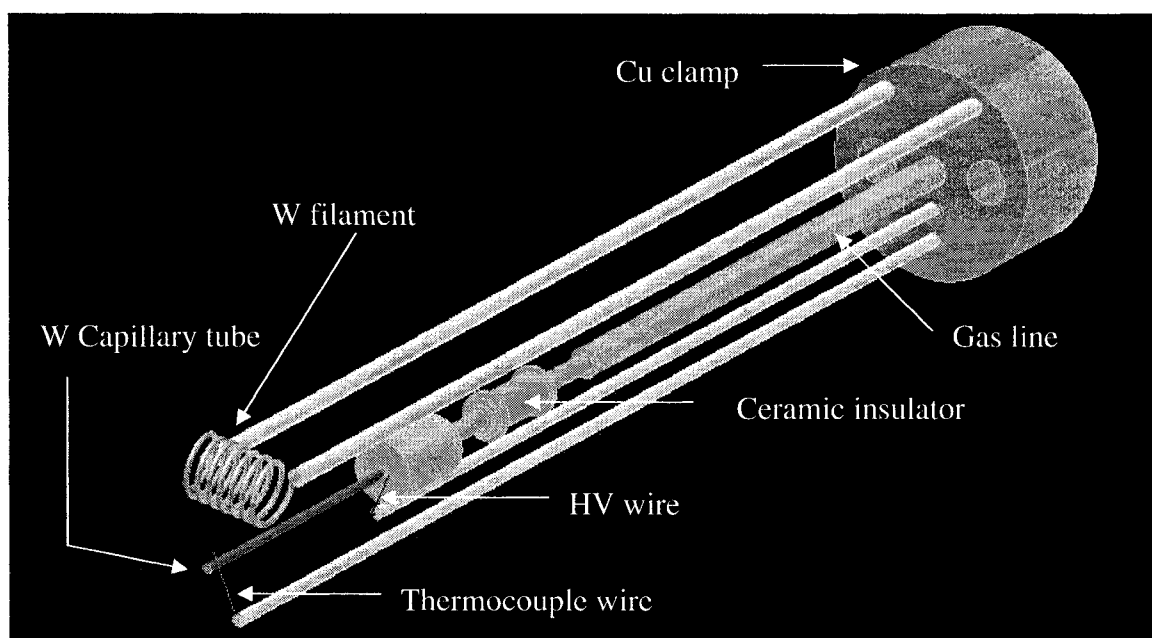


Figure 3.2 Schematic diagram of the AHS components relevant for atomic hydrogen generation.

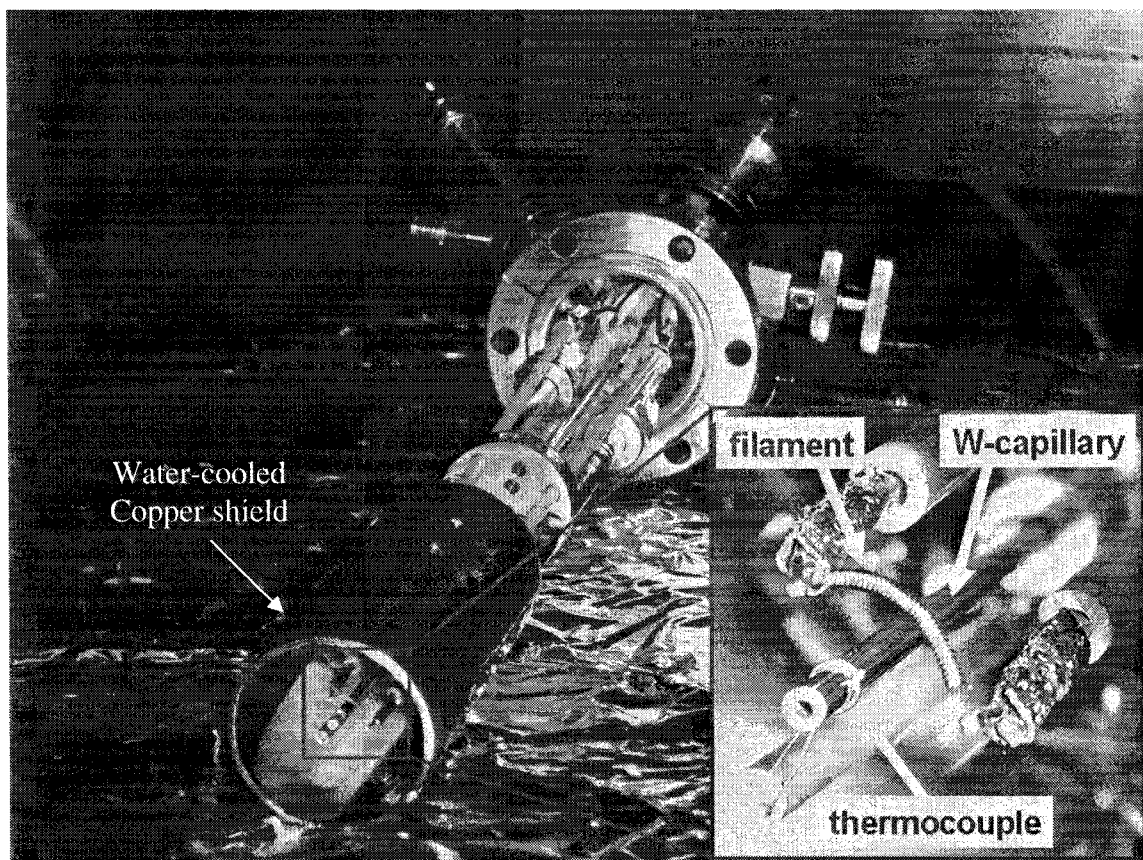


Figure 3.3 Photograph of the constructed AHS, inset shows the principle components relevant for atomic hydrogen generation.

which are assumed to be accurate to within 25 K.

In order to minimize sample damage caused by the heat emerging from the capillary tube or by filament-emitted electrons, the AHS was equipped with a water-cooled copper shield, shown in Figure 3.3. Because copper has a high vapor pressure compared to other metals, great effort was dedicated to ensure that this copper shield would not be in itself a source of contamination due to insufficient cooling.

### 3.3.2 AHS Activity Characterization via Mass Spectroscopy

To determine an adequate  $T_w$  range to optimally dissociate molecular hydrogen and produce atomic hydrogen, a series of Mass Spectroscopy (MS) runs were performed. In these experiments, the UHV system hydrogen equilibrium pressure,  $\Delta P_{H_2}$ , established by the difference of the introduced molecular hydrogen flux and the flux evacuated by the UHV system's pumps, was maintained constant and the  $T_w$  was varied. The partial pressures for mass/charge ratios ( $m/z$ ) of 1 and 2 (i.e.,  $P_{AH}$  and  $P_{H_2}$ ) were recorded and evaluated. Although  $P_{H_2}$  does not equal  $\Delta P_{H_2}$ , when the AHS is off both values are approximately the same.

The  $T_w$  was raised to the desired temperature; the operational procedure for this process is described more in detail in Section 2.2.5. For a temperature of 298 K, molecular hydrogen gas was introduced without heating the capillary of the AHS. For a temperature of 400 K, the AHS filament was turned on; without supplying a HV bias, the W capillary tube would then reach 400 K after approximately 5 min. For all higher temperatures, both the AHS filament as well as the HV bias was used. Molecular hydrogen gas was introduced until the desired equilibrium pressure was reached. Five measurements at  $m/z$  values of 1 and 2 were taken for each temperature value before the  $T_w$  was raised to the next temperature. Each set of mass spectroscopy runs for a particular  $T_w$  took approximately 3 minutes. These measurements were then averaged for analysis of results.

Figure 3.4 presents the  $P_{AH}/P_{H_2}$  ratios for five different equilibrium hydrogen pressures as a function of  $T_w$ . The y-axis error bars show the standard deviation of the five measurement sets of the partial pressure ratios. It is conclusive that atomic hydrogen

formation is found for AHS operation at  $T_w \sim 1500$  K and above, as seen from the significant increase in the  $P_{AH}/P_{H_2}$  ratios at all equilibrium pressures.

Several factors lead to believe that the dissociation degree is considerably greater than that shown by the detected MS  $P_{AH}/P_{H_2}$  ratios in Figure 3.4. First, the mass spectrometer was located at a distance of about 30 cm from the W capillary tube exit and second, in a  $215^\circ$  angle position. Thus, the atomic/molecular hydrogen beam does not stream directly into the mass spectrometer.

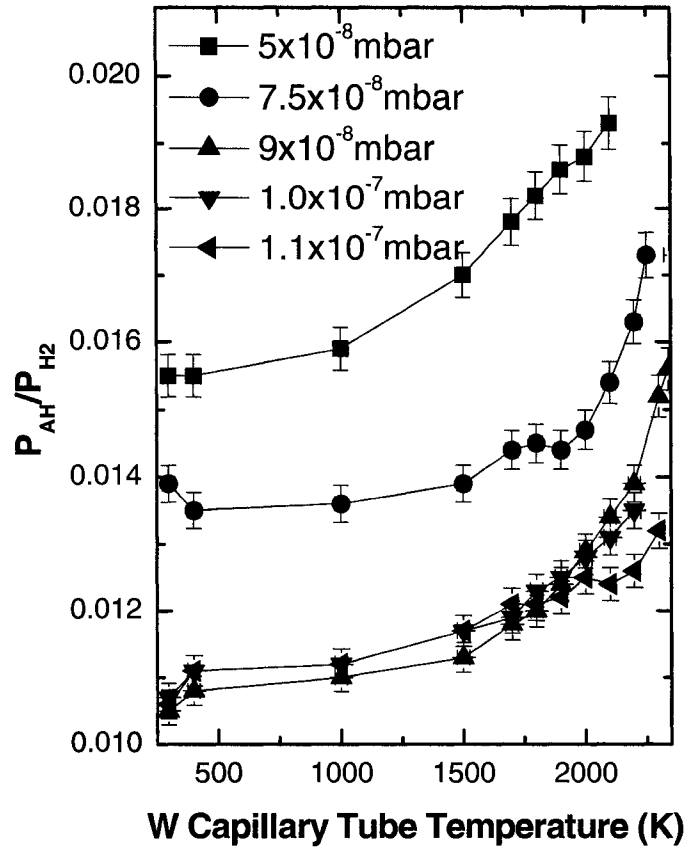


Figure 3.4 Measured  $P_{AH}/P_{H_2}$  ratios as a function of  $T_w$  for the five different  $\Delta P_{H_2}$  given in the legend.

Since the atomic/molecular beam has a small angular distribution [47, 48], a predominant fraction of the produced atomic hydrogen hits the system's chamber walls, which consequently leads to recombination into molecular hydrogen [49]. Thus the detected amount of atomic hydrogen by the mass spectrometer is greatly diminished and the molecular hydrogen signal increases due to the recombination taking place. In consequence, an underestimated  $P_{\text{AH}}/P_{\text{H}_2}$  ratio would be measured. Furthermore, there is an interfering intrinsic atomic hydrogen formation involved in the operation of the Mass Spectrometer (i.e., the hydrogen fragmentation pattern) as well as in the operation of the AHS (below the  $T_{\text{W}}$  required for atomic hydrogen generation). In both cases, molecular hydrogen could dissociate when it comes in contact with the hot filaments in the MS ( $\text{ThO}_2/\text{Ir}$ ) or the AHS (W). This further influences the accuracy of the  $P_{\text{AH}}/P_{\text{H}_2}$  measurement since the detected atomic hydrogen could be due to this “background” atomic hydrogen production.

In summary, the characterization of the AHS activity gives a qualitative yield, rather than a quantitatively accurate number. Furthermore, in order to use the MS results even as a qualitative measure for the atomic hydrogen generated by the AHS, the background signal must be corrected, as discussed below.

Examination of the  $P_{\text{AH}}/P_{\text{H}_2}$  ratios at 298 K (i.e., no “background” atomic hydrogen produced by the AHS filament and no atomic hydrogen deliberately produced in the capillary) for the five different analyzed  $\Delta P_{\text{H}_2}$  in Figure 3.4 suggests that the atomic hydrogen generation of the  $\text{ThO}_2/\text{Ir}$  filament in the mass spectrometer follows a  $\sqrt{P_{\text{H}_2}}$  - proportional rate, similar to a W surface at hydrogen pressures above  $10^{-6}$  mbar (see Section 3.1), as shown in Figure 3.5. From Equation 5, it is revealed that  $P_{\text{AH}}$  is

proportional to  $\sqrt{\Delta P_{H2}}$ . Assuming  $P_{H2} \approx \Delta P_{H2}$  leads to  $P_{AH}/P_{H2}$  being proportional to  $(\Delta P_{H2})^{-1/2}$ .

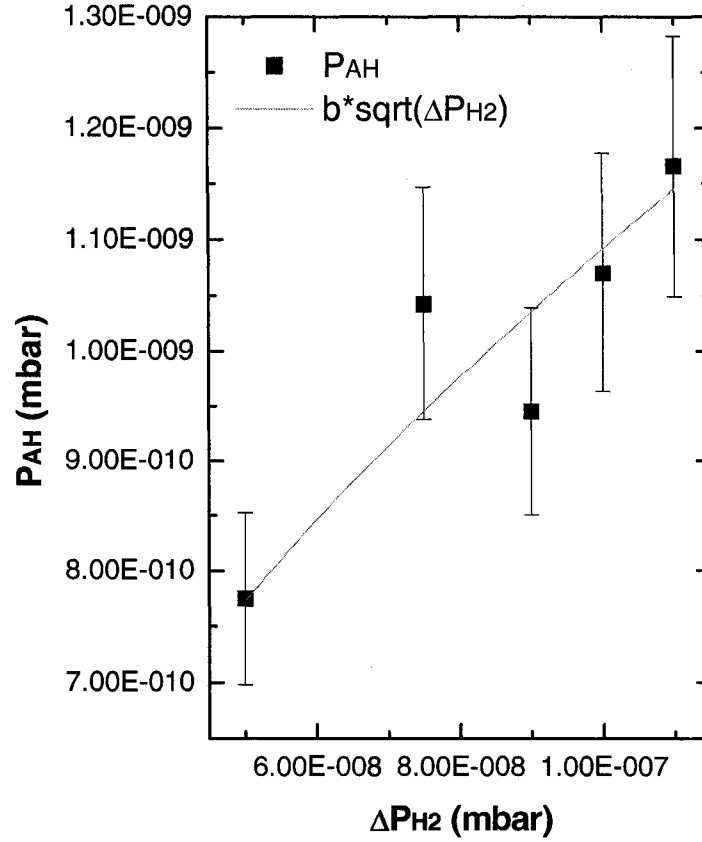


Figure 3.5 Mass spectrometer  $P_{AH}$  background as a function of  $\Delta P_{H2}$ . Constant  $b = 3.45 \times 10^{-6}$ .

Assuming that the  $\text{ThO}_2/\text{Ir}$  MS filament temperature remained constant for the different  $\Delta P_{H2}$  MS measurements, when comparing the  $P_{AH}/P_{H2}$  ratio for a given  $\Delta P_{H2}$ , i, to that of a different  $\Delta P_{H2}$ , ii, the pre-exponential and exponential factors of Equation 5 cancel. Thus, the following expression is obtained:

$$\frac{(P_{AH}/P_{H_2})_i}{(P_{AH}/P_{H_2})_{ii}} \approx \frac{\sqrt{\Delta P_{H_2 ii}}}{\sqrt{\Delta P_{H_2 i}}} \quad (6)$$

Plugging in the  $\Delta P_{H_2}$  employed in the MS runs and the obtained  $P_{AH}/P_{H_2}$  ratios in equation (5), it becomes apparent that the atomic hydrogen background signal produced by the MS filament indeed follows a  $\sqrt{P_{H_2}}$ -proportional rate, as presented in Table 3.1.

In order to correct the detected overall atomic hydrogen concentration for the “background” signal (from the MS and AHS filament), the 400 K  $P_{AH}/P_{H_2}$  value of the different  $\Delta P_{H_2}$  MS runs were subtracted from the  $P_{AH}/P_{H_2}$  values for higher  $T_w$  and are displayed in Table 3.2. After factoring for the difference of  $\Delta P_{H_2}$  employed in the MS runs, no significant increase of atomic hydrogen formation was detected by increasing  $\Delta P_{H_2}$  (see Table 3.3). This is not expected since one would assume that a higher  $\Delta P_{H_2}$  would result in a greater number of molecules colliding with the interior of the W capillary tube. On the contrary, though there is a pronounced scattering of the data, one can observe that the lowest- $\Delta P_{H_2}$  seemed to fare slightly better than the rest, as presented in Table 3.3. This observation may be explained by a greater mean free path of the atomic hydrogen at a lower  $\Delta P_{H_2}$ . This also means that a higher  $\Delta P_{H_2}$  would obscure the detection of a greater quantity of atomic hydrogen produced at higher pressure conditions.

Thus, in summary, it is apparent from the results of the AHS operation characterization, that the formation of atomic hydrogen is observed at  $T_w = 1500$  K and above. A more detailed discussion of the choice of optimal operating temperature will be given in the following chapter. With the current experimental set-up, it is not possible to derive the exact degree of molecular hydrogen dissociation. Nonetheless, it is safe to



Table 3.1 Comparison of the calculated square root values ratios of the five analyzed  $\Delta P_{H_2}$  with their respective  $P_{AH}/P_{H_2}$  ratios. Subset i represents the value for  $\Delta P_{H_2} = 5.00E-08$  mbar and subset ii for the different hydrogen equilibrium pressures. The values are compared to the  $P^{1/2}$  formation rate model (see text).

$P_{H_2}$ (mbar)	$\sqrt{\Delta P_{H_2}}$	$\frac{\sqrt{\Delta P_{H_2}ii}}{\sqrt{\Delta P_{H_2}i}}$	$P_{AH} / P_{H_2}$	$\frac{(P_{AH} / P_{H_2})i}{(P_{AH} / P_{H_2})ii}$	%-diff.
5.00E-08	2.24E-04	1.00	0.0155	1	-
7.50E-08	2.74E-04	1.22	0.0139	1.115	+9.37
9.00E-08	3.00E-04	1.34	0.0105	1.476	-9.55
1.00E-07	3.16E-04	1.41	0.0107	1.449	-2.40
1.10E-07	3.32E-04	1.48	0.0106	1.462	+1.42

Table 3.2 Measured  $P_{AH}/P_{H_2}$  values of the different  $\Delta P_{H_2}$  MS runs as a function of  $T_w$  after subtraction of the “background” atomic hydrogen signal (see text).

$T_w$ (K)	$5.0 \times 10^{-8}$ mbar	$7.5 \times 10^{-8}$ mbar	$9. \times 10^{-8}$ mbar	$1.0 \times 10^{-7}$ mbar	$1.1 \times 10^{-7}$ mbar
1000	0.0004	0.0001	0.0002	0.0001	0.0001
1500	0.0015	0.0004	0.0005	0.0006	0.0006
1700	0.0023	0.0009	0.0010	0.0008	0.0010
1800	0.0027	0.0010	0.0012	0.0012	0.0010
1900	0.0031	0.0009	0.0016	0.0014	0.0011
2000	0.0033	0.0012	0.0021	0.0017	0.0014
2100	0.0038	0.0019	0.0026	0.002	0.0013

Table 3.3 Detected  $P_{AH}$  of the different  $\Delta P_{H_2}$  MS runs as a function of  $T_w$  relative to the  $\Delta P_{H_2}=5.0 \times 10^{-8}$  mbar  $P_{AH}$  values, differences in  $\Delta P_{H_2}$  have been factored.

$T_w$ (K)	$5.0 \times 10^{-8}$ mbar	$7.5 \times 10^{-8}$ mbar	$9. \times 10^{-8}$ mbar	$1.0 \times 10^{-7}$ mbar	$1.1 \times 10^{-7}$ mbar
1000	1	0.38	0.90	0.50	0.55
1500	1	0.40	0.60	0.80	0.88
1700	1	0.59	0.78	0.70	0.96
1800	1	0.56	0.80	0.89	0.81
1900	1	0.44	0.93	0.90	0.78
2000	1	0.55	1.15	1.03	0.93
2100	1	0.75	1.23	1.05	0.75

assume that the atomic hydrogen production of the AHS is substantially greater than that produced by the mass spectrometer  $ThO_2/Ir$  filament. This is corroborated by the observed changes of several PES spectral lines after sample hydrogenation treatments of  $\Delta P_{H_2} = 1.0 \times 10^{-6}$  mbar (1 mbar = 0.7501 Torr) and  $T_w = 1700$  K, as will be presented in the following chapter.

## CHAPTER 4

### RESULTS AND DISCUSSION

#### 4.1 Introduction

The results of three hydrogenation series are presented and discussed in this chapter. These experimental series consisted of: (i) a W capillary tube temperature ( $T_w$ )-dependent hydrogenation series of SWNT, (ii) an atomic hydrogen adsorption/desorption cycling series of SWNT, and (iii) a hydrogenation series of  $C_{60}$ .

As will be discussed in detail in the following sections, the first experimental series shows a direct correlation between the XPS C 1s line position and spectral width of SWNTs and the degree of exposure to atomic hydrogen. Changes in the sample's valence band (VB) are also observed as a result. The second hydrogenation series shows that such changes of the SWNT electronic structure are reversible by heating the treated sample. The third experimental series shows that hydrogenation-induced electronic structure changes can also be observed for  $C_{60}$ , similar to the case of SWNT. Due to the molecular characteristic of  $C_{60}$ , the hydrogen-induced modifications observed in the valence states are even more pronounced than in the case of SWNTs.

#### 4.2 Hydrogenation Study of SWNT as a Function of Atomic Hydrogen Exposure

##### 4.2.1 Experimental Procedure

The SWNT powder employed in this study was obtained from a commercial vendor,

Carbon Nanotubes Inc. (Batch # P0288). According to their product description [50, 51], all carbon nanotubes are single-walled with a mean diameter of 1.0 nm. The presence of amorphous carbon and iron catalyst (employed during the SWNT synthesis process), is less than 5 %-wt. and 12 %-wt., respectively.

The sample used in this experimental series was prepared by pressing the SWNT powder on a 1-cm<sup>2</sup> square-shaped indium (In) foil, which was previously cleaned by ultrasonication in isopropanol for one hour. The preparation of the sample was performed in a nitrogen-filled glovebox. The SWNT sample on In foil was mounted onto a sample carrier stub for transferring throughout the UHV system. Due to the softness of the In foil, it could be carefully pressed to fit the contour of the stub. This contact was helpful in preventing sample charging effects during the electron spectroscopy experiments.

The SWNT sample was introduced into the UHV system loadlock chamber and left there overnight to minimize any degassing from the sample. From there, it was transferred to other chambers of the system by means of a mechanical conveying trolley system, as explained in Section 2.2.3.

The hydrogenation treatment was performed in the preparation chamber of the Andere ESCA system. The distance between the sample and the W capillary tube opening of the AHS was about 10 cm. It was desirable to have the sample as close to the capillary tube in order to maximize the fraction of generated hydrogen atoms actually impinging onto the sample. The hydrogen equilibrium pressure,  $\Delta P_{H_2}$ , was held at  $1.0 \times 10^{-6}$  mbar during the two-minute hydrogenation treatment periods. The temperature of the W capillary

( $T_w$ ) employed for the series of hydrogenation treatments were: 298 K, 1000 K, 1500 K, 1700 K, 1800 K, 1850 K, 1900 K, 1950 K, 1975 K, 2000 K, and 2050 K.

The sample was probed by XPS using Mg  $K_\alpha$  x-rays ( $h\nu=1253.6$  eV) and UPS using He I ( $h\nu= 21.2$  eV) and He II ( $h\nu= 40.8$  eV) UV light. The XPS survey scans were performed using a 50 eV pass energy with 0.5 eV energy steps. The electron analyzer was set to an entrance slit of 7 mm. From equation (4) of Section 2.2.2, the analyzer energy resolution ( $\Delta E_{ANA}$ ) for these parameters is 1.17 eV. The energy resolution of the Mg  $K_\alpha$  x-ray source ( $\Delta E_S$ ) is 0.68 eV. The overall instrumental energy resolution ( $\Delta E_{INS}$ ) is expressed as follows:

$$\Delta E_{INS} = \sqrt{\Delta E_{ANA}^2 + \Delta E_S^2} \quad (7)$$

and was calculated to be 1.35 eV for the XPS survey spectra. The C 1s detail spectra were performed using a 10 eV pass energy and 0.03 eV energy steps. An entrance slit of 7 mm was used for the electron analyzer. From equation (4) of Section 2.2.2, the analyzer energy resolution ( $\Delta E_{ANA}$ ) for these parameters is 0.23 eV. In consequence, the overall instrumental energy resolution results in 0.72 eV, from equation (7). As mentioned in Section 2.1.3, to these values the core hole lifetime must be incorporated to define the natural line width of the XPS core level lines. From the obtained full-width-at-half-maximum (FWHM) of the C 1s line of the untreated sample, it is found that the core hole lifetime adds approx. 0.3 eV to the line width. As mentioned in Section 2.2.2, the XPS measurements were calibrated to the Ag 3d<sub>5/2</sub>, Au 4f<sub>7/2</sub>, and the Cu 2p<sub>3/2</sub> photoelectron lines of reference samples.

The He I UPS secondary electron cutoff spectra (to derive the work function) were obtained using a 1 eV pass energy and 0.03 eV energy steps. The He II valence band

maximum (VBM) spectra were obtained using a 10 eV pass energy and 0.02 eV energy steps. The UPS measurements were referenced to the Au Fermi Energy ( $E_F$ ) edge measured by He I and II, accordingly. A 15 V bias voltage was employed in all UPS measurements.

The presented PES spectra are normalized to the highest intensity unless otherwise stated.

#### 4.2.2 XPS Results

XPS spectra of the untreated SWNT sample demonstrate that carbon is not the only element present at the surface of the sample. Figure 4.1 shows the XPS survey scans for the original sample and after four different stages of hydrogenation treatments ( $T_w$  is given): (a) 298 K, (b) 1500 K, (c) 1800 K, and (d) 2050 K. From Section 3.3.2, it was determined that these four stages correspond to sample exposures: (a) to a molecular hydrogen beam, (b) to a predominantly molecular hydrogen beam, with  $T_w$  at the onset of atomic hydrogen generation, (c) to an atomic/molecular hydrogen beam with significant atomic hydrogen contributions, and (d) to a beam with the highest fraction of atomic hydrogen in the present hydrogenation study.

As expected, in addition to carbon, iron signals are observed, which are due to the catalyst residue. Uncovered portions of the In foil are responsible for the evident indium core level peaks. Additionally, slight traces of chlorine and sodium were detected, the presence of which are also attributed to the sample preparation process. Due to the oxidative process involved in the production of the SWNTs, surface oxygen in the form of carbonyl and alcohol groups is expected to be present in the sample [52, 53]. Furthermore, the SWNT powder was exposed to air prior to insertion into our glovebox.

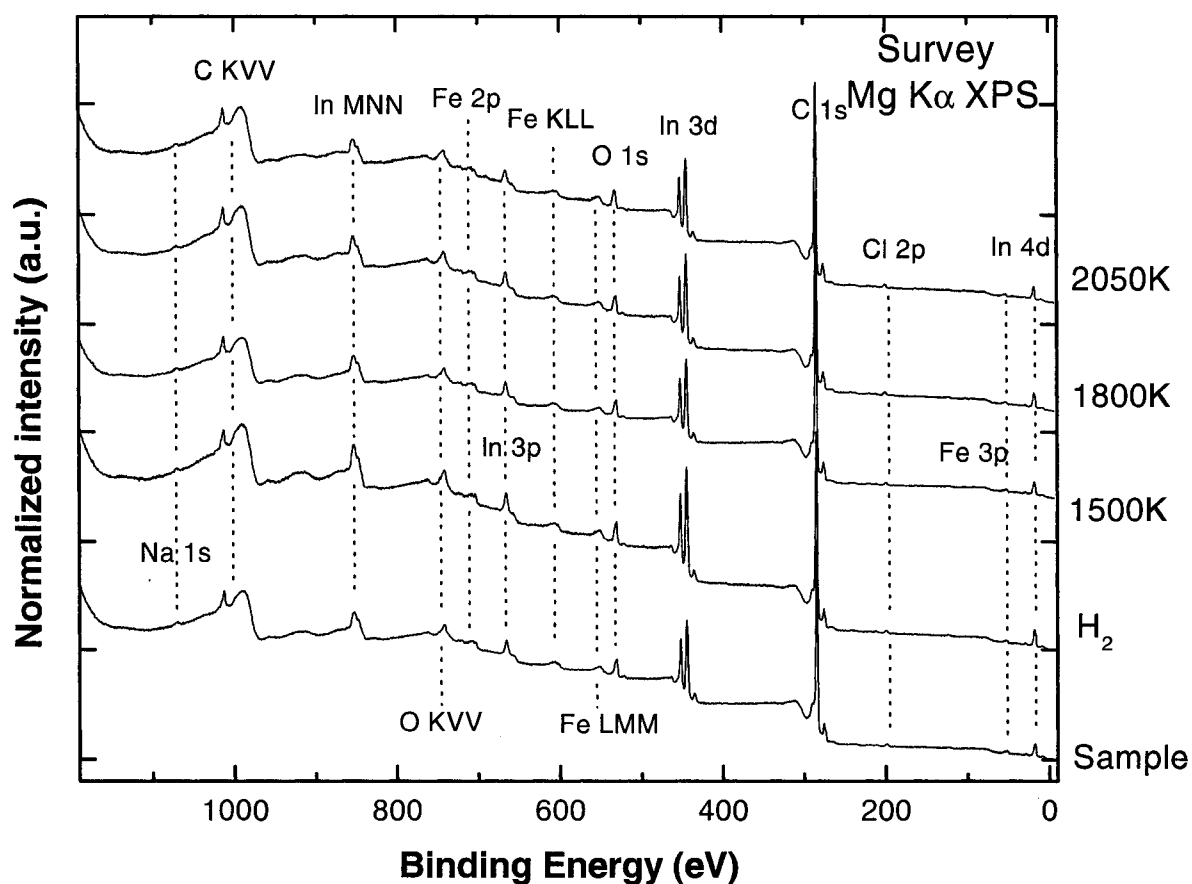


Figure 4.1 XPS survey spectra of a SWNT sample on In foil in its original state and after various  $T_w$  hydrogenation treatments.

Therefore, the survey spectra also contain an oxygen signal component, e.g., due to adsorbed water molecules. Note that hydrogen cannot be directly detected with XPS, and thus the similarity of the different survey spectra does not exclude the presence of chemisorbed hydrogen on the sample. Rather, the fact that the survey spectra indicate no significant changes as a function of  $T_w$  during the treatments indicate a relatively clean hydrogenation process, with the exception of minor fluorine deposition (at a binding

energy of approximately 690 eV, not detectable in the survey spectra) to be discussed below.

In order to investigate the scope of hydrogen chemisorption on SWNT, the XPS ability to discriminate a given element in different chemical environments must be exploited (explained in Section 2.1.3). Because the chemical bonding of atomic hydrogen

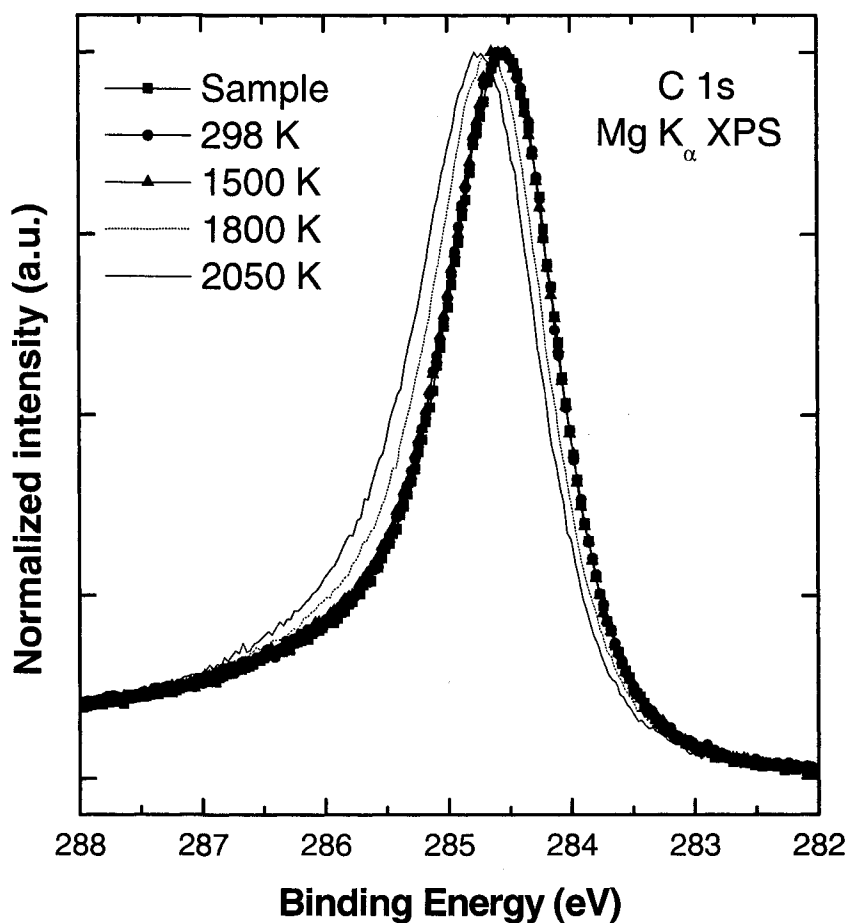


Figure 4.2 XPS C 1s detail spectra of a SWNT sample on In foil in its original state and after various hydrogenation treatments ( $T_w$  is given in the legend).



to SWNT carbon results in carbon rehybridization from an  $sp^2$ -state to an  $sp^3$ -state, a hydrogenation-induced XPS chemical shift of the C 1s core-electrons of the sample can be expected [21, 23, 24, 54].

Figure 4.2 shows detailed C 1s XPS spectra of the SWNT sample prior and after the above-mentioned hydrogenation treatment series. No chemical shift is observed after sample exposure to molecular hydrogen or lower  $T_w$  hydrogen beams, indicating an absence of hydrogen chemisorption. That molecular hydrogen exposure does not elicit a chemical change in the SWNT sample comes as no surprise since dissociation of molecular hydrogen by SWNT is energetically prohibited [27, 28]. However, it must be noted that even though the AHS characterization study showed a small production of atomic hydrogen at  $T_w=1500$  K, hydrogenation treatment at this temperature did not produce any change of the C 1s core level. Although the sample might have been exposed to some atomic hydrogen during this hydrogenation treatment, its energy may have been too low to overcome the energetic barriers for hydrogen chemisorption [23, 25, 26].

The above-mentioned shift of the C 1s peak position due to the rehybridization of the carbon atoms is observed after a hydrogenation treatment at a  $T_w$  of 1700 K and above (i.e., 1800 and 2050 K in Figure 4.2). As analyzed in detail in Figure 4.3, hydrogenation treatment at higher  $T_w$  results in a shift towards higher binding energies, following a pattern parallel to the one exhibited by the atomic hydrogen generation of the AHS, discussed in Section 3.3.2. (the presented peak positions were derived by fitting the upper half of all the detail C 1s peaks of the experimental series with a Gaussian function, which determines the position of the overall peak maximum).

Along with the observed BE shift, the C 1s peak broadens as a result of hydrogenation. Figure 4.4 presents this phenomenon by displaying the C 1s peak FWHM values as a function of  $T_w$  during hydrogenation. Again, the  $T_w$  onset for the modification of the SWNT electronic structure (here: the induced peak broadening) appears at 1700 K. The shape of the curve displays a distinctive similarity to the induced C 1s peak chemical shift as well as the analysis of the atomic hydrogen generation of the AHS in Section 3.3.2, and the origin of both, the peak shift and the broadening, will be discussed in the following.

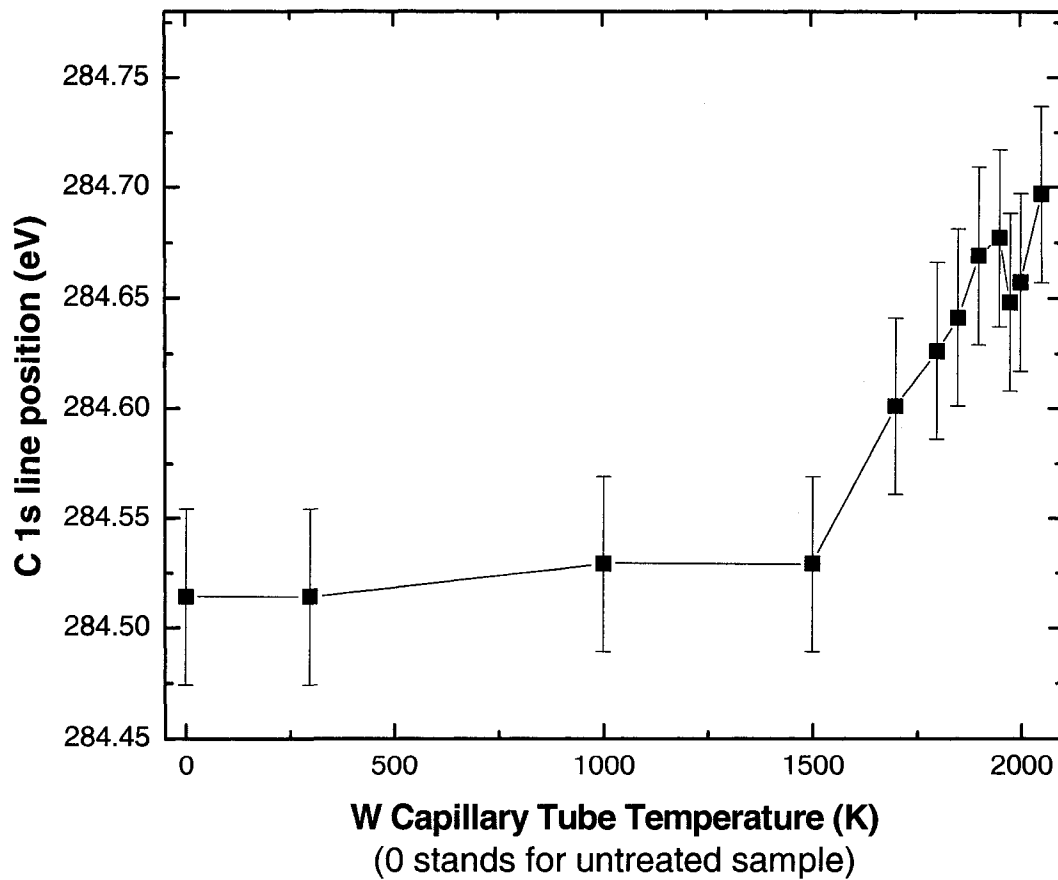


Figure 4.3 SWNT C 1s line position after hydrogenation treatments at increasing capillary tube temperature  $T_w$ .

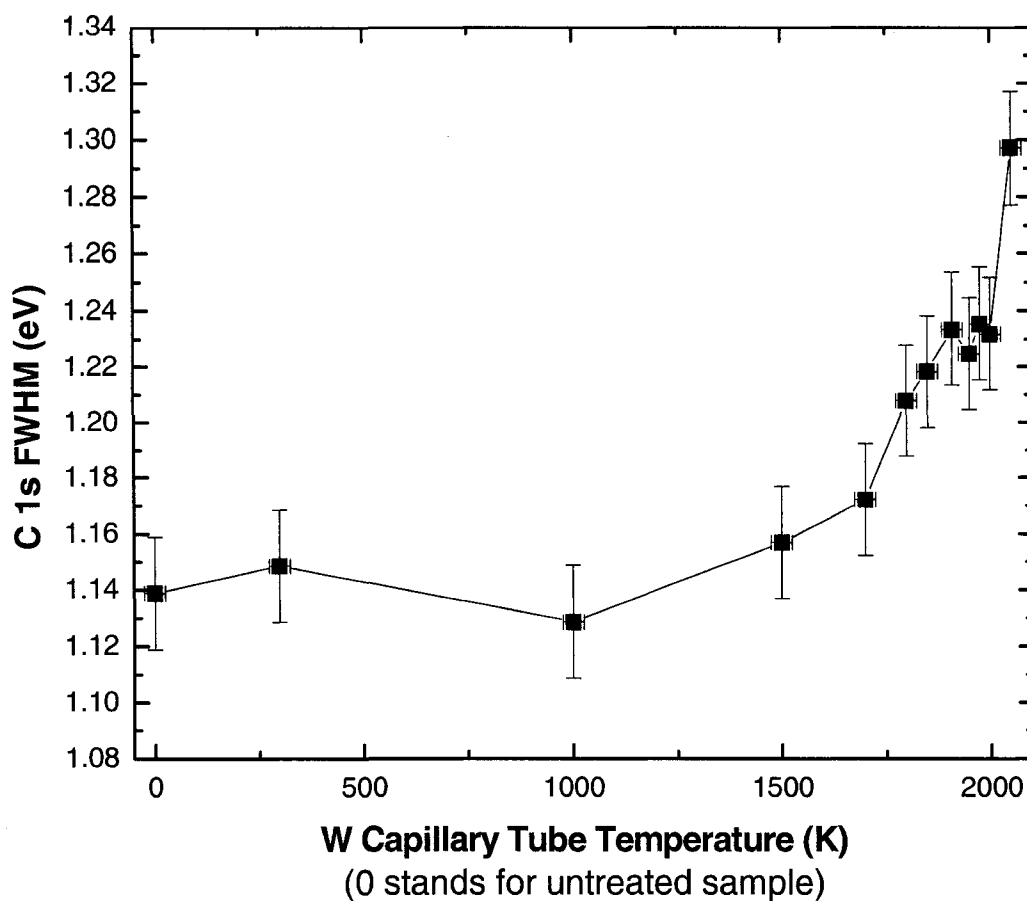


Figure 4.4 SWNT C 1s FWHM during hydrogenation treatment.

#### 4.2.3 Curve-Fit Analysis of C 1s detail XPS Spectra

Further evaluation of the detail C 1s XPS spectra yields information regarding the carbon speciation evolution of the experimental series. For this purpose, the spectra in Figure 4.2 were curve-fitted to obtain the peak components of the C 1s photoemission line. The components were fitted by using Voigt functions, which combine Lorentzian and Gaussian distributions in the peak analysis to account for core-hole lifetime and instrumental contributions, respectively. A linear background was included in the fit procedure, and all C 1s spectra of the experimental series were fitted *simultaneously*. A

reasonable agreement between fit and experimental data was found if the spectra were deconvoluted into three peaks, which are assigned to: (i) the  $sp^2$  hybridized network carbon (peak I), (ii) the  $sp^3$  hybridized carbon (peak II), and (iii) the SWNT shake-up line involving the  $\pi \rightarrow \pi^*$  transition (peak III) [24, 36, 54]. An example of a Voigt function fit with the three deconvoluted peaks is given in Figure 4.5. Each peak had its FWHM fixed for the complete fitting series; this way, the area differences for a particular peak component throughout the different stages of the series

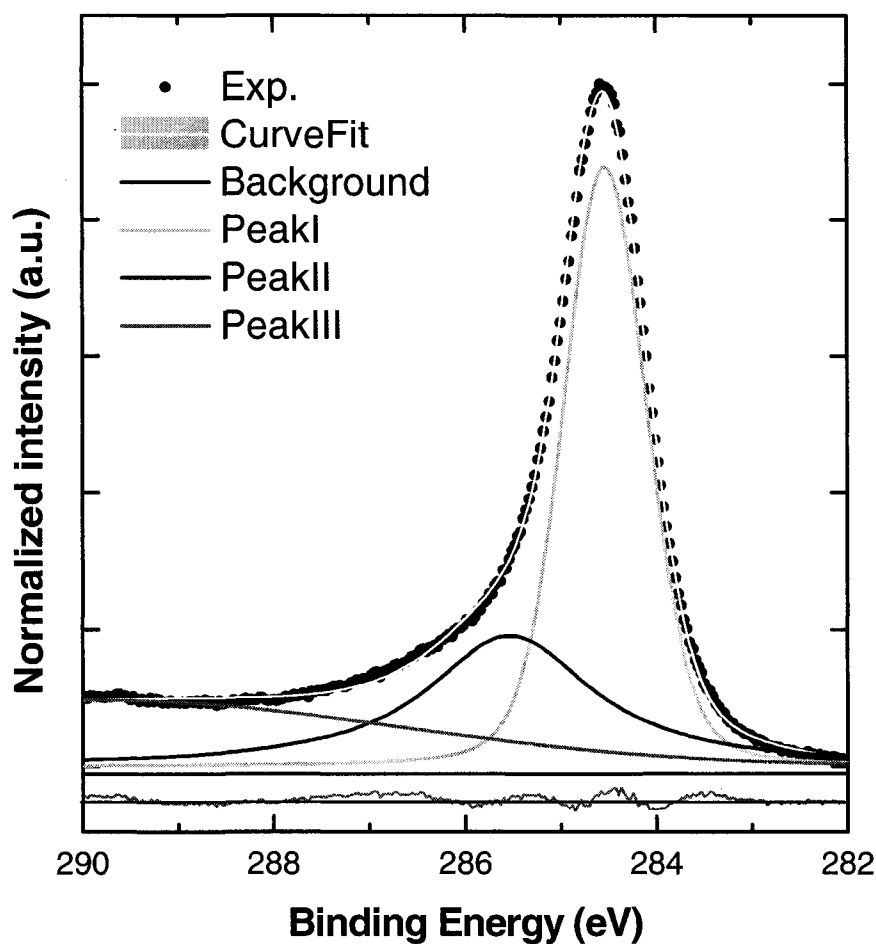


Figure 4.5 Deconvolution of the C 1s photoemission line.

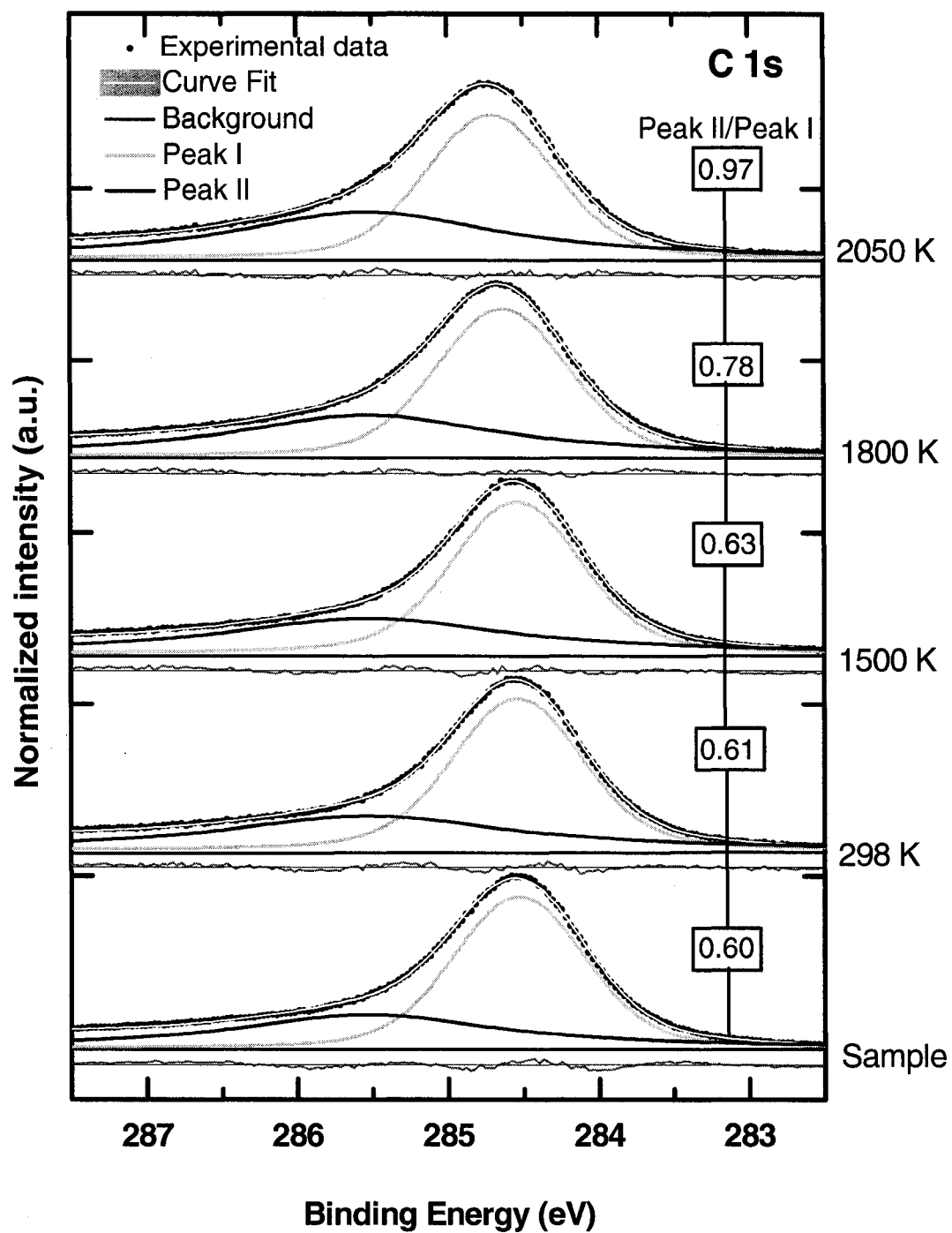


Figure 4.6 Deconvolution of the C 1s photoemission line for five different capillary temperatures  $T_w$  of the experimental hydrogenation series (the fit residual shown below the background line has been magnified by a factor of 2).

experiments can be directly attributed to changes in the intensity of the represented chemical species. Figure 4.6 provides the fitted peak I and II components of the C 1s spectra for five stages of the experimental series.

The curve-fitting evaluation of the detailed C 1s spectra demonstrates that the changes in the spectral shape of the C 1s photoemission line are caused by intensity changes in peak I and peak II. The position of the peak I and peak II components was found to be 284.6 and 285.5 eV, respectively. This 0.9 eV separation is corroborated by literature values [24, 54]. The hydrogenation treatment induces a reduction in peak I, while simultaneously augmenting peak II, as expected. The change of the ratio between the peak II area ( $A_{II}$ ) and the peak I area ( $A_I$ ) as a function of  $T_w$  during hydrogenation treatment is displayed in Figure 4.7. Again the  $A_{II}/A_I$  values for the C 1s peak components of the original sample and the sample after “low”  $T_w$  hydrogenation treatments are observed to remain relatively constant. An increase in the  $A_{II}/A_I$  ratio occurs at 1700 K  $T_w$  and continues to increase along with the capillary tube temperature. These observations are in complete agreement with the expectation of rehybridization induced by hydrogen chemisorption.

Several reasons can account for the presence of a  $sp^3$ -hybridized component (peak II) in the detail C 1s spectrum of the untreated SWNT sample. First of all, an amount of 5 %-wt. amorphous carbon was present in the SWNT powder employed during the sample preparation [50, 51]. Moreover, the XPS survey O 1s line indicates the existence of oxygen-containing functional groups binding to the carbon network of the SWNT sample. These carbon species show up at a higher BE than the network-coordinated carbon [36, 53, 55]. Consequently, to ensure that increments in peak II intensity are truly

induced by hydrogen chemisorption, the levels of the extemporaneous factors accounting for the original sample's C 1s peak II component were investigated in more detail (see below).

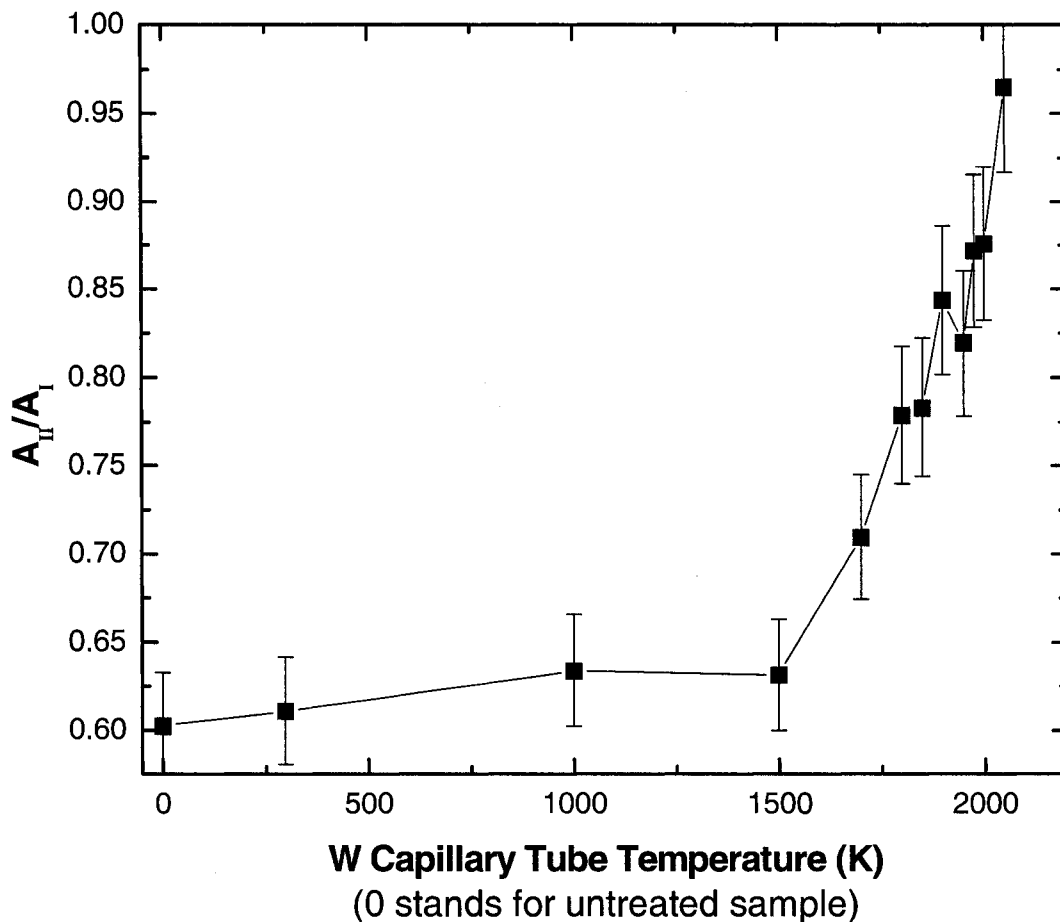


Figure 4.7 Peak II/peak I area ratio  $A_{II}/A_I$  (i.e.,  $sp^3/sp^2$  carbon hybridization ratio) of the SWNT sample as a function of  $T_w$  during hydrogenation.

Because the sample remained in an UHV environment ( $10^{-10} - 10^{-9}$  mbar) throughout the entire experimental series, it is expected that (except for an initial change which could

potentially take place right after the sample was introduced in the characterization system) the oxygen content of the sample may remain relatively unchanged. Likewise, chlorine sample levels should remain relatively unchanged since the only sample handling taking place pertains to sample transferring via the mechanical trolley transfer system, which does not involve any direct contact with the analyzed sample. To determine the relative oxygen intensity of the sample throughout the experimental series, the 523.6-543.6 eV BE range was extracted from the XPS survey spectra. The obtained “detail” spectra were normalized to the background (at 527.6 eV BE). The area of the O 1s photoemission line was fitted using a linear background and two Voigt peaks, one for alcohol groups and one for carbonyl groups. The total area of the O 1s XPS peaks is the sum of the component peak areas. Likewise, the Cl 2p relative intensity was obtained following the same guidelines. The 190.1-210.1 eV BE range was extracted from the XPS surveys. The intensity at 192.6 eV BE was used for background normalization. One Voigt peak was used for the curve fitting analysis. Because these fittings were performed from the mentioned survey spectra portions, the energy resolution as well as the signal-to-noise ratio was poorer than if detail spectra had been collected. A larger error bar in the derived values is thus expected than that obtained from dedicated detail spectra.

Figure 4.8 presents the behavior of the oxygen and chlorine intensities after the different hydrogenation temperatures of the experimental series ( $A_T$ ) in comparison to the original intensity ( $A_0$ ). As expected, the surface population of these elements remains relatively unchanged in comparison to the original sample. A slight spike in the oxygen



and chlorine levels seems to occur at 1950 K and 1975 K  $T_w$  hydrogenation levels. However, the rise does not continue at higher  $T_w$  and is well within the error bars.

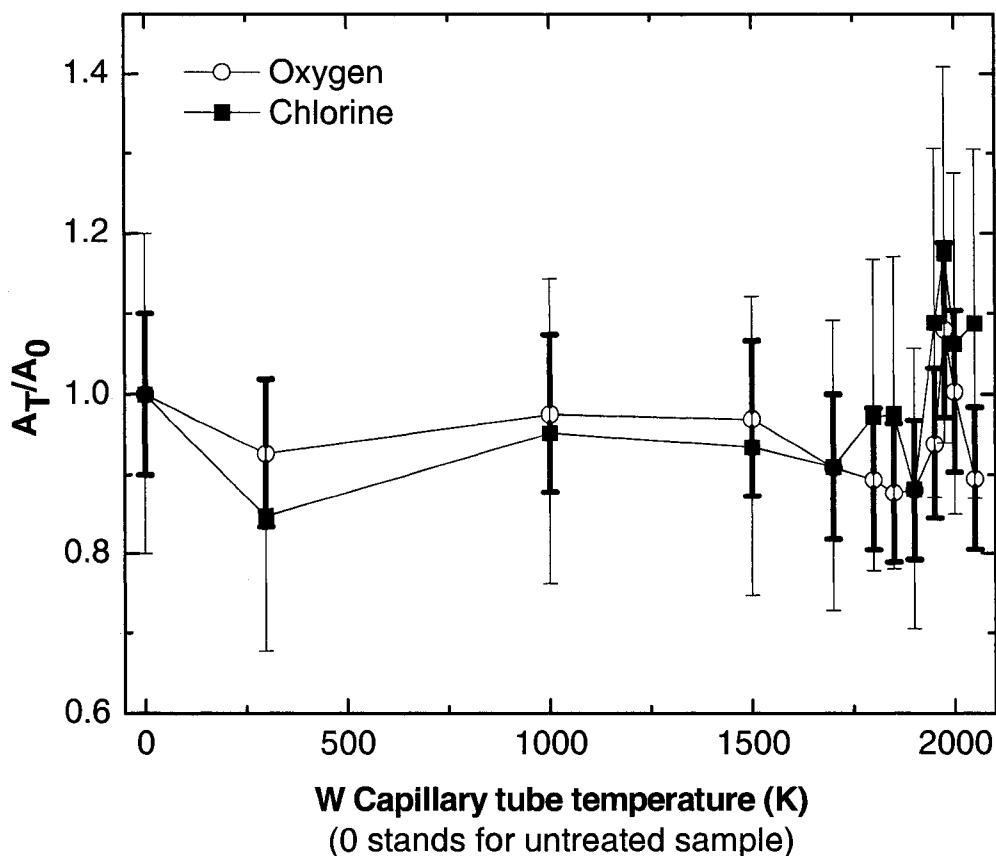


Figure 4.8 Oxygen and chlorine surface levels along the course of the experimental series relative to the original level in the untreated sample.

This constant surface coverage was not observed in the case of fluorine. Although initially undetected in the XPS spectra of the untreated and low  $T_w$  hydrogenation treated SWNT sample, a fluorine signal appears after the 1850 K  $T_w$  hydrogenation step, indicating fluorine deposition on the sample (see Figure 4.9a). The source of the F

contamination was found to be a vacuum gate valve with a Viton® sealing lip. Electrons escaping from the AHS and impinging on the fluoropolymer elastomer material, as well as the increased temperature of the AHS surrounding during hydrogenation are likely responsible for the fluorine liberation. After removal of the vacuum gate valve after this experimental series, the presence of fluorine in samples was no longer detected.

The F 1s peak intensities for the different  $T_w$ -dependent spectra were analyzed to compare their surface content. For this purpose, the 680-700 eV BE range was extracted from the hydrogenation treatment XPS survey spectra. The derived “detail” spectra were normalized to background (at 527.6 eV BE) and are shown in Figure 4.9a. The area of the F 1s photoemission line was fitted using a linear function background and a Voigt peak. The fitted peak area obtained for all the hydrogenation treatment spectra ( $A_T$ ) were normalized to the background area of the untreated sample ( $A_0$ ). Figure 4.9b presents the results of this analysis. The solid line in the figure demarcates the  $T_w$  whereupon formation of atomic hydrogen by the AHS becomes significantly pronounced. The dotted line indicates the approximate onset of F deposition on the sample.

The presence of fluorine on the hydrogenated samples is a great concern due to fluorine’s large electronegativity. Thus, a fluorine surface contamination could result in significant modifications of the electronic structure of the treated samples. This could potentially influence the changes induced by hydrogen chemisorption. However, it can be determined by the intensity of the F 1s peak in the XPS survey spectra of the affected samples that the fluorine “contamination” is only very small, and thus it is highly improbable that deposition of fluorine on the sample may have caused the observed chemical changes in SWNT carbon.

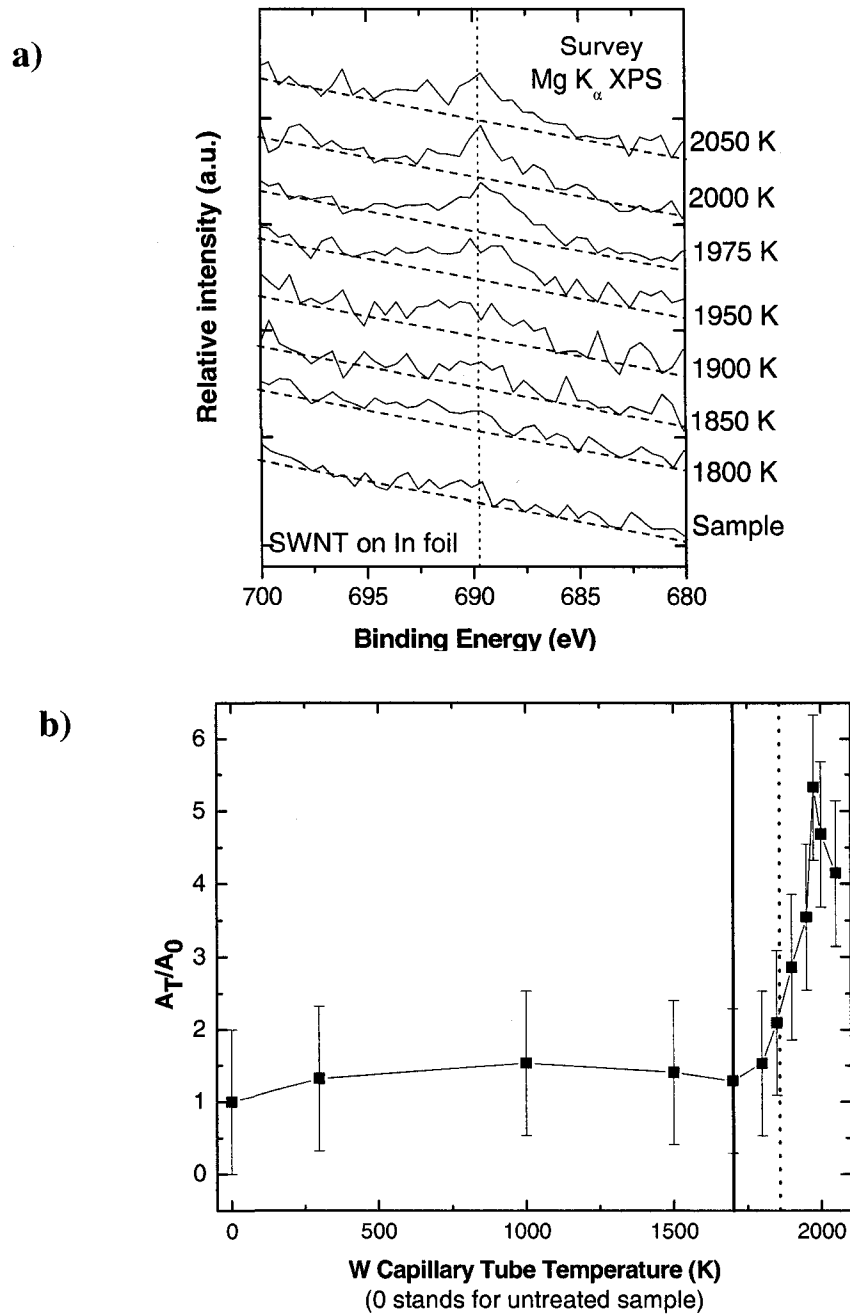


Figure 4.9 Analysis of fluorine contamination on the SWNT sample: (a) F 1s spectral region extracted from the XPS survey spectra as a function of  $T_w$ ; (b) comparison of F 1s fitted intensity relative to the untreated sample. The solid line indicates the  $T_w$  onset for the hydrogen-induced C 1s core level changes, and the dotted line the probable  $T_w$  onset for fluorine deposition.

Although Figure 4.9b shows that the intensity of the F 1s photoemission is increasing with increasing  $T_w$ , the temperature at which fluorine is first detected (i.e.,  $T_w = 1850$  K) is above the onset temperature at which the first C 1s peak shift is observed (i.e.  $T_w = 1700$  K). Furthermore, one would expect the fluorine-bonded carbon contribution to the C 1s line at positions higher than 288 eV BE [36, 56], which is at least 2.5 eV above the  $sp^3$  hybridized carbon peak that increases upon hydrogenation. No evidence for such additional intensity is observed in our C 1s XPS detail spectra.

Nevertheless, effects of fluorine contamination should not be treated lightly, in particular for the characterization of VB structures and work function values. This will be discussed in conjunction with the UPS results discussed in the next section.

#### 4.2.4 UPS Results

UPS characterization sheds light on the VB structure and its potential changes as a result of hydrogenation treatments. As previously addressed in Section 2.1.4, two electron groups of interest can be investigated using this spectroscopic technique: (i) electrons photo-emitted from the uppermost atomic layers of the sample, which suffer no energy loss related to inelastic collisions; and (ii) secondary electrons that have gained enough energy to escape from the solid to the vacuum level. Evaluation of the former electron group allows for the determination of the outer VB density-of-states (DOS) electron distribution. Evaluation of the latter group yields the work function of the sample.

Figure 4.10 shows the He II UPS valence band spectra of the SWNT sample at five different stages of the experimental series. Three significant feature changes in the valence band are induced by the hydrogenation treatment: (i) an intensity reduction of the

DOS in the 3 eV BE range, (ii) a broadening of the VBM 10 eV BE shoulder, and (iii) a shift of the 3 eV BE DOS to higher BE.

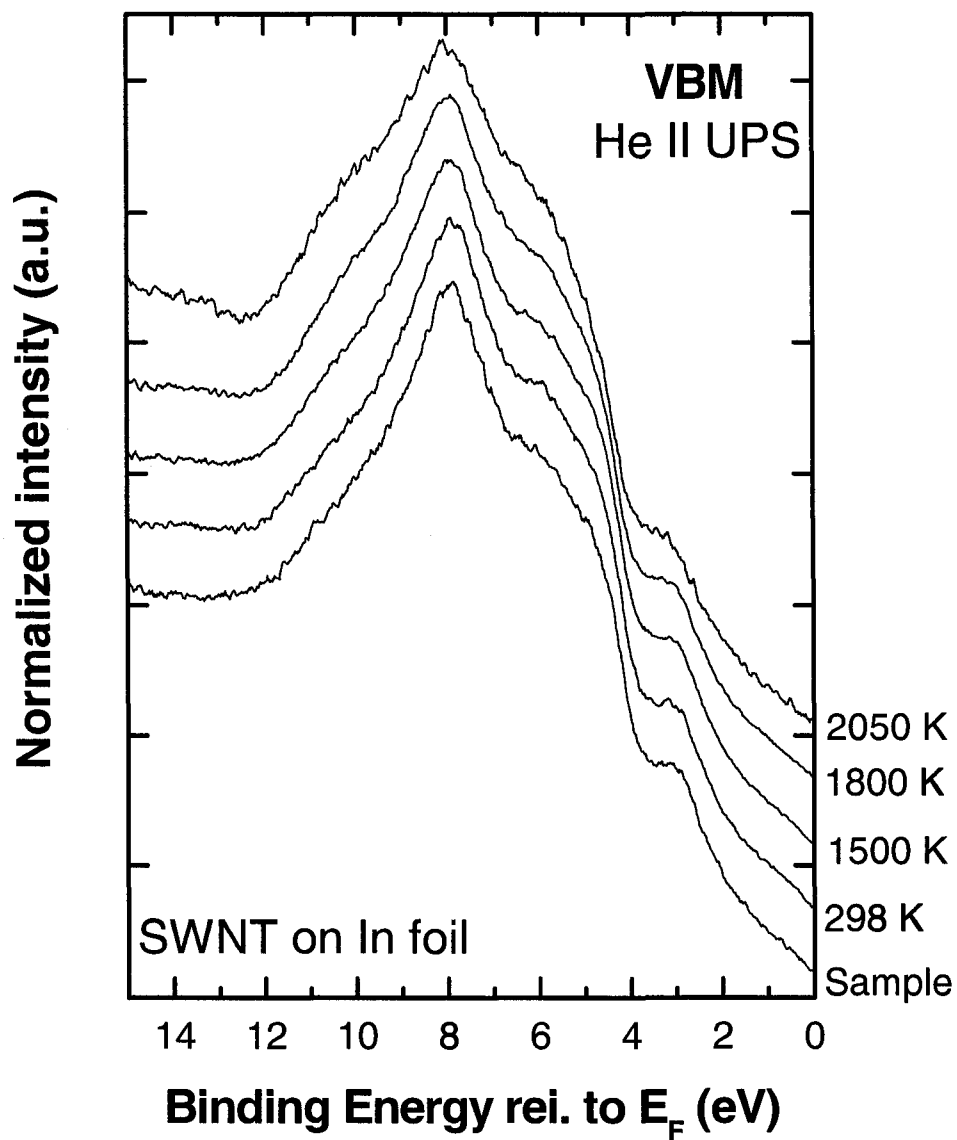


Figure 4.10 He II UPS spectra of a SWNT sample on In foil in its original state and after various  $T_w$  hydrogenation treatments, normalized to the area below the presented data.

The 3 eV BE peak is a pure  $\pi$ -state peak and thus indicates the  $\pi$ -conjugation character of the  $sp^2$ -hybridized carbon network of the SWNT [23, 57]. To quantify the peak reduction as a function of hydrogenation, sixth-order polynomial backgrounds were fitted to extrapolate the shoulder at 3.9 eV BE to the baseline observed at lower binding energy with respect to the  $\pi$ -state peak. Subtracting this background produced the peaks shown in Figure 4.11a, which were then fitted using a Voigt function to obtain their respective areas. The area of the  $\pi$ -state peaks measured throughout the various stages of the experimental series ( $A_T$ ), compared to the  $\pi$ -state peak area of the original sample ( $A_0$ ), is illustrated in Figure 4.11b. A considerable peak reduction is observed after the 1700 K  $T_w$  hydrogenation treatment stage. After the last stage of the experimental series, the peak intensity was 63% that of the untreated sample. The intensity values for the 1950 K and 1975 K  $T_w$  hydrogenation are higher than the one for 1700 K; from Figures 4.8 and 4.9, it was noticed that the spectral intensity of oxygen, chlorine and fluorine are the highest at these  $T_w$  treatments. Since UPS is an extremely surface-sensitive technique, the observed increment of surface contamination may be accountable for this deviation from the trend.

The 8-10 eV BE range is a mixed  $\sigma$ - $\pi$  state [23, 57]. The broadening of this region suggests  $\sigma$ -bond formation. Although the 10 eV BE shoulder was not quantified as a function of  $T_w$  hydrogenation treatment, Figure 4.10 qualitatively shows the shoulder broadening to follow a pattern along with  $T_w$ , with the 1800 K spectrum already exhibiting a substantial deviation from the previous stages. Thus, both feature changes (i) and (ii), signal a  $sp^2$  to  $sp^3$  hybridization transition induced by atomic hydrogen bonding to SWNT.

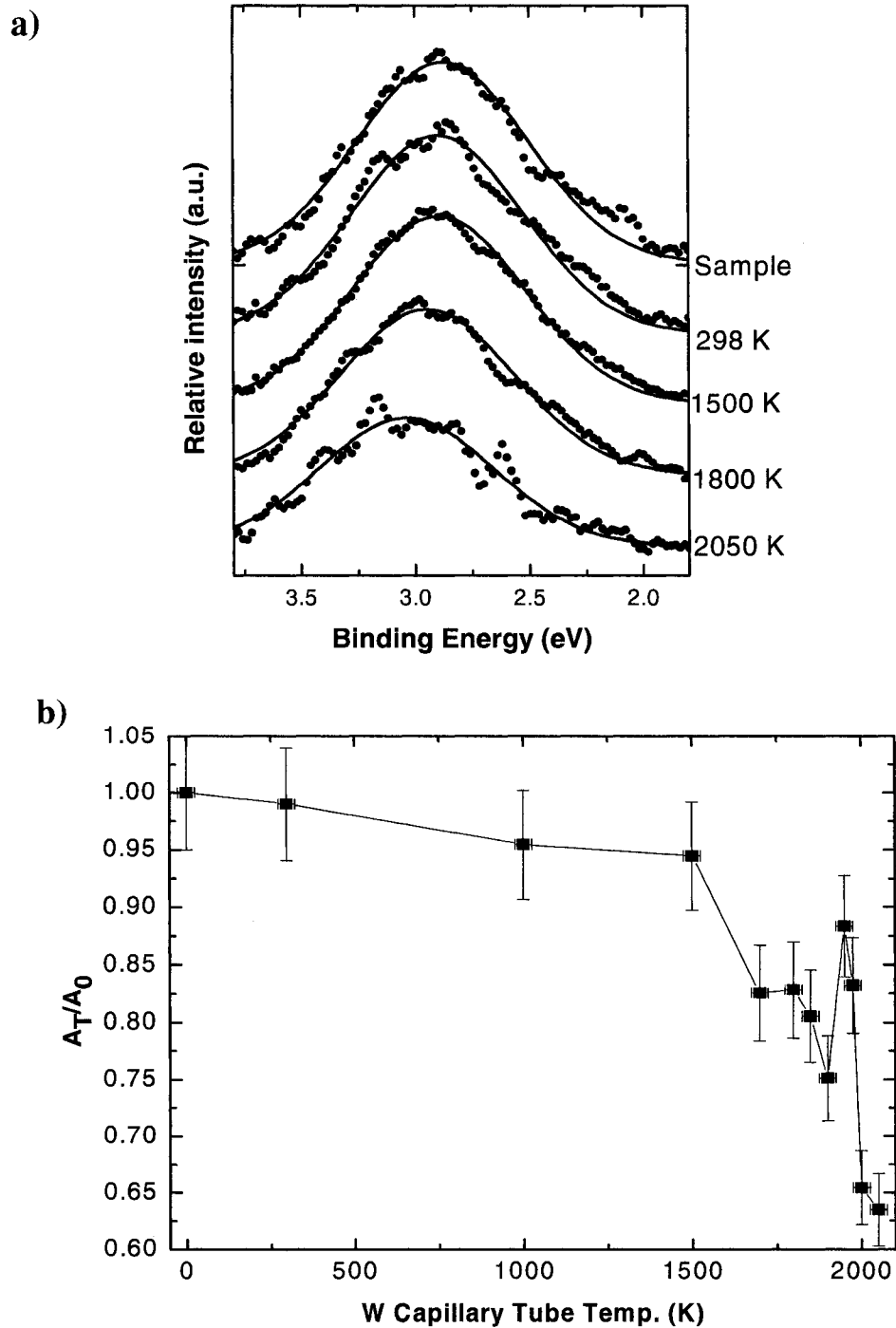


Figure 4.11 Hydrogenation-induced reduction of the SWNT  $\pi$ -electron conjugation system: (a)  $\pi$ -state peaks from the VBM spectra shown in Figure 4.10 after background subtraction; (b) comparison of  $\pi$ -state intensities relative to the untreated sample.

From examination of Figure 4.11a, a positional shift of the pure  $\pi$ -state peak towards higher BE energy is noticed as a function of hydrogenation treatment. The maximum shift ( $0.18 \pm 0.04$  eV) was observed after the 2000 K  $T_w$  hydrogenation treatment, as shown in Table 4.1. Several works have reported the possibility of modulating the band gap energy of SWNTs, and consequently their electronic properties, as a function of hydrogen coverage [26, 58-60]. The observed  $\pi$ -state peak shift would be in agreement with a larger energy band gap for the hydrogenated SWNT sample. Nonetheless, the present findings concerning this subject are still inconclusive. Since UPS only characterizes the position of valence band maximum (VBM) with respect to the  $E_F$ , inverse photoelectron spectroscopy would still be required for the same experimental series in order to determine the conduction band minimum, resulting in a direct access to the electronic surface band gap energy. Moreover, the most pronounced positional shift was observed after the 1900 K  $T_w$  hydrogenation treatment.

<b>Tw</b>	0	298	1000	1500	1700	1800	1850
<b>position</b>	2.88 $\pm$ 0.02	2.9 $\pm$ 0.02	2.9 $\pm$ 0.02	2.9 $\pm$ 0.02	2.92 $\pm$ 0.02	2.95 $\pm$ 0.02	2.95 $\pm$ 0.02
<b>shift</b>	0	0.02 $\pm$ 0.04	0.02 $\pm$ 0.04	0.02 $\pm$ 0.04	0.04 $\pm$ 0.04	0.07 $\pm$ 0.04	0.07 $\pm$ 0.04

<b>Tw</b>	1900	1950	1975	2000	2050
<b>position</b>	3.03 $\pm$ 0.02	3.01 $\pm$ 0.02	3.03 $\pm$ 0.02	3.06 $\pm$ 0.02	3.01 $\pm$ 0.02
<b>shift</b>	0.15 $\pm$ 0.04	0.13 $\pm$ 0.04	0.15 $\pm$ 0.04	0.18 $\pm$ 0.04	0.13 $\pm$ 0.04

Table 4.1  $\pi$ -state peak position and shift induced by hydrogenation treatment. (The  $\pi$ -state peak position and shift are given in eV, the  $T_w$  in K. The 1000 K  $T_w$  hydrogenation treatment values were omitted due to table space constraints).



Since fluorine deposition on the sample begins around this experimental series stage it is unclear whether the  $\pi$ -state shift is attributable to hydrogen chemisorption, fluorine deposition, or a combination of both. Further experimentation is planned to resolve this issue.

Hydrogenation treatment also led to a reduction in the sample work function ( $\Phi$ ), which is the minimum energy required to remove an electron from the  $E_F$  to the vacuum level near the surface of the sample. Figure 4.12a shows the secondary electron cut-off of the UPS spectra after various stages of the experimental series. Subtracting the respective cut-off values from the excitation energy source (i.e., He I = 21.22 eV) yields the  $\Phi$  value. In Figure 4.12b, the measured  $\Phi$  values are shown as a function of  $T_w$  hydrogenation.

A clear change in the  $\Phi$  value first becomes apparent after 1700 K  $T_w$  hydrogenation treatment. The  $\Phi$  value continues to decline with subsequent higher  $T_w$  hydrogenation treatments. After the last stage, the obtained  $\Phi$  value was 0.5 eV lower than the one for the untreated sample. Because carbon has greater electronegativity than hydrogen, C-H covalent bonds possess an inherent dipole charge. A positive surface charge is created as a result of SWNT hydrogenation, which modifies the dipole existing at the surface of the pristine SWNT sample. Since this induced charge formation facilitates the ejection of electrons from the sample, the  $\Phi$  value is decreased [23, 61]. Since fluorine has the highest electronegativity properties of all the elements, sole deposition of fluorine on a SWNT would have the opposite effect of hydrogen chemisorptions, which is not observed in our data. In contrast, the observed fluorine contamination apparently does not prevent the  $\Phi$  value reduction induced by the hydrogenation of the SWNT sample.

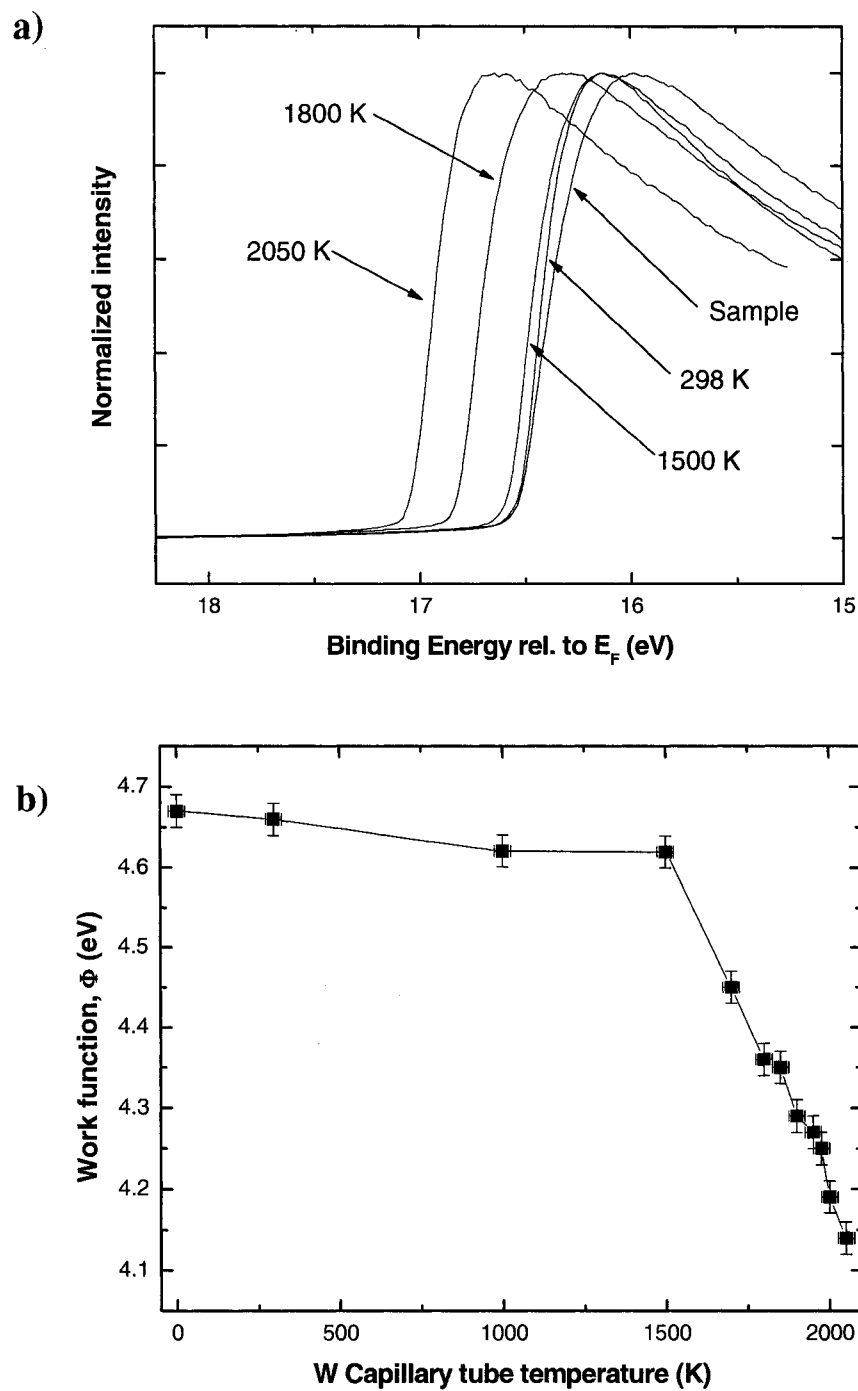


Figure 4.12 Hydrogenation-induced work function reduction: (a) He I UPS cut-off spectra for SWNT sample on In foil in its original state and after various  $T_w$  hydrogenation treatments; (b) work function as a function of  $T_w$  hydrogenation.

In summary, this experimental series has shown the transformation of chemical and electronic states of a SWNT sample as a result of hydrogenation treatment. All characterized features show a similar transformation pattern along with  $T_w$ . A significant change of the chemical and electronic structure of the sample can be observed at AHS capillary temperatures for which atomic hydrogen is produced, in particular a transition from  $sp^2$ -bonded carbon to  $sp^3$ -bonded carbon environments. Fluorine contamination was observed, but occurred only at higher hydrogenation temperature treatments. Thus, the presented results from this experimental series might contain a greater margin of error, but, nonetheless, it is safe to claim that the observed changes were induced by hydrogen chemisorption of the SWNT sample because the F-contamination and hydrogenation was found to start at different capillary temperatures. Appendix I summarizes the results of this experimental series.

### 4.3 Hydrogen Adsorption/Desorption Cycle Study

#### 4.3.1 Introduction

The reversibility of the change of electronic structure induced by hydrogen chemisorption observed in the experimental series described in Section 4.2 is tested in this study. Hydrogen desorption is attained by annealing a hydrogenated SWNT sample.

Additionally, two unresolved issues from the previous experimental series are considered in this new study: (a) the spurious effect of fluorine and other surface contaminants and (b) the effect of hydrogenation time exposure on the degree of hydrogenation experienced by the sample. To minimize the first concern, the prepared SWNT sample was heat-treated to desorb surface contaminants, and exposed to a 1750 K

$T_w$  hydrogenation treatment (i.e., below the “fluorine contamination onset”) to prevent fluorine deposition on the sample. Regarding the second matter, the sample was hydrogenated for two different durations. The first period lasted 15 minutes, comparable to the entire (summed) atomic hydrogenation exposure time during the experimental series in Section 4.2. The second period lasted 30 minutes.

#### 4.3.2 Experimental Procedure

For this experimental series, the sample was prepared by depositing several drops of a SWNT dispersion in dimethylformamide (DMF) onto tantalum foil. The SWNT powder used to prepare the dispersion was the same as the one mentioned in Section 4.2.1. After application of the dispersion, the sample was submitted to vacuum for 10 minutes in order to evaporate the solvent. Afterwards, the sample was stored overnight in UHV. The resulting sample possessed greater substrate coverage with better layer uniformity in comparison to the “pressing in In foil” method. Furthermore, the Ta sample support allowed for heating of the sample. Heat-treatment is greatly advantageous with respect to removing surface contamination, such as adsorbed water molecules. Desorption of chemisorbed hydrogen can also be achieved; thus, the results of further hydrogenation cycles can be assessed. The Ta support was secured to a molybdenum (Mo) sample plate by the use of Mo screws. The sample plate was slid into a sample holder on the manipulator of the SCIENTA system on which sample heating could be carried out in UHV in the preparation chamber of the SCIENTA system. The introduced SWNT sample was annealed for several hours at a temperature of 1050 K. The annealing of the hydrogenated sample (for hydrogen desorption) was carried out for three hours at a temperature of 980 K. During this experimental series, the AHS was also installed in the

SCIENTA preparation chamber, and hydrogenation treatment took place therein. Due to the dimensions and design of the Mo sample plates for the SCIENTA system, a stainless steel carrier was constructed in order to allow sample transferring via the trolley mechanism to the Andere ESCA system, where all the measurements of this experimental series were performed. In order to prevent fluorine contamination on the sample, as observed in the  $T_w$ -dependence series in Section 4.2, the hydrogenation treatment was limited to  $T_w$  values of 1750 K, as mentioned above. Moreover, longer hydrogenation time periods were tested to investigate how the chemical and electronic structure changes as a function of hydrogenation time.

The experimental series consisted of five phases: (i) the original sample, (ii) the heat-treated sample, (iii) the hydrogenated sample, (iv) the annealed sample, and (v) the rehydrogenated sample. Sample analysis was carried out in the same manner as explained in Section 4.2.1. Detailed XPS measurements for O 1s and F 1s were included in this experimental series, using a 10 eV pass energy and a 0.03 eV energy step setting in both cases.

#### 4.3.3 XPS Results

Once again, the XPS surveys showed iron, oxygen, chlorine, and sodium to be present at the sample surface, as demonstrated by Figure 4.13. A Mo signal was detected attributable to the screws securing the sample and to the large spot of the impinging X-ray shining onto the Mo sample plate. Remarkably, the most intense Ta photoelectron lines, the ones for the 4f core electrons, do not even surface in the survey spectra of this experimental series. This lack of a significant Ta fingerprint in the survey spectra indicates the effectiveness of the here-employed sample preparation technique.

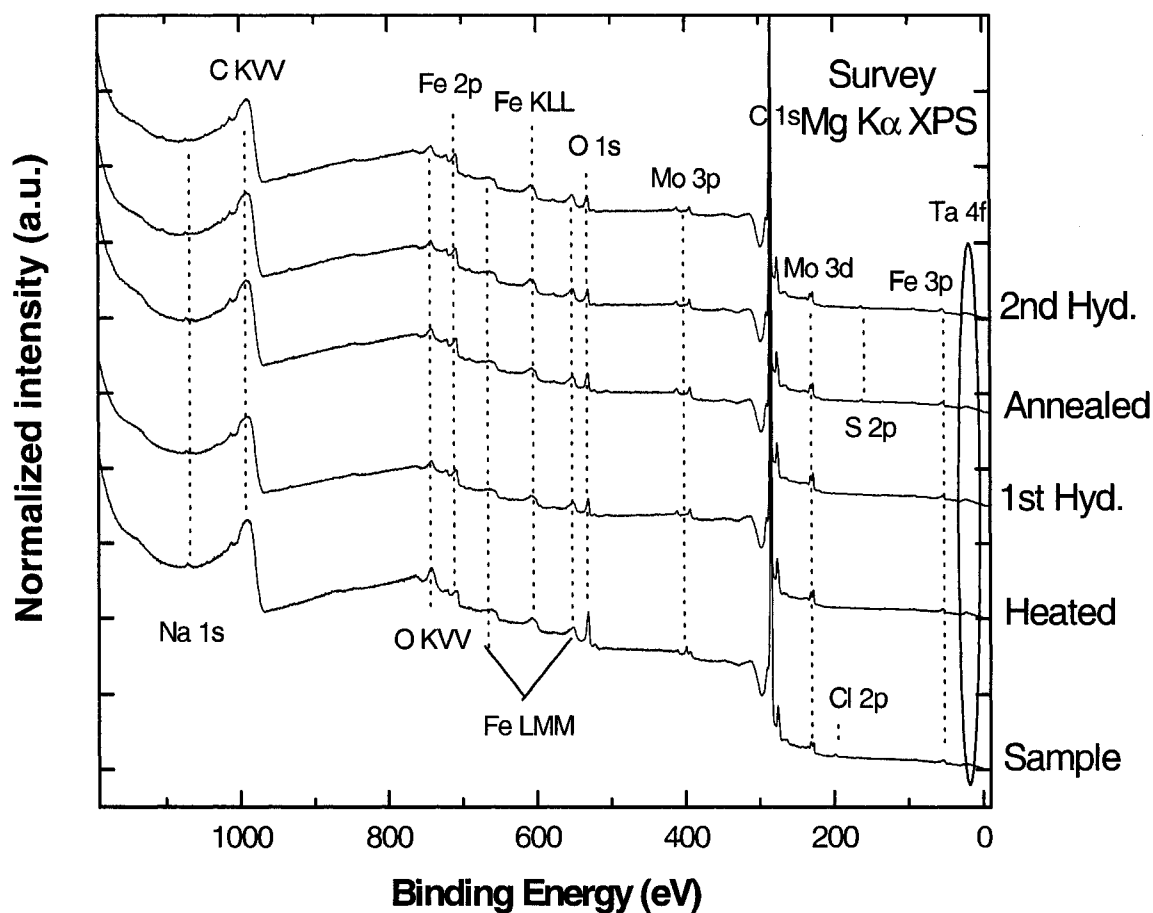


Figure 4.13 XPS survey of SWNT sample on Ta foil throughout the five phases of the experimental series (the oval points out the BE-position for Ta 4f photoelectron lines).

After heating the sample to temperatures greater than 1050 K for several hours, a considerable reduction in surface oxygen and sodium content was achieved. Furthermore, no traces of chlorine were detectable in the survey spectrum of the heated sample. Figure 4.14 shows the detailed O 1s spectra throughout the course of the experimental series. Fit analysis of the O 1s detailed spectra reveals that heat treatment caused the oxygen content

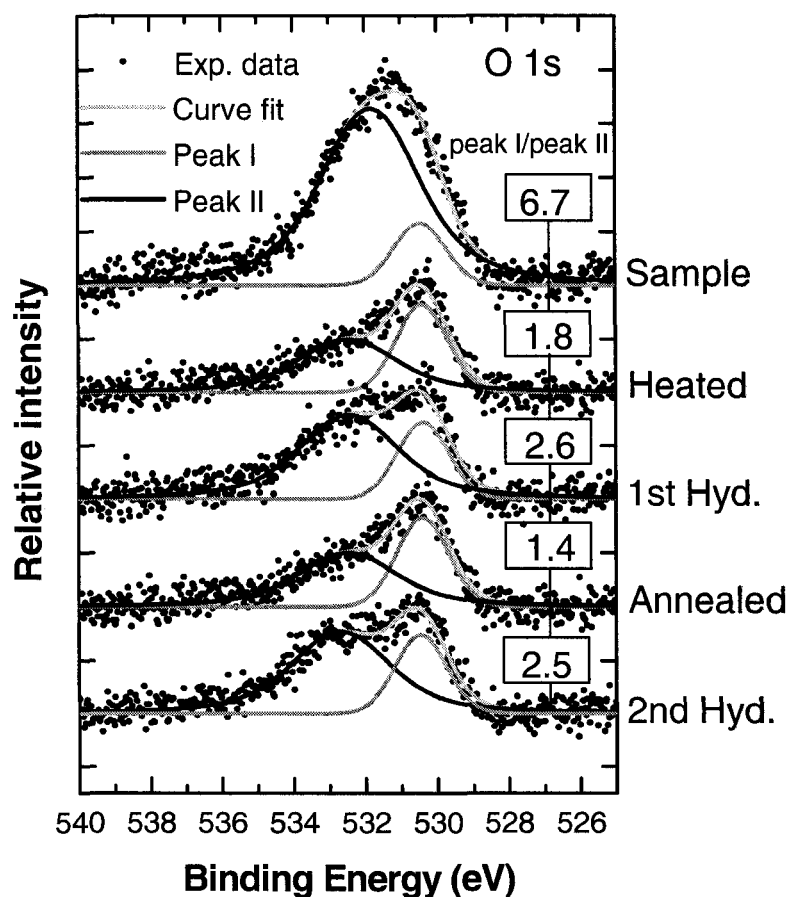


Figure 4.14 Oxygen speciation during the course of the experimental series, linear background omitted. Peak I, roughly representing double-bonded oxygen, is observed at 530.4 eV, peak II, roughly representing single-bonded oxygen, is found at 532.5 eV.

in the sample surface to drop to approximately half the untreated content. However, oxygen desorption overwhelmingly proceeds from the oxygen forming single covalent bonds to surface carbon, shown as the 532.5 eV peak II in Figure 4.14. The intensity of peak I at 530.4 eV, representing double-bonded oxygen, actually increases as a result of the heat treatment. Upon hydrogenation, one can observe a reduction in the peak I intensity and at the same time a growth in the intensity of peak II. This suggests that

atomic hydrogen reacts with the remaining carbonyl oxygen, reducing it to hydroxyl groups.

Concerning fluorine deposition as a result of the hydrogenation process, Figure 4.15 shows that a small fluorine signal was originally present in the untreated SWNT sample, but that it did not perceptibly change in the following stages of the experimental series, in particular not during the hydrogenation stages.

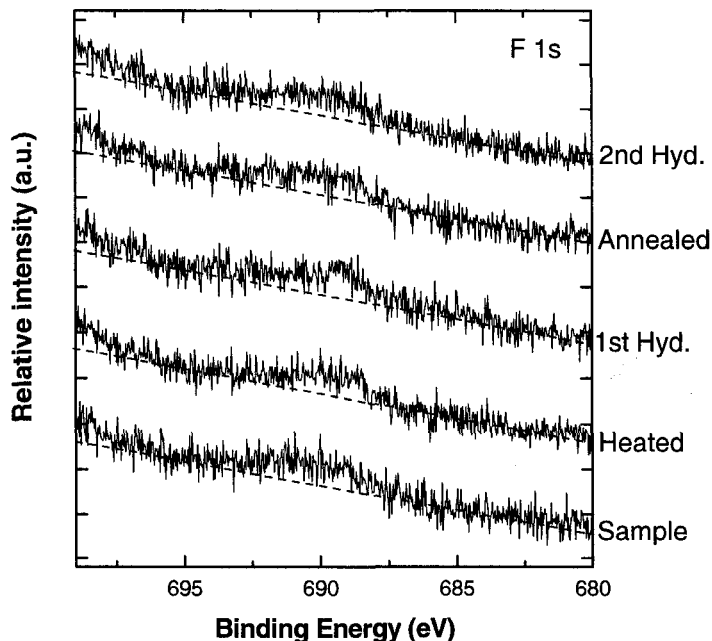


Figure 4.15 F 1s detail spectra of the SWNT sample during the five phases of the experimental series.

To better appreciate the carbon chemical shifts obtained in this series, the five detailed C 1s spectra are shown in two steps in Figure 4.16. The lower set of spectra shows the experimental stages up to the first hydrogenation phase. The upper set of spectra displays



the C 1s photoemission line after annealing the hydrogenated sample and re-hydrogenation. The C 1s chemical shift to higher BE values observed in Section 4.2.2 was reproduced as a result of the hydrogenation treatment, indicating  $sp^3$  hybridized carbon formation due to hydrogen chemisorption. Moreover, this chemical shift was reversed after the annealing stage, as can be seen in the detailed position analysis in Figure 4.17.

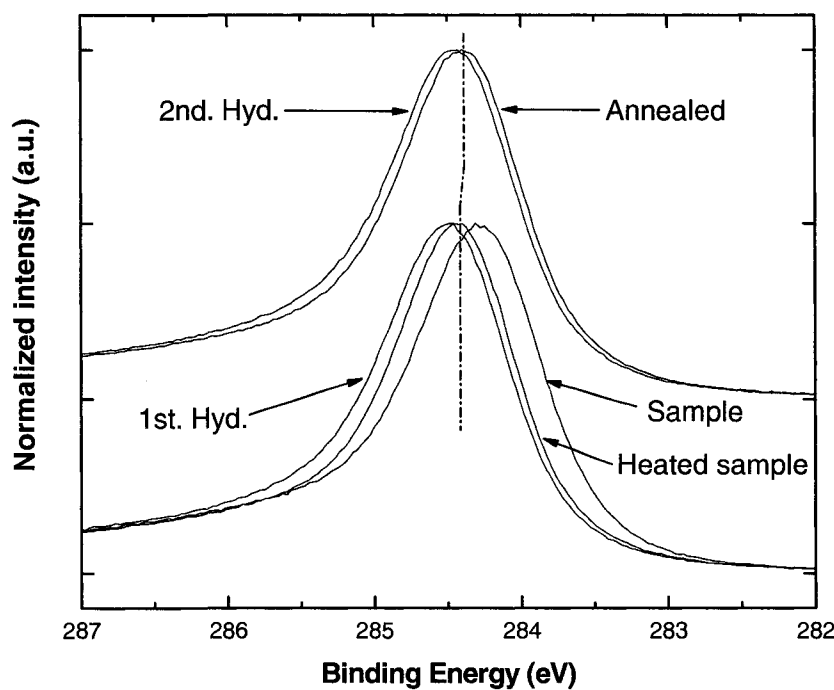


Figure 4.16 XPS C 1s detailed spectra of SWNT on Ta foil at various experimental stages (lines drawn through the heated and annealed samples are there to ease comparison of peak positions).

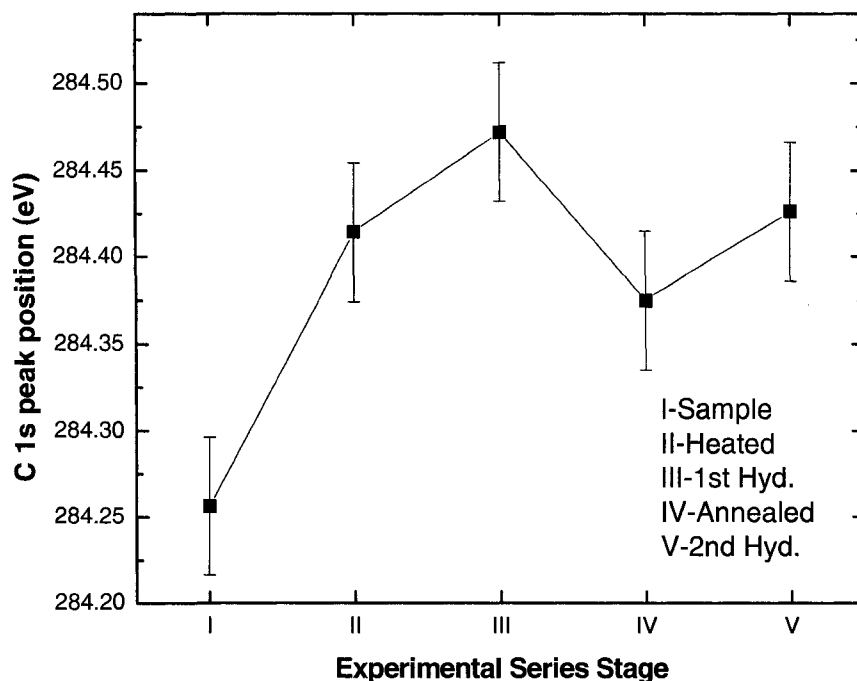


Figure 4.17 SWNT C 1s line position throughout experimental series stages.

As in the previous experimental series, the chemical shifts observed in Figures 4.16 and 4.17 are accompanied by a modulation of the peak width. The calculated FWHM values throughout the experimental series are displayed in Figure 4.18. It can be noticed that the FWHM value for the untreated sample in the present experimental series is in close agreement with the FWHM value for the sample in the  $T_w$ -dependent series, i.e.,  $1.11 \pm 0.02$  eV vs.  $1.14 \pm 0.02$  eV. A drop in the C 1s FWHM value of the SWNT sample is observed after heat treatment. Since the intensity of the oxygen photoelectron lines decreased in the survey and O 1s detail spectra of the heat-treated sample, the FWHM reduction might be associated with a better-defined chemical environment of the C atoms due to oxygen desorption.

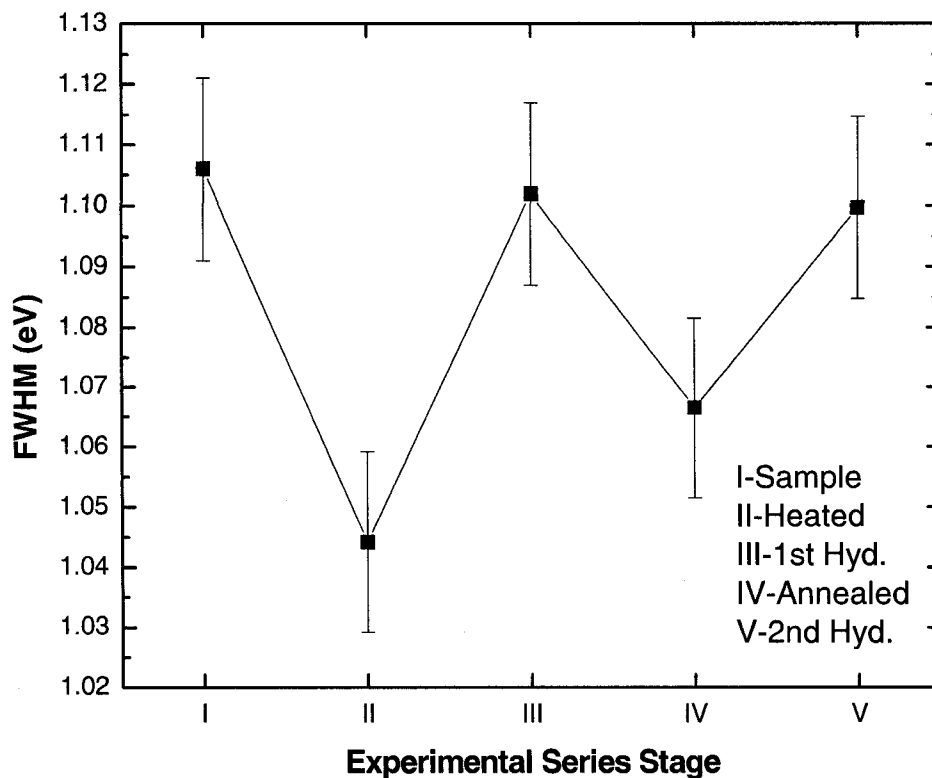


Figure 4.18 FWHM properties of the C 1s state line of the SWNT sample throughout the experimental series stages.

The 15-minute hydrogenation treatment at 1750 K  $T_w$  produced a change in FWHM nearly twice the one evoked by the 2-minute 1700 K  $T_w$  hydrogenation treatment in the first series, but not as high as the  $\Delta$ FWHM obtained by the 2-minute 1800 K  $T_w$  hydrogenation treatment (see Section 4.2.3). The FWHM was reduced by annealing the hydrogenated sample, suggesting hydrogen desorption. Nonetheless, the resulting FWHM was larger than the value for the heat-treated sample. The second hydrogenation treatment results in a similar FWHM value compared to the one attained for the first hydrogenation. Since the exposure time for the second hydrogenation treatment is twice

as long as the first hydrogenation, a lack of further C 1s width increase suggests that the level of hydrogen coverage possible for the 1750 K hydrogenation treatment has already been attained after 15 minutes of exposure time, but not yet after 2 minutes (comparing with the first series).

The curve fitting analysis of the C 1s detailed spectra, carried out following the routine employed in Section 4.2.3, is presented in Figure 4.19. Not surprisingly, the ratio of the deconvoluted component peaks follows the same pattern that was observed for the previous C 1s photoemission line FWHM evaluation. The ratio for the area of component peak II ( $A_{II}$ ) to the area of component peak I ( $A_I$ ) shown in Fig. 4.20 agrees well with the area ratios observed for the peak components of the C 1s line of the original sample in the  $T_w$  dependence experimental series. Hydrogenation causes an increment in the area ratio, indicating growth of the  $sp^3$ -hybridized peak. The ratio value change found for this second series (i.e.,  $\Delta A_{II}/A_I = 0.17$ , the difference between cycle stage 2 and stage 3) is significantly greater than the change produced by the 1700 K  $T_w$  hydrogenation treatment of the first experimental series ( $\Delta A_{II}/A_I = 0.11$ , see Figure 4.7). Note that not only the hydrogenation  $T_w$  and the hydrogenation exposure time might have an influence in the degree of hydrogen adsorption, but also the purity of the sample on the second experimental series was cleaner due to the applied heating stage. It is speculated that in this case the probability of hydrogen chemisorption is higher since more vacant adsorption sites are present.

Annealing of the hydrogenated sample decreases the  $A_{II}/A_I$  ratio. Nonetheless, as in the FWHM evaluation, the ratio does not relax back to the heat-treated sample value. A second course of hydrogenation treatment restores the  $A_{II}/A_I$  ratio to the one after the first

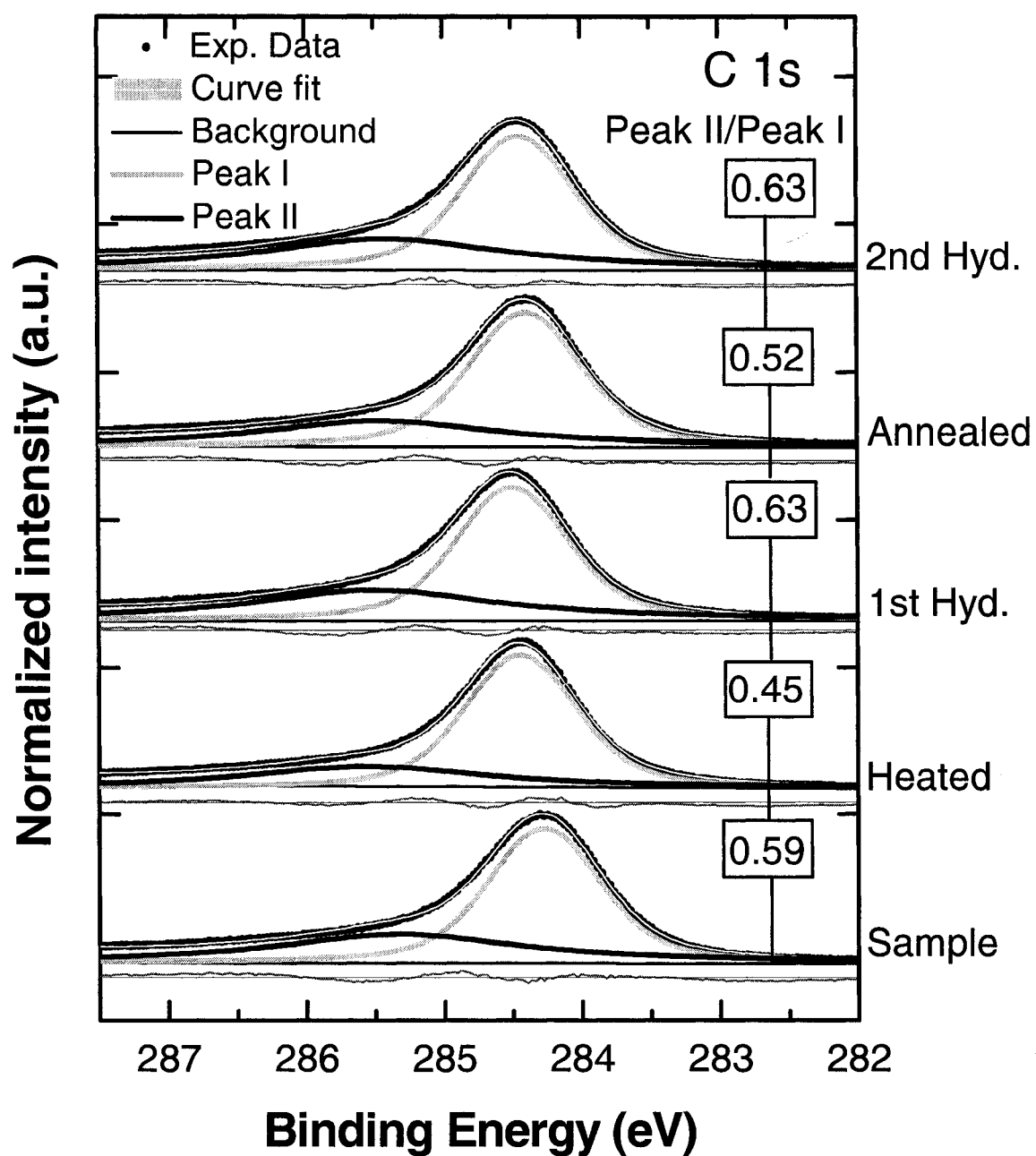


Figure 4.19 Deconvolution of the C 1s peak for the five phases of the experimental series (the fit residual shown below the background line has been magnified by a factor of 2).

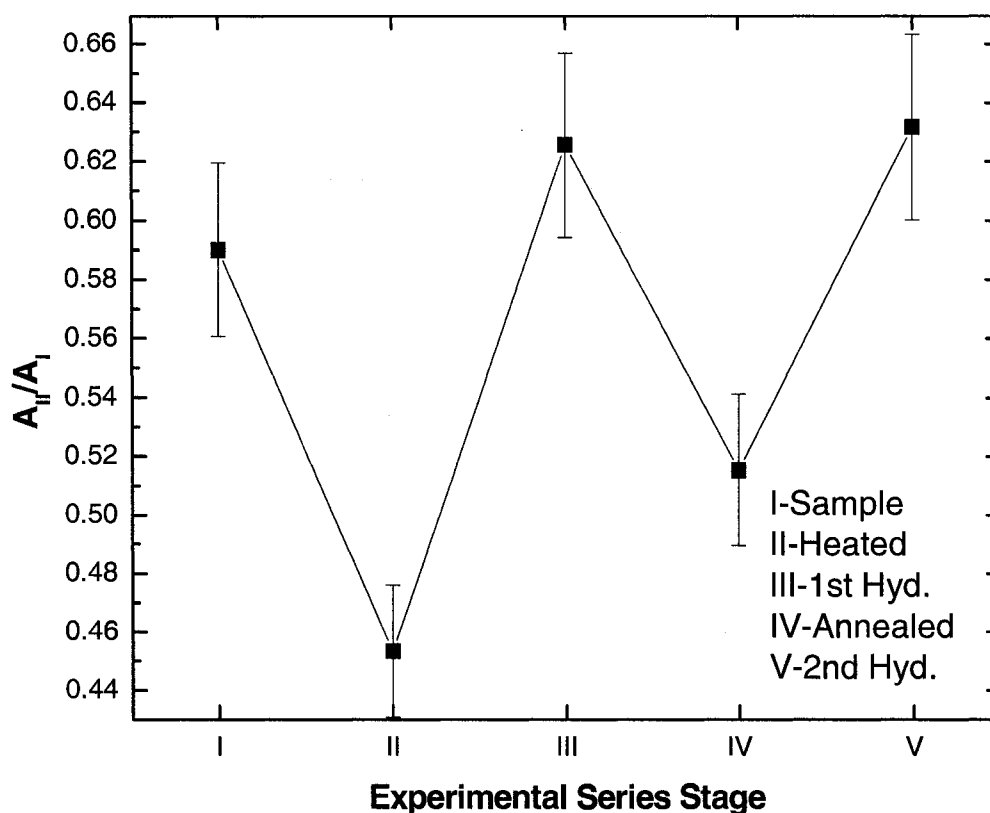


Figure 4.20 Peak II/Peak I (i.e.,  $sp^3/sp^2$  carbon hybridization) area ratio of the SWNT sample for the five stages of the experimental series.

hydrogenation treatment. Consequently, the change between stage IV and stage V is smaller than that between stage II and III. Possibly, some chemisorbed hydrogen remains after the annealing process or defects have been created in the SWNT. Since the second hydrogenation (with longer time period) does not show a significant enhancement in the fraction of hydrogen-bonding carbon, it appears that the maximum hydrogen coverage allowed for the atomic hydrogen produced at 1750 K  $T_w$  was reached during the first hydrogenation exposure.

#### 4.3.4 UPS Results

Figure 4.21 presents the VBM spectra of the sample throughout the stages of the experimental sequence. VB characterization of the sample was carried out via He II UPS as performed in Section 4.2.3. Note that, due to a He lamp failure, it was not possible to carry out the characterization of the rehydrogenated SWNT sample, i.e., the final stage in this series.

Baseline subtraction and curve fitting analysis of the  $\pi$ -peaks for the respective VBM spectra yields Figure 4.22. This analysis was carried out as explained in Section 4.2.4. Heat-treatment produces an increase of  $\pi$ -character in the SWNT sample. As a result of oxygen desorption due to sample annealing and resulting SWNT “healing” [25], the  $\pi$ -conjugation is enhanced in the heat-treated sample. Treating the sample for 15 minutes with an atomic/molecular hydrogen beam produced by a  $T_w = 1750$  K reduced the  $\pi$ -peak area to 77% compared to that of the heat-treated sample. The  $\pi$ -character in the hydrogenated sample is thus lower than the  $\pi$ -character for the SWNT sample before annealing. Since the 1700 K  $T_w$  hydrogenation treatment in the  $T_w$ -dependence study showed a  $\pi$ -peak reduction to 82% the of the original area, and because the as-introduced sample in the present study had a  $\pi$ -peak area of 83% the area of the one for the heat-treated sample, the hydrogenation treatment of the latter was expected to cause a  $\pi$ -peak reduction to an area lower than 70%, which is not observed. Annealing of the hydrogenated sample is seen to partially recover the  $\pi$ -character lost due to the hydrogenation treatment.

The shoulder at 10 eV BE again increases after hydrogenation of the sample, indicating  $\sigma$ -bond formation [23, 57, 62]. The observed increase is not as prominent as

produced by the higher  $T_w$  hydrogenations examined in Section 4.2.3; nonetheless, this feature appreciably diminishes after annealing the hydrogenated sample.

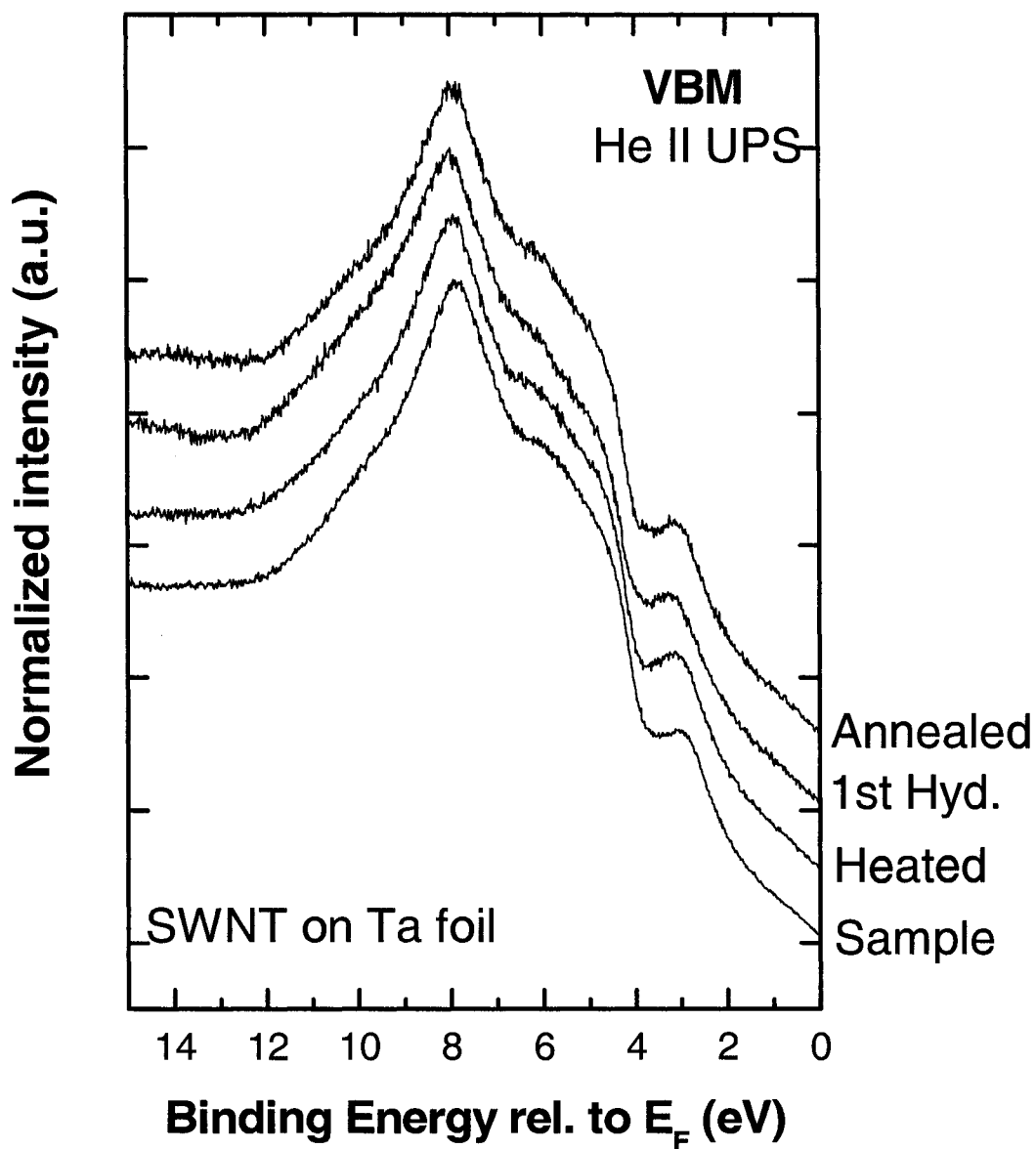


Figure 4.21 He II UPS spectra of SWNT sample on Ta foil in its original state and after various  $T_w$  hydrogenation treatments, normalized to the area below the presented data.



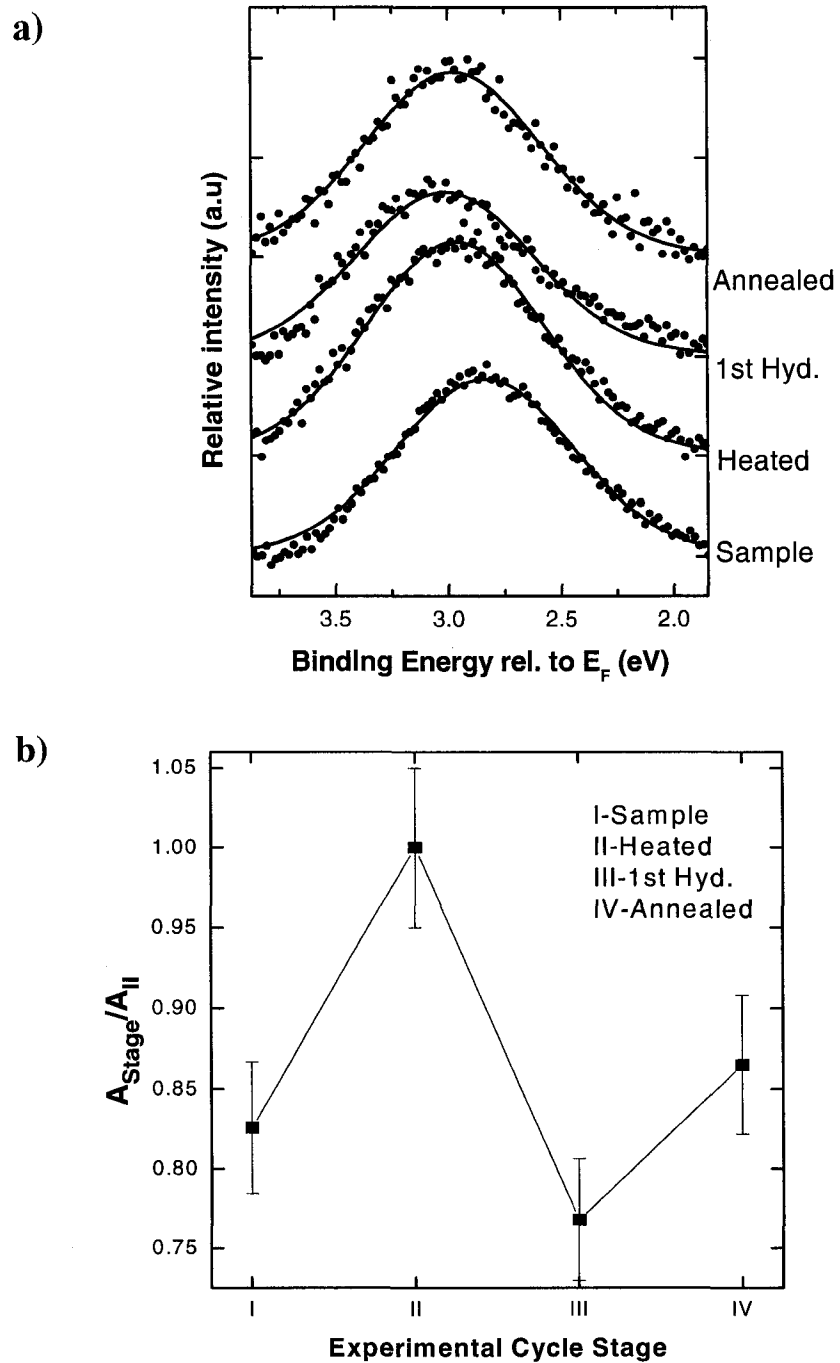


Figure 4.22 SWNT  $\pi$ -electron conjugation modulations for four stages of the experimental series: (a)  $\pi$ -state peaks extracted from the VB spectra shown in Figure 4.18; (b) comparison of  $\pi$ -state peak fit intensities relative to the heat-treated sample.

The  $\pi$ -peak for the as-introduced SWNT sample is found at 2.84 eV BE relative to  $E_F$ , which is in good agreement with the 2.88 eV BE  $\pi$ -peak of the original sample in the  $T_w$ -dependence study. After desorption of oxygen the  $\pi$ -peak shifts to a position 0.16 eV higher in BE, as observed in Figure 4.22a. This detected effect agrees well with theoretical work detailing a reduction in the energy band gap of SWNT as a result of oxygen chemisorption [63], an effect opposite to hydrogen chemisorption. Moreover, hydrogenation of the heat-treated sample yields a 0.05 eV  $\pi$ -peak positional shift to higher BE, reproducing the shift elicited by the 1700 K  $T_w$  hydrogenation treatment for the  $T_w$ -dependence study. Annealing the hydrogenated sample partially reversed the hydrogenation-induced shift.

The work function of the sample throughout the stages of the experimental series was again determined by He I UPS. Figure 4.23a presents the UPS cut-off spectra of the five experimental stages, from which the  $\Phi$  values were calculated. The  $\Phi$ -value for the as-introduced sample is in excellent agreement with the original sample of the  $T_w$ -dependence series,  $4.74 \pm 0.02$  eV and  $4.73 \pm 0.02$  eV, respectively. The  $\Phi$ -value for the heat-treated sample is reduced by  $0.17 \pm 0.04$  eV. This work function decrease agrees with the fact that oxygen desorbs from the sample during heat treatment. Because oxygen possesses greater electronegativity than carbon, oxygen functionalization of the SWNT will produce a negative surface charge on the sample [64]. This resulting negative charge will impose an additional energy barrier for electrons escaping from the sample surface. The removal of this energy barrier is observed in the  $\Phi$ -value drop effectuated by the heat-treatment. A further  $0.38 \pm 0.04$  eV decline in  $\Phi$  is attained by hydrogenation of the sample, as expected from the results of Section 4.2.3. This property

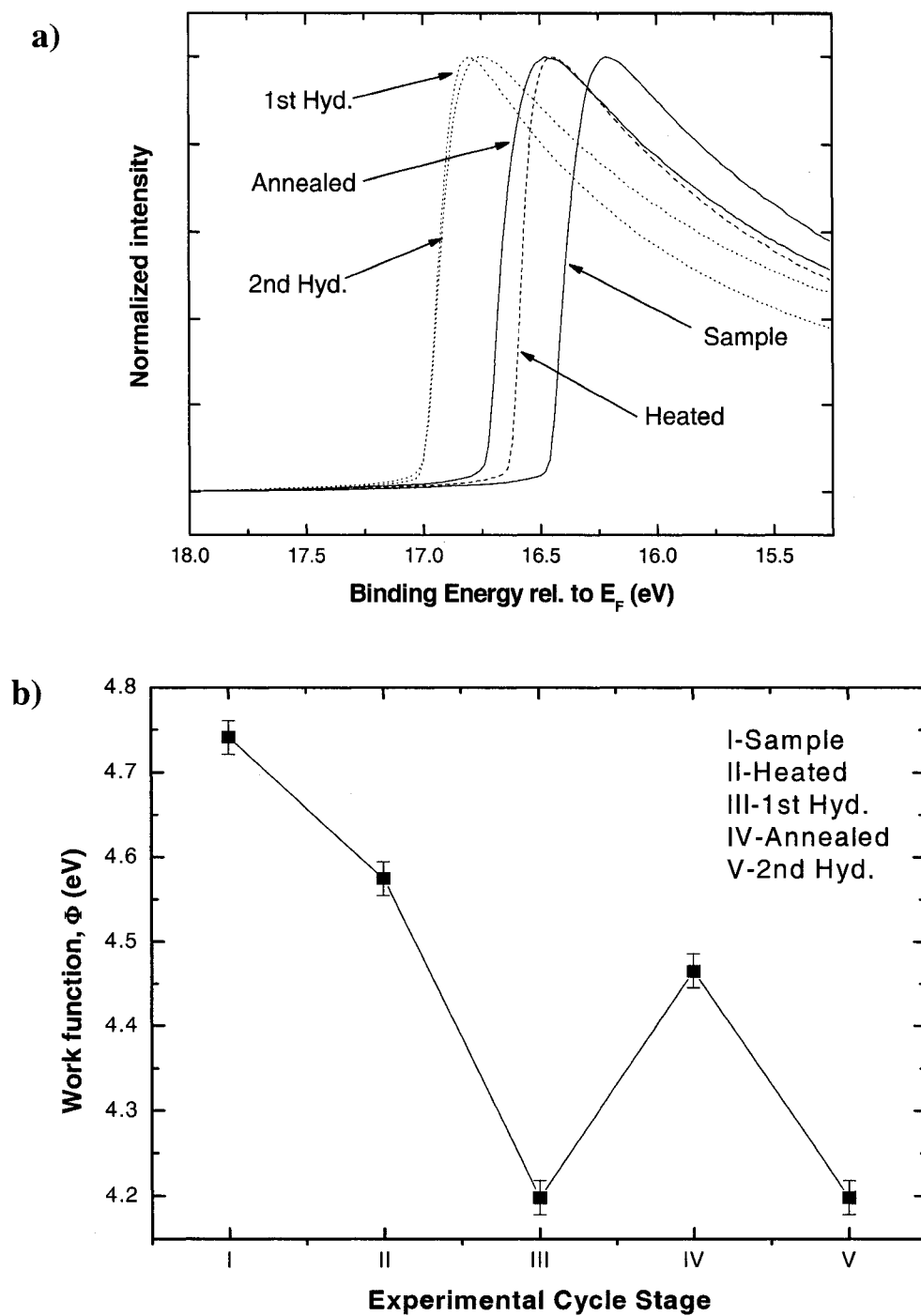


Figure 4.23 Work function changes resulting from hydrogen adsorption and desorption: (a) He I UPS secondary electron cut-off spectra for SWNT sample on Ta foil for the five stages of the study; (b) work function values throughout the course of the experimental series.

is significantly reversed by annealing, as this experimental series stage has shown to do with all previously analyzed hydrogenation-induced features. Furthermore, re-hydrogenation of the sample yields an identical  $\Phi$ -value to the one achieved by the first hydrogenation.

This experimental series has shown, through thermal desorption, the reversibility of the hydrogenation-induced chemical and electronic transformations of SWNT observed in experimental series (i). Additionally, the characteristics of SWNT exposed to  $T_w$  hydrogenation treatments at the onset of atomic generation from experimental series (i) were successfully reproduced with significantly reduced surface oxygen levels of the sample and no spurious effects due to fluorine contamination. This shows that the carbon speciation observed by hydrogenation treatments results predominantly from hydrogen chemisorption to  $sp^2$ -hybridized carbon. Furthermore, it was discerned that the saturation point of the surface fractional coverage for 1750 K  $T_w$  generated atomic hydrogen was achieved within the time of exposure of the first hydrogenation (15 minutes). Although the exposure time for the 1<sup>st</sup> hydrogenation of the second series was several factors greater than the 1700 K  $T_w$  hydrogenation treatment of experimental series (i), comparison of both sets of results does not show a great difference as a consequence.

Appendix II summarizes the results of this experimental series.

#### 4.4 C<sub>60</sub> hydrogenation Study

##### 4.4.1 Introduction

To complete our studies of the interaction between chemisorbed hydrogen and carbon nanomaterials, a hydrogenation study was performed on C<sub>60</sub> fullerenes. Due to the

increased surface curvature of this carbon nanomaterial with spherical geometry, the carbon  $sp^2$ -hybridized network exhibits an inherent degree of  $sp^3$ -character [65]. Since hydrogen chemisorption to  $sp^2$ -hybridized carbon must surmount a surface reconstruction energy requirement [26], a lower energetic requisite for  $C_{60}$  in principle would translate to easier hydrogenation of this storage matrix [23, 27].

#### 4.4.2 Experimental Procedure

The fullerene sample was prepared by depositing a few drops of a  $C_{60}$  dispersion in DMF on a Au-coated silicon wafer, as described in Section 4.3.2. The  $C_{60}$  powder used in the dispersion was obtained from TCI (Product # B1641) and had a  $C_{60}$  purity level >99.5% [66, 67]. The Au-coated silicon wafer was commercially obtained from Platypus Technologies. The sample was mounted on a SCIENTA molybdenum sample plate by use of carbon tape. Furthermore, a stainless steel clip fastened by a Mo screw was employed to further secure the sample and to provide adequate sample grounding. Due to malfunctioning of the heating stage element of the SCIENTA manipulator, sample heat treatment and thermal desorption of hydrogen could not be conducted. Since it was apparent that no heat treatments could be performed, the  $C_{60}$  series was conducted with a Au-coated silicon substrate to ease the sample preparation. Note that  $C_{60}$  sample heat-treatment would have been carried out at a considerably lower temperature than the one employed for the SWNT on Ta foil sample. This is due to the fact that the sublimation point for  $C_{60}$  is rather low, in the vicinity of 530 K [68, 69]. This could ultimately reduce the oxygen desorption efficacy of a sample heat-treatment stage. Regarding the hydrogen desorption effects of annealing hydrogenated  $C_{60}$ , literature reports only low degrees of

hydrogen desorption taking place at temperatures even close to the temperature onset of  $C_{60}$  evaporation [21], which might be important for future cycling experiments.

The experimental series consisted of three stages: (i) the original sample, (ii) molecular hydrogen exposure, and (iii) atomic/molecular hydrogen exposure. The hydrogenation treatments were performed in the preparation chamber of the SCIENTA system. The hydrogenation time of exposure for phase (ii) was 30 minutes. For phase (iii), the hydrogenation treatment lasted 3 minutes, and the  $T_w$  was 2000 K (note that, for this series, the gate valve responsible for the fluorine contamination at such temperatures had already been removed). Sample analysis was carried out in the same manner as in Section 4.3.2. Most of the PES scans were performed in the Andere ESCA with the same parameters as for the previous section. Detail spectra for the C 1s of the untreated sample and the atomic/hydrogen treated sample were also performed in the SCIENTA system using a monochromatized Al  $K_\alpha$  ( $h\nu=1486.58$  eV) x-ray source for better resolution. The SCIENTA electron analyzer entrance slit size was set to 0.8 mm. Additionally, a 50 eV pass energy and a 0.01 eV energy step were selected. From these parameters, equation 4 in Section 2.2.2 yields an analyzer energy resolution of 0.1 eV. Since the line width of the monochromated Al  $K_\alpha$  x-ray source ( $\Delta E_s$ ) is 0.27 eV, equation (7) in Section 4.2.1 yields a 0.29 eV overall instrumental energy resolution. To this value, the core lifetime must be incorporated to define the natural line width of the XPS core level lines, as mentioned in Section 2.1.3. From the C 1s detail XPS core level lines, it is found that the core lifetime adds 0.3 eV to the line width, in agreement with the C 1s core lifetime detected in the previous two experimental series.

Sample transfer between system components was performed again through the use of an adaptor, as described in Section 4.3.2.

#### 4.4.3 XPS Results

The XPS survey spectra show carbon (as expected), oxygen, chlorine, and sodium to be present at the sample surface, as demonstrated by Figure 4.24. Additionally, nitrogen lines were also observed, which are most likely due to residues from the DMF solvent. As in the case of the second experimental series, a Mo signal was detected, attributable to the screws securing the sample and to part of the impinging x-ray spot shining onto the Mo sample plate (note that this is only true for the Andere ESCA experiments, but not for the SCIENTA experiments since, in the latter case, the spot of the x-ray source is significantly smaller). A Au fingerprint is also seen in the survey spectra, which can be ascribed to the Au/Si substrate. The Au signal intensity increases significantly after the atomic/molecular hydrogenation treatment. Although it was not possible to measure the sample temperature during this specific experimental phase, from previous experiments it was observed that hydrogenation treatments at this  $T_w$  caused a small sample temperature change to a few degrees above room temperature. This makes thermal evaporation of  $C_{60}$  as a result of hydrogenation treatment very unlikely. On the other hand, the  $C_{60}$  layer appeared to not attach as strongly to the sample support as the SWNT layer did in the second experimental series. Retrieving the SCIENTA sample plate from the sample adaptor carrier in occasions required stern pulling. It is probable that some sample layer coverage may have been lost during the back and forth sample transferring process between the two system components.

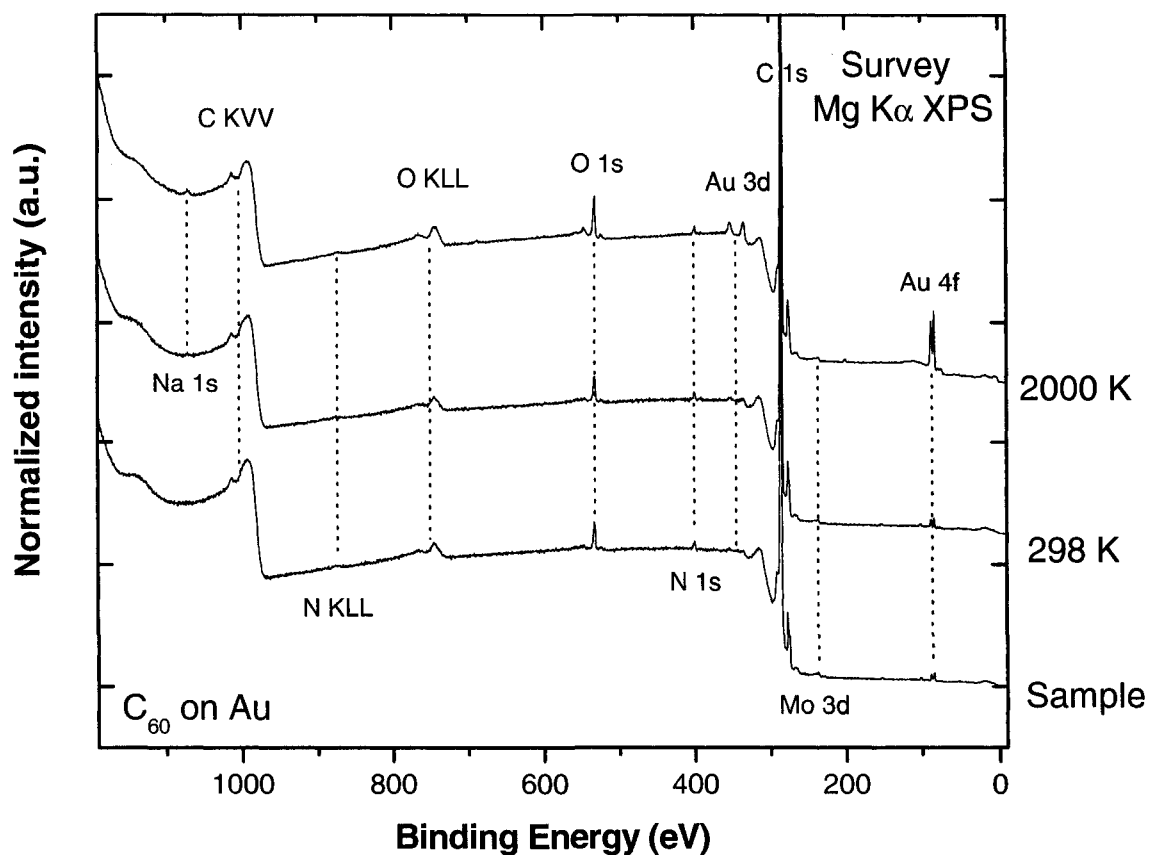


Figure 4.24 XPS survey spectra of a  $C_{60}$  sample on a Au-coated Si wafer in its original state and after the two hydrogenation treatments (the temperatures listed pertain to  $T_w$ ).

A comparison of the high-resolution detail C 1s spectra of the untreated sample and the sample after 2000 K  $T_w$  hydrogenation treatment is shown in Figure 4.25. A broadening of the C 1s photoemission line is observed after atomic hydrogen treatment. The elicited  $\Delta FWHM$  is close to 0.1 eV. Following the guidelines of Section 4.2.3, curve fitting analysis of the spectra reveals the emergence of a new C 1s component peak after sample exposure to atomic hydrogen. The distance between the two peak components is



0.4eV. The ratio value between the  $sp^3$ -hybridized component peak (peak II) and the  $sp^2$ -hybridized component peak (peak I) was 0.21.

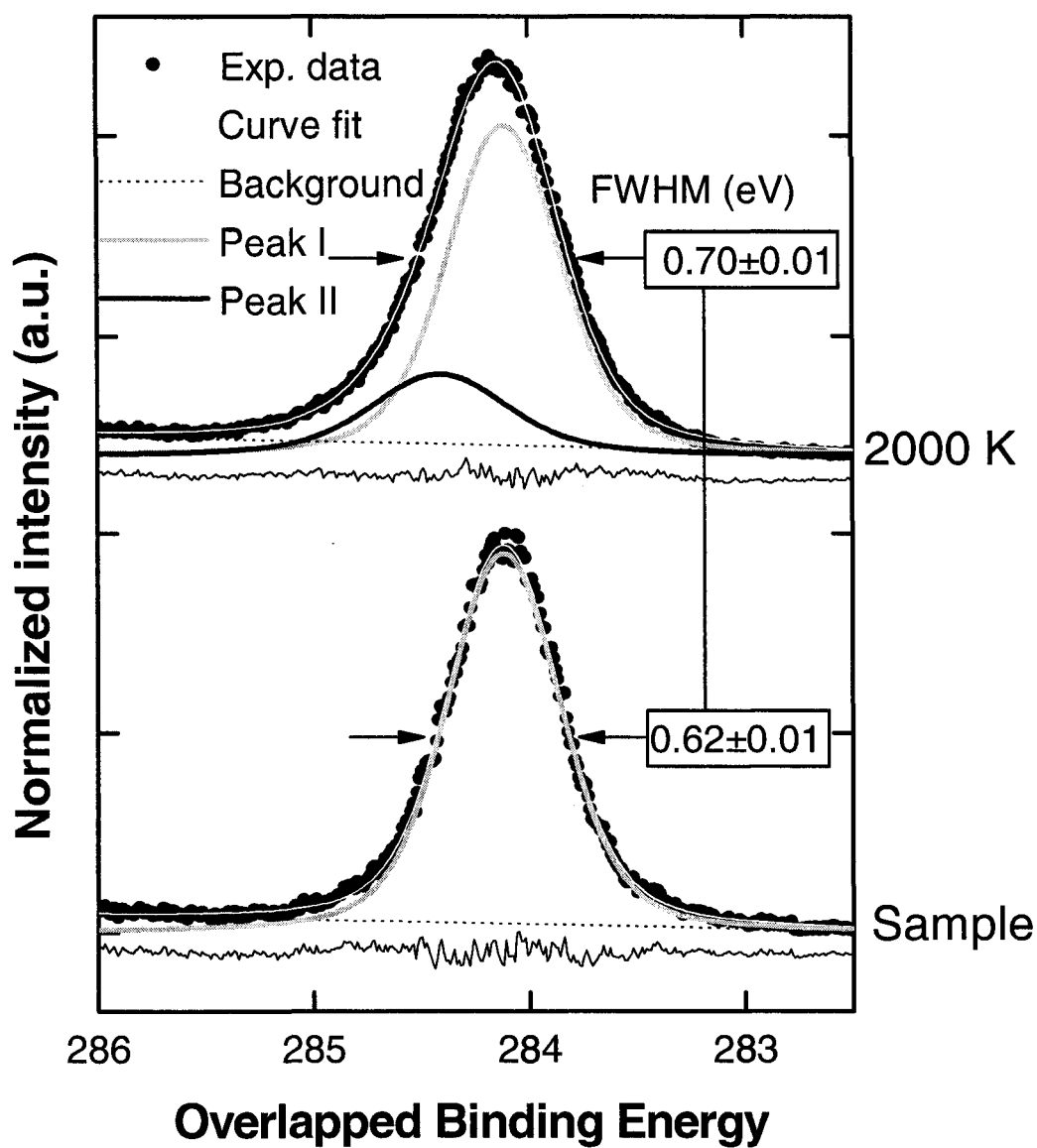


Figure 4.25 Deconvolution of the C 1s state line for the untreated C<sub>60</sub> sample and after 2000 K T<sub>w</sub> hydrogenation treatment.

#### 4.4.4 UPS Results

VB characterization of the sample was carried out with He II UPS as performed in Section 4.2.3. Figure 4.26 presents the VB spectra of the sample throughout the three stages of the experimental sequence. It can be noticed that molecular hydrogen exposure did not alter the VB structure of the C<sub>60</sub>. Contrary, atomic hydrogen treatment transformed several electronic state features.

The most conspicuous feature change resulting from atomic hydrogenation treatment is seen to be the intensity reduction of the peaks located at 2.3 eV and 3.6 eV. These peaks correspond to the highest occupied molecular orbital (HOMO) and the second highest occupied molecular orbital (HOMO-1), which are pure  $\pi$ -state orbitals [21, 70, 71].

Baseline subtraction and curve fitting of these orbitals show that the intensity of the HOMO and HOMO-1 of the atomic hydrogen-treated sample drops to 40% of that of the original C<sub>60</sub> sample. This was carried out by fitting sixth-order polynomial function backgrounds to extract the HOMO and HOMO-1 peaks, which were then fitted using two Voigt peaks and a linear background.

Additionally, it can be noticed in Figure 4.26 that an increase in intensity occurs at ~10 eV, indicating  $\sigma$ -bond formation [21]. The intensity at ~7 eV also increases, a region representing mixed  $\pi$  and  $\sigma$  character. Since the  $\pi$ -character of the sample decreases as its  $\sigma$ -character increases, the enhancement observed at the ~7 eV region is likely due to a strengthening of the  $\sigma$  component. Thus, as in the previous studies, the valence band spectra indicate a  $sp^2$  to  $sp^3$  hybridization transition induced by hydrogen chemisorption on C<sub>60</sub>.

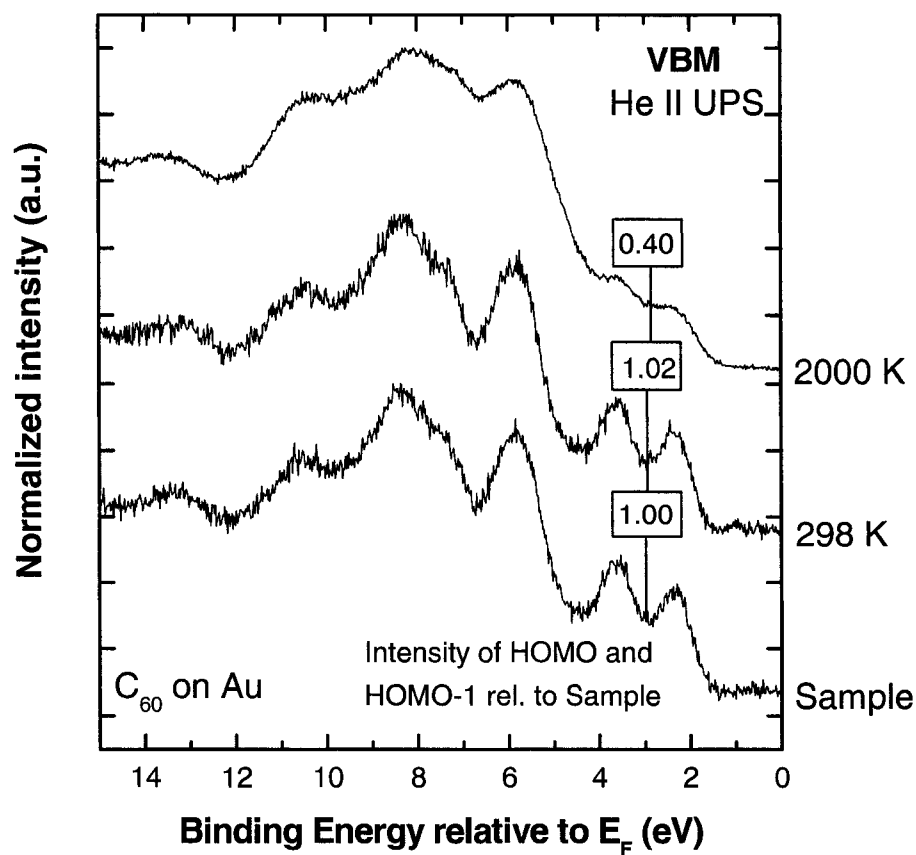


Figure 4.26 He II UPS VBM of  $C_{60}$  on Au in its original state and after molecular and atomic hydrogen treatments. Spectra are normalized to overall area.

The work function of the sample throughout the stages of the experimental series was determined by He I UPS. Figure 4.27 presents the secondary electron cut-off of the three experimental stages, from which the  $\Phi$  values were calculated. The  $\Phi$ -value for the untreated sample is  $4.31 \pm 0.02$  eV, which is close to the 4.44 eV reported for  $C_{60}$  multilayers on various metal surfaces [72]. Whereas the work function remains unchanged after molecular hydrogen exposure, the atomic hydrogenation treatment leads

to a 0.3 eV reduction. This reduction is attributed to hydrogen chemisorption to the carbon nanomaterial, as expected from the results of Section 4.2.4.

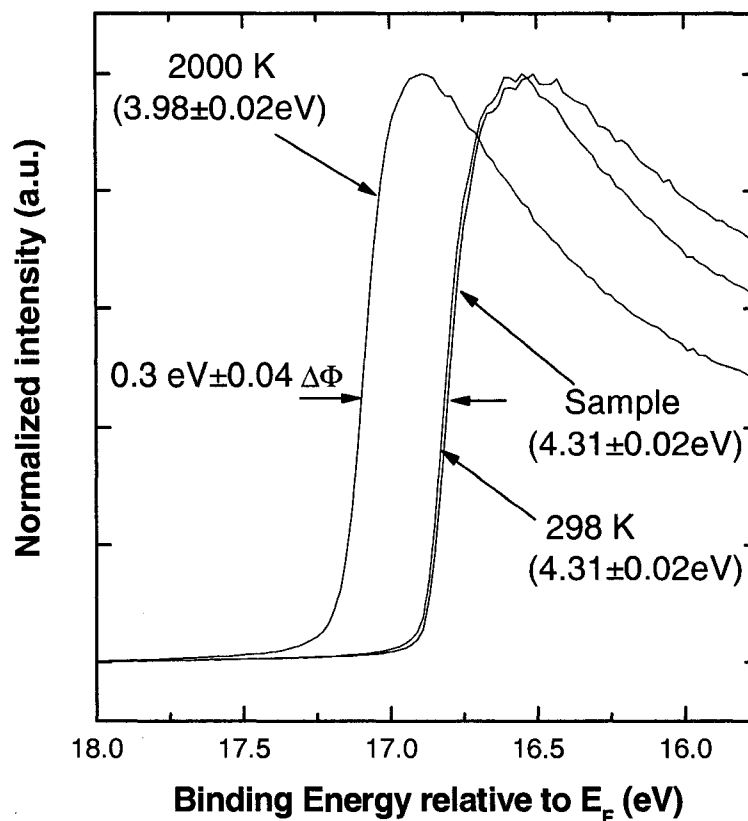


Figure 4.27 He I UPS secondary electron cut-off spectra for  $C_{60}$  on Au in its original state and after molecular and atomic hydrogen treatments; the respective work function values,  $\Phi$ , are shown in parenthesis.

This experimental series thus shows the transformation of chemical and electronic states of a  $C_{60}$  sample as a result of a (atomic) hydrogenation treatment. A similar pattern

of change is observed for all the characterized features as was the case in the first two experimental series.

## CHAPTER 5

### SUMMARY AND FUTURE WORK

#### 5.1 Summary

In this thesis, an atomic hydrogen source was constructed that allows the exposure of a large variety of materials to atomic hydrogen in ultra-high vacuum. Furthermore, the interactions between atomic hydrogen and carbon-based nanomaterials were studied. The samples submitted to molecular and/or atomic hydrogen treatments were probed using photoelectron spectroscopies to gain insight into the chemical and electronic properties of the hydrogen-chemisorbed samples. The findings give insight into the detailed bonding mechanisms, which helps to understand, determine, and optimize the hydrogen storage capacities of the analyzed materials.

In order to investigate the hydrogen dissociation capabilities of the constructed atomic hydrogen source, five series of mass spectroscopy runs were carried out at different hydrogen flow rates. The partial pressures for atomic hydrogen and molecular were monitored as a function of the tungsten capillary tube temperature of the atomic hydrogen sources. It was observed that for all analyzed flow rates, an appreciation in the atomic hydrogen partial pressure initiated at a capillary tube temperature of 1500 K. Furthermore, this partial pressure increased as the tube temperature was incremented, indicating greater hydrogen dissociation.

Three experimental series of sample hydrogenations were carried out. In the first series, changes of the C 1s core level and the valence band structure of a SWNT sample proceeded along with the capillary temperature during the hydrogenation treatment. An evaluation of these transformations indicates the formation of  $sp^3$ -hybridized carbon, simultaneous to a decrease of the number of carbon atoms in the  $sp^2$ -hybridized network. In the second series, the hydrogenation-induced alterations could be reverted by heating a hydrogenated SWNT sample in ultra-high vacuum. A second round of atomic hydrogen exposure of the same sample shows similar electronic modifications as observed after the first hydrogenation treatment. Such observations suggest the possibility of hydrogen storage reversibility in SWNT. In the third series, analogous changes in the C 1s core level and the valence band structure of  $C_{60}$  were elicited by hydrogen chemisorption.

## 5.2 Future Work

For structural information, the hydrogenated samples described above can be studied with Scanning Tunneling Microscopy. To probe their local density of electronic states and band gap, Scanning Tunneling Spectroscopy investigations can also be performed. Additionally, experimental hydrogenation series on transition-metal decorated carbon-based nanomaterials would be of great interest to pursue. Higher resolution studies as the ones presented in this thesis can also be procured with the present optimized state of the SCIENTA system and in the newly-installed photoemission system SALSA at the Advanced Light Source, Lawrence Berkeley National Laboratory. In that system, further analysis of the electronic properties of the hydrogenated samples can also take place by using X-ray Absorption Spectroscopy and X-ray Emission Spectroscopy. Finally, other

carbon-based nanomaterials, such as functionalized SWNT, buckyballs, nanohorns, etc., would be of great interest as well.



## APPENDIX I

### DETAILED XPS AND UPS DATA OF THE $T_w$ -DEPENDENT HYDROGENATION SERIES (SECTION 4.2)

$T_w$ (K)	C 1s Peak Position (eV)	C1s Shift (eV)	FWHM (eV)	$\Delta$ FWHM (eV)	sp3/sp2
0	284.51 $\pm$ 0.04	0.00	1.14 $\pm$ 0.02	0.00	0.60 $\pm$ 0.03
298	284.51 $\pm$ 0.04	0.00 $\pm$ 0.08	1.15 $\pm$ 0.02	0.01 $\pm$ 0.04	0.61 $\pm$ 0.03
1000	284.53 $\pm$ 0.04	0.02 $\pm$ 0.08	1.13 $\pm$ 0.02	-0.01 $\pm$ 0.04	0.63 $\pm$ 0.03
1500	284.53 $\pm$ 0.04	0.02 $\pm$ 0.08	1.16 $\pm$ 0.02	0.02 $\pm$ 0.04	0.63 $\pm$ 0.03
1700	284.60 $\pm$ 0.04	0.09 $\pm$ 0.08	1.17 $\pm$ 0.02	0.03 $\pm$ 0.04	0.71 $\pm$ 0.04
1800	284.63 $\pm$ 0.04	0.11 $\pm$ 0.08	1.21 $\pm$ 0.02	0.07 $\pm$ 0.04	0.78 $\pm$ 0.04
1850	284.64 $\pm$ 0.04	0.13 $\pm$ 0.08	1.22 $\pm$ 0.02	0.08 $\pm$ 0.04	0.78 $\pm$ 0.04
1900	284.67 $\pm$ 0.04	0.16 $\pm$ 0.08	1.23 $\pm$ 0.02	0.09 $\pm$ 0.04	0.84 $\pm$ 0.04
1950	284.68 $\pm$ 0.04	0.16 $\pm$ 0.08	1.22 $\pm$ 0.02	0.09 $\pm$ 0.04	0.82 $\pm$ 0.04
1975	284.65 $\pm$ 0.04	0.13 $\pm$ 0.08	1.24 $\pm$ 0.02	0.10 $\pm$ 0.04	0.87 $\pm$ 0.04
2000	284.66 $\pm$ 0.04	0.14 $\pm$ 0.08	1.23 $\pm$ 0.02	0.09 $\pm$ 0.04	0.88 $\pm$ 0.04
2050	284.70 $\pm$ 0.04	0.18 $\pm$ 0.08	1.30 $\pm$ 0.02	0.16 $\pm$ 0.04	0.97 $\pm$ 0.05

SWNT XPS C 1s peak transformation as a result of  $T_w$ -hydrogenation treatment, where 0

$T_w$  stands for untreated sample

$T_w$ (K)	$\pi$ -peak intensity rel. to sample	$\pi$ -state Position (eV)	$\pi$ -state shift (eV)	$\Phi$ (eV)	$\Delta\Phi$ (eV)
0	1	2.88 $\pm$ 0.02	0	4.67 $\pm$ 0.02	0
298	0.99 $\pm$ 0.05	2.90 $\pm$ 0.02	0.02 $\pm$ 0.04	4.66 $\pm$ 0.02	-0.01 $\pm$ 0.04
1000	0.95 $\pm$ 0.05	2.92 $\pm$ 0.02	0.04 $\pm$ 0.04	4.62 $\pm$ 0.02	-0.05 $\pm$ 0.04
1500	0.94 $\pm$ 0.05	2.90 $\pm$ 0.02	0.02 $\pm$ 0.04	4.62 $\pm$ 0.02	-0.05 $\pm$ 0.04
1700	0.83 $\pm$ 0.04	2.92 $\pm$ 0.02	0.04 $\pm$ 0.04	4.45 $\pm$ 0.02	-0.22 $\pm$ 0.04
1800	0.83 $\pm$ 0.04	2.95 $\pm$ 0.02	0.07 $\pm$ 0.04	4.36 $\pm$ 0.02	-0.31 $\pm$ 0.04
1850	0.81 $\pm$ 0.04	2.95 $\pm$ 0.02	0.07 $\pm$ 0.04	4.35 $\pm$ 0.02	-0.32 $\pm$ 0.04
1900	0.75 $\pm$ 0.04	3.03 $\pm$ 0.02	0.15 $\pm$ 0.04	4.29 $\pm$ 0.02	-0.38 $\pm$ 0.04
1950	0.88 $\pm$ 0.04	3.01 $\pm$ 0.02	0.13 $\pm$ 0.04	4.27 $\pm$ 0.02	-0.4 $\pm$ 0.04
1975	0.83 $\pm$ 0.04	3.03 $\pm$ 0.02	0.15 $\pm$ 0.04	4.25 $\pm$ 0.02	-0.42 $\pm$ 0.04
2000	0.65 $\pm$ 0.03	3.06 $\pm$ 0.02	0.18 $\pm$ 0.04	4.19 $\pm$ 0.02	-0.48 $\pm$ 0.04
2050	0.63 $\pm$ 0.03	3.01 $\pm$ 0.02	0.13 $\pm$ 0.04	4.14 $\pm$ 0.02	-0.53 $\pm$ 0.04

Valence Band conversions induced by  $T_w$ -hydrogenation treatment, where 0  $T_w$  stands for untreated sample.

## APPENDIX II

### DETAILED XPS AND UPS DATA OF THE HYDROGEN ADSORPTION/DESORPTION CYCLING SERIES (SECTION 4.3)

Stage	C 1s Peak Position (eV)	FWHM (eV)	$\Delta$ FWHM rel. heat-treated	
			sample (eV)	sp3/sp2
I	284.26 $\pm$ 0.04	1.11 $\pm$ 0.02	0.07 $\pm$ 0.04	0.59 $\pm$ 0.03
II	284.41 $\pm$ 0.04	1.04 $\pm$ 0.02	0	0.45 $\pm$ 0.02
III	284.47 $\pm$ 0.04	1.10 $\pm$ 0.02	0.06 $\pm$ 0.04	0.63 $\pm$ 0.03
IV	284.38 $\pm$ 0.04	1.07 $\pm$ 0.02	0.02 $\pm$ 0.04	0.52 $\pm$ 0.03
V	284.43 $\pm$ 0.04	1.10 $\pm$ 0.02	0.06 $\pm$ 0.04	0.63 $\pm$ 0.03

Analysis of the SWNT XPS C 1s peak as a result of hydrogen adsorption and desorption. Numerals I-V represent the experimental stages for untreated sample, heat-treated sample, hydrogenated sample, annealed sample, and re-hydrogenated sample, respectively.

Stage	$\pi$ -peak intensity rel.	$\pi$ -state Position	$\pi$ -state shift w.r.t	$\Delta\Phi$ (eV) w.r.t	
	to heat-treated sample	(eV)	heat-treated sample(eV)	$\Phi$ (eV)	heat-treated sample (eV)
I	0.83 $\pm$ 0.04	2.84 $\pm$ 0.02	-0.12966	4.74 $\pm$ 0.02	0.16 $\pm$ 0.04
II	1	2.97 $\pm$ 0.02	0	4.58 $\pm$ 0.02	0
III	0.77 $\pm$ 0.04	3.01 $\pm$ 0.02	0.04667	4.20 $\pm$ 0.02	-0.38 $\pm$ 0.04
IV	0.86 $\pm$ 0.04	2.98 $\pm$ 0.02	0.01175	4.47 $\pm$ 0.02	-0.11 $\pm$ 0.04
V	-	-	-	4.20 $\pm$ 0.02	-0.38 $\pm$ 0.02

Analysis of the valence band structure of the sample elicited by the adsorption/desorption cycles in stages I – III. Numerals I-V represent the experimental stages for untreated sample, heat-treated sample, hydrogenated sample, annealed sample, and re-hydrogenated sample, respectively.

## BIBLIOGRAPHY

- [1] E. Almqvist, History of Industrial Gases, Springer, New York 2003
- [2] Energy Information Administration, International Energy Outlook 2004, DOE/EIA-0484 2004
- [3] M. I. Hoffert, K. Caldeira, G. Benford, D. R. Criswell, C. Green, H. Herzog, A. K. Jain, H. S. Kheshgi, K. S. Lackner, J. S. Lewis, H. D. Lightfoot, W. Manheimer, J. C. Mankins, M. E. Mauel, L. J. Perkins, M. E. Schlesinger, T. Volk, and T. M. L. Wigley, Advanced Technology Paths to Global Climate Stability: Energy for a Greenhouse Planet, *Science* 298 (2002) 981
- [4] G. W. Crabtree, M. S. Dresselhaus, and M. V. Buchanan, The Hydrogen Economy, *Phys. Today* 57 (2004) 39
- [5] S. Hynek, W. Fuller, and J. Bentley, Hydrogen Storage by Carbon Sorption, *Int. J. Hydrogen Energy*, 22 (1997) 601
- [6] S. Iijima and T. Ichihashi, Single-shell carbon nanotubes of 1-nm diameter, *Nature* 363 (1993) 603
- [7] J. W. Ding, X. H. Yan, and J. X. Cao, Analytical relation of band gaps to both chirality and diameter of single-wall carbon nanotubes, *Phys. Rev. B* 66 (2002) 073401
- [8] URL: nano.gtri.gatech.edu (2008)
- [9] A. C. Dillon, K. M. Jones, T. A. Bekkedahl, C. H. Kiang, D. S. Bethune, and M. J. Heben, Storage of hydrogen in single-walled carbon nanotubes, *Nature* 386 (1997) 377
- [10] Y. Ye, C. C. Ahn, C. Witham, B. Fultz, J. Liu, A. g. Rinzler, D. Colbert, K. A. Smith, and R. E. Smalley, Hydrogen adsorption and cohesive energy of single-walled carbon nanotubes, *Appl. Phys. Lett.* 74 (1999) 2307
- [11] A. C. Dillon, T. Gennett, J. L. Alleman, K. M. Jones, P. A. Parilla, and M. J. Heben, in: Proceedings of the 2000 U.S. DOE Hydrogen Program Review, 2000, NREL/CP-507-28890
- [12] M. Hirscher, M. Becher, M. Haluska, F. von Zeppelin, X. Chen, U. Dettlaff-Weglikowska, and S. Roth, Are carbon nanostructures an efficient hydrogen storage medium?, *J. Alloys Compd.* 356-357 (2003) 433

- [13] T. W. Ebbesen, H. Hiura, M. E. Bisher, M. M. J. Treacy, J. L. Shreeve-Keyer, and R. C. Haushalter, Decoration of Carbon Nanotubes, *Adv. Mater.* 8 (1996) 155
- [14] M. Yudasaka, T. Ichihashi, D. Kasuya, H. Kataura, and S. Iijima, Structure changes of single-wall carbon nanotubes and single-wall carbon nanohorns caused by heat treatment, *Carbon* 41 (2003) 1273
- [15] A. Jung, R. Graupner, L. Ley, and A. Hirsch, Quantitative determination of oxidative defects on single walled carbon nanotubes, *Phys. Stat. Sol.* 243 (2006) 3217
- [16] T. Yildirim, O. Gülseren, and S. Ciraci, Exohydrogenated single-wall carbon nanotubes, *Phys. Rev. B* 64 (2001) 075404
- [17] S. Park, D. Srivastava, and K. Cho, Generalized Chemical Reactivity of Curved Surfaces: Carbon Nanotubes, *Nano Lett.* 3 (2003) 1273
- [18] A. V. Talyzin and S. Klyamkin, Hydrogen adsorption in  $C_{60}$  at pressures up to 2000 atm, *Chem. Phys. Lett.* 397 (2004) 77
- [19] H. Lüth, Surfaces and Interfaces of Solids, Springer-Verlag, Berlin (1993)
- [20] A. Zangwill, Physics at Surfaces, Cambridge University Press, New York (1996)
- [21] T. R. Ohno, C. Gu, and J. H. Weaver, Electronic properties of hydrogen-bonded fullerenes and potassium fullerenes, *Phys. Rev. B* 47 (1993) 13848
- [22] Y. Vasil'ev, D. Wallis, M. Nüchter, B. Ondruschka, A. Lobach, and T. Drewello, From major to minor and back—a decisive assessment of  $C_{60}H_{36}$  with respect to the Birch reduction of  $C_{60}$ , *Chem. Commun.* 14 (2000) 1232
- [23] P. Ruffieux, O. Gröning, M. Biemann, P. Mauron, L. Schlapbach, and P. Gröning, Hydrogen adsorption on  $sp^2$ -bonded carbon: Influence on the local curvature, *Phys. Rev. B* 66 (2002) 245416
- [24] A. Nikitin, H. Ogasawara, D. Mann, R. Denecke, Z. Zhang, H. Dai, K. Cho, and A. Nilsson, Hydrogenation of Single-Walled Carbon Nanotubes, *Phys. Rev. Lett.* 95 (2005) 225507
- [25] Y. Ma, Y. Xia, M. Zhao, M. Ying, X. Liu, and P. Liu, Collision of hydrogen atom with single-walled carbon nanotube: Adsorption, insertion, and healing, *J. Chem. Phys.*, 115 (2001) 8152
- [26] X. Sha, B. Jackson, First-principles study of the structural and energetic properties of H atoms on a graphite (0 0 0 1) surface, *Surf. Sci.* 496 (2002) 318

- [27] O. Gülseren, T. Yildirim, and S. Ciraci, Tunable Adsorption on Carbon Nanotubes, *Phys. Rev. B* 64 (2001) 116802
- [28] J. Li, T. Furuta, H. Goto, T. Ohashi, Y. Fujiwara, and S. Yip, Theoretical evaluation of hydrogen storage capacity in pure carbon nanostructures, *J. Chem. Phys.* 119 (2003) 2376
- [29] A. D. Lueking and R. T. Yang, Hydrogen spillover to enhance hydrogen storage—study of the effect of carbon physicochemical properties, *Appl. Catal. A* 265 (2004) 259
- [30] T. Yildirim and S. Ciraci, Titanium-Decorated Nanotubes as a Potential High-Capacity Hydrogen Storage Medium, *Phys. Rev. Lett.* 94 (2005) 175501
- [31] Q. Sun, P. Jena, Q. Wang, and M. Marquez, First-Principles Study of Hydrogen Storage on  $\text{Li}_{12}\text{C}_{60}$ , *J. Am. Chem. Soc.* 128 (2006) 9741
- [32] H. Hertz, Über einen Einfluss des ultravioletten Lichtes auf die elektrische Entladung, *Ann. Physik* 31 (1887) 983
- [33] S. Hüfner, Photoelectron Spectroscopy: Principles and Applications, Springer, Berlin (2003)
- [34] D. Briggs and M. P. Seah, Practical Surface Analysis, John Wiley & Sons Ltd., Chichester, England 1990
- [35] D. J. O'Connor, B. A. Sexton, and R. St. C. Smart, Surface Analysis Methods in Materials Science, Springer-Verlag, Berlin (1992)
- [36] J. F. Moulder, W. F. Stickle, P. E. Sobol, and K. D. Bomben, Handbook of X-ray Photoelectron Spectroscopy, Perkin-Elmer Corporation, USA (1992)
- [37] U. Bischler and E. Bertel, Simple source of atomic hydrogen for ultrahigh vacuum applications, *J. Vac. Sci. Technol. A* 11 (1993) 458
- [38] I. Langmuir, A chemically active modification of hydrogen, *J. Amer. Chem. Soc.* 34 (1912) 1320
- [39] W. Zheng and A. Gallagher, Hydrogen dissociation on high-temperature tungsten, *Surf. Sci.* 600 (2006) 2207
- [40] K. Christmann, Interaction of Hydrogen with Solid Surfaces, *Surf. Sci. Rep.* 9 (1988) 1
- [41] D. A. Butler, B. E. Hayden, and J. D. Jones, Precursor dynamics in dissociative hydrogen adsorption on W (100), *Chem. Phys. Lett.* 217 (1994) 423

- [42] G. Ehrlich, Molecular Dissociation and Reconstitution on Solids, *J. Chem. Phys.* 31 (1959) 1111
- [43] T. W. Hickmott, Interaction of Hydrogen with Tungsten, *J. Chem. Phys.* 32 (1960) 810
- [44] D. Brennan and P. C. Fletcher, The atomization of hydrogen on tungsten, *Proc. Roy. Soc. A*, 250 (1959) 389
- [45] L. Stobinski and R. Dus, Rate of H<sub>2</sub> atomization over the surface of a hot tungsten filament, *Vacuum* 46 (1995) 433
- [46] Marathon MM Series High-Performance Infrared Thermometer Operating Instructions, *Rev. C1* (2007)
- [47] C. Eibl, G. Lackner, and A. Winkler, Quantitative characterization of a highly effective atomic hydrogen doser, *J. Vac. Sci. Technol. A*. 16 (1998) 2979
- [48] K. G. Tschersich and V. von Bonin, Formation of an atomic hydrogen beam by a hot capillary, *J. Appl. Phys.* 84 (1998) 4065
- [49] B. J. Wood, and H. Wise, Diffusion and Heterogeneous Reaction. II. Catalytic Activity of Solids for Hydrogen-Atom Recombination, *Physics* 29 (1958) 1416
- [50] Unidym, Inc., Product Description: HiPco Single-Wall Carbon Nanotubes (2008)
- [51] L. Brelsford, private communication (2008)
- [52] T. W. Ebbesen, H. Hiura, M. E. Bisher, M. M. J. Treacy, J. L. Shreeve-Keyer, and R. C. Haushalter, Decoration of Carbon Nanotubes, *Adv. Mater.* 8 (1996) 155
- [53] M. T. Martínez, M. A. Callejas, A. M. Benito, M. Cochet, T. Seeger, A. Ansón, J. Schreiber, C. Gordon, C. Marhie, O. Chauvet, J. L. G. Fierro, and W. K. Maser, Sensitivity of single wall carbon nanotubes to oxidative processing: structural modification, intercalation, and functionalisation, *Carbon* 41 (2003) 2247
- [54] R. Haerle, E. Riedo, A. Pasquarello, and A. Baldereschi, sp<sup>2</sup>/sp<sup>3</sup> hybridization ratio in amorphous carbon from C 1s core-level shifts: X-ray photoelectron spectroscopy and first-principles calculation, *Phys. Rev. B* 65 (2001) 045101
- [55] A. Jung, R. Graupner, L. Ley, and A. Hirsch, Quantitative determination of oxidative defects on single walled carbon nanotubes, *Phys. Stat. Sol.* 243 (2006) 3217
- [56] B. N. Khare, P. Wilhite, M. Meyyappan, The fluorination of single wall carbon nanotubes using microwave plasma, *Nanotechnology* 15 (2004) 1650



- [57] J. Schäfer, J. Ristein, R. Graupner, L. Ley, Photoemission study of amorphous carbon modifications and comparison with calculated densities of states, *Phys. Rev. B* (1996) 7762
- [58] K. S. Kim, D. J. Bae, J. R. Kim, K. A. Park, S. C. Lim, J. Kim, W. B. Choi, C. Y. Park, and Y. H. Lee, Modification of Electronic Structures of a Carbon Nanotube by Hydrogen Functionalization, *Adv. Mater.* 24 (2002) 1818
- [59] K. A. Park, K. Seo, and Y. H. Lee, Adsorption of Atomic Hydrogen on Single-Walled Carbon Nanotubes, *J. Phys. Chem. B* 109 (2005) 8967
- [60] G. Buchs, A. V. Krashennnikov, P. Ruffieux, P. Gröning, A. S. Foster, R. M. Nieminen, and O. Gröning, Creation of paired electron states in the gap of semiconducting carbon nanotubes by correlated hydrogen adsorption, *New J. Phys.* 9 (2007) 275
- [61] P. Ruffieux, O. Gröning, M. Biemann, L. Schlapbach, and P. Gröning, Hydrogen Atoms Cause Long-Range Electronic Effects on Graphite, *Phys. Rev. Lett.* 84 (2000) 4910
- [62] J. Robertson, E.P. O'Reilly, Electronic and atomic structure of amorphous carbon, *Phys. Rev. B* 35 (1987) 2946
- [63] V. Barone, J. Heyd, and G. E. Scuseria, Effect of oxygen chemisorption on the energy band gap of a chiral semiconducting single-walled carbon nanotube, *Chem. Phys. Lett.* 389 (2004) 289
- [64] S. Dag, O. Gülseren, T. Yildirim, and S. Ciraci, Oxygenation of carbon nanotubes: Atomic structure, energetics, and electronic structure, *Phys. Rev. B* 67 (2003) 165424
- [65] J. Guo, Synchrotron radiation, soft-X-ray spectroscopy and nanomaterials, *Int. J. of Nanotechnology* 1 (2004) 193
- [66] TCI, C<sub>60</sub> & C<sub>70</sub> The Third Form of Carbon, TCI Product Literature (2007)
- [67] R. Brelsford, private communication (2008)
- [68] R. Fasel, R. G. Agostino, P. Aebi, and L. Schlapbach, Unusual molecular orientation and frozen librational motion of C<sub>60</sub> on Cu(110), *Phys. Rev. B* 60 (1999) 4517
- [69] G. Bertoni, C. Cepek, and M. Sancrotti, Temperature-dependent interaction of C<sub>60</sub> with Ge(1 1 1)-c(2 x 8), *Appl. Surf. Sci.* 212 (2003) 52
- [70] J. H. Weaver, J. L. Martins, T. Komeda, Y. Chen, T. R. Ohno, G. H. Kroll, and N. Troullier, Electronic Structure of Solid C<sub>60</sub>: Experiment and Theory, *Phys. Rev. Lett.* 66 (1991) 1741

[71] G. Cherkashinin, S. Krischok, M. Himmerlich, O. Ambacher, and J. A. Schaefer, Electronic properties of C<sub>60</sub>/InP(001) heterostructures, *J. Phys.: Condens. Matter* 18 (2006) 9841

[72] W. Brütting, Physics of Organic Semiconductors, Wiley-VCH Verlag GmbH, New York 2005

## VITA

Graduate College  
University of Nevada, Las Vegas

Roberto Félix

Home Address:

3401 Mary Ann Ave.  
Las Vegas, Nevada 89101

Degree:

Bachelor of Science, Chemistry, 2005  
University of Nevada, Las Vegas

Thesis Title: Study of the Interaction between Hydrogen and Carbon-based  
Nanomaterials

Thesis Examination Committee:

Chairperson, Dr. Clemens Heske, Dr. rer. nat.

Committee Member, Dr. Chulsung Bae, Ph. D.

Committee Member, Dr. Balakrishnan Naduvalath, Ph. D.

Graduate College Representative, Dr. Pamela Burnley, Ph. D.